B.M.H. Weninger

The Battolyzer

Combined short- and long-term energy storage

TU Delft

The Battolyzer
Combined short- and long-term energy storage

By
B.M.H. Weninger

in partial fulfilment of the requirements for the degree of

Master of Science
in Sustainable Energy Technology

at the Delft University of Technology,
to be defended publicly on Wednesday March 16, 2016 at 9:00 AM.

Student number:	4280113
Faculty:	Applied Sciences
Department:	Chemical Engineering
Section:	Materials for Energy Conversion and Storage

Supervisor:	Prof.dr. F.M. Mulder,	MECS, TU Delft
Thesis committee:	Prof.dr. F.M. Mulder,	MECS, TU Delft
	Prof.dr. B. Dam,	MECS, TU Delft
	Dr. W.G. Haije,	P&E, 3ME, TU Delft

TU Delft

Acknowledgements

First of all, I would like to thank all those people who made this thesis possible.

I want to thank my advisor Fokko Mulder at Delft University. He offered his advice and encouragement throughout the course of this thesis. We have spent quite some hours deliberating; about the new idea, about ways to built the battolyzer, about the materials to use, about the outcome of the test results and about the ways to overcome the setbacks. And of course for the exciting time of - hopefully - publishing an article in Nature.

Furthermore I would like to express my gratitude to Herman Schreuders, Joost Middelkoop, and Frans Ooms for their technical assistance. Herman and Joost helped me in designing the battolyzer and provided any assistance needed. Frans supported me with all "Maccor" related issue.

I also would like to express my gratitude to David Vermaas, who taught me to operate a potentiostat and to work with reference electrodes, and to Ibadillah Digdaya who helped me with the theory on electrical impedance measurements.

I am thankful to Michael Mikusik and especially to Jeroen Nijman for their support and grammatical editing of my thesis.

Finally, I take this opportunity to express my gratitude to my wife Karin Nijman-Weninger for the encouragement whenever I needed it, and I thank my daughter Florine and my newborn son Raphael for the endless joy and energy they give me.

Bernhard Weninger

Alphen aan den Rijn, March 2016

Abstract

In the study described in this thesis, it is demonstrated that combined short-term and long-term energy storage in one device, the battolyzer, is possible. The battolyzer is a device that works as a rechargeable battery, and that is capable of performing highly efficient electrolysis with any excess electricity. The battolyzer was based on the Nickel-Iron-Battery, which was developed by Thomas Edison and Waldemar Jungner, and on alkaline electrolysis. Both are well-established technologies that were developed more than a century ago.

The main research question in this thesis is: *"Is an energy storage system based on Nickel and Iron suitable to operate as an integrated battery and electrolyzer, and what would be the overall energy efficiency of such a device?"*.

Firstly, a test-series that was designed to simulate various real-life situations, including partial and full charging and discharging, rapid switching, continuous overcharging, and the around-the-clock cycling. Neither the battery, nor the electrolysis have noticeably deteriorated after the many cycles. The remarkable finding is that the reversible discharge capacity of the battery is not adversely affected by such harsh test conditions.

Secondly, the gas quality was analyzed, qualitatively and quantitatively. The outcome of these tests was that overcharging leads to gas production with a Coulombic (or Faradaic) conversion efficiency of equal to 100%, within the experimental accuracy.

In a final step, optimal operating conditions for the battolyzer have been identified. Tests show that the overall energy efficiency of the battolyzer could surpass 90%. However, the most remarkable finding of the whole project is the stability of the energetic efficiency at 80-90% over many different types of cycles, including all cycles to simulate real-life situations.

We anticipate these results to be a starting point for a robust grid-scale energy storage solution in a low-cost, abundant-element based, intrinsically flexible device that has close to full-time operability: as electrical power storage, switchable electricity supply, and as a hydrogen producer.

Parts of this thesis have been submitted to nature on 10th November 2015, with the title "Efficient electricity storage with an integrated alkaline Ni-Fe battery and electrolyser", manuscript nr. 2015-11-15677. On 9th February 2016 the first revision of the manuscript was submitted. On 9th March 2016, the current stage of the revised manuscript is "Manuscript under consideration".

Contents

1 Introduction

1.1 Motivation

Obtaining energy on demand is a key feature of our modern standard of living. Renewable energy systems have the potential to replace fossil fuels, but inherently confront us with the major challenge of storage. Fossil fuels, such as gas, oil, or coal, are easy to store, and make for very easy energy production. Renewable energy, on the other hand, is only available when the wind is blowing or the sun is shining. Our energy consumption is also characterized by diurnal and seasonal fluctuations. Solar energy, for example, is available on sunny days in summer, while private consumption is at a maximum on cold days in winter.

Technical solutions are necessary to overcome these discrepancies. In a renewable energy future, similar quantities of electricity storage, in batteries and in the production of hydrogen fuels, may be required on an annual basis, to allow adequate short-term (daily), and long-term (seasonal) energy storage[1]. The transition of the energy sector to renewable energy is only possible with efficient short- and long-term energy storage.

Batteries are appropriate for short-term energy storage. An important characteristic is that the stored electricity comes back as electricity and that the efficiency is typically high. However, they are not deployable for seasonal storage due to the high investment costs.

Producing hydrogen is considered to be the best opportunity for long-term energy storage, because it can be used to generate electricity or heat when required. Hydrogen can be stored directly or it can be synthesized to produce synthetic fuels. Furthermore, hydrogen production enables the ‘greening’ of chemical processes since hydrogen acts as feedstock for subsequent thermal processes, like the Sabatier (CH_4 from H_2 and CO_2), Fischer- Tropsch (alkanes from CO/CO_2 and H_2), and the Haber-Bosch process (NH_3 from N_2 and H_2). Electrolyzers are used to produce hydrogen on a large scale. In a renewable future with varying supply of electricity they will typically only operate when there is excess energy, and all short-term options for energy storage have been exhausted. Since electrolyzers are designed for continuous operation, downtime is financially undesirable.

In this work a prototype of a device that combines short and long-term energy storage is designed and tested. This device is a combined battery and electrolyzer. Our starting point is the Nickel-Iron battery, also known as the Edison cell, which is virtually indestructible. This type of battery was once very common, but it vanished with the evolution of the lead-acid battery, as the efficiency of nickel-iron batteries is poor. The reason for the low efficiency is hydrogen evolution. Hydrogen evolution was considered a loss because the hydrogen could not be used. Research into nickel-iron batteries has been flourishing in an effort to minimize the hydrogen evolution. In this study, the opposite approach is taken, by investigating the combined performance as battery and electrolyzer by purposely stimulating the hydrogen production.

A device based on the elements nickel and iron was assembled and designed to operate as a combined battery and electrolyzer. Traditionally, two distinct devices have been necessary for these operations. As the combined device can operate continuously, and - as will be shown - efficiently, it will be economically preferable compared to separate devices. The electricity storage capabilities can stabilize the short-term variation in renewable power, while the hydrogen production enables long-term energy storage and 'greening' of chemical processes. The battolyzer

combines efficient short-term and long-term energy storage, which gives it the potential to contribute to the transition of the energy- and hydrogen-based chemical sector towards renewable energy.

1.2 Research question

The materials applied in a Nickel-Iron cell are environmentally friendly, and they are available for large-scale applications. Current research, focusing on the battery application only, investigates the following options:

- Increase in the cell performance (capacity and speed),
- Suppression of the hydrogen evolution, and
- Development of a sealed unit with recombination of H_2 and O_2 when formed.

In this work I will investigate a different, or rather opposite, approach: to develop and use a combined device as a battery and an electrolyzer. Instead of suppressing the hydrogen evolution reaction, this characteristic will be exploited in order to produce hydrogen. The main idea is to use the battery's capacity for daily storage to handle electricity supply and fluctuation, and to produce hydrogen when excess energy is available beyond the level required to store on a short-timescale.

This topic will be approached by answering the following research questions:

"Is an energy storage system based on Nickel and Iron suitable to operate as an integrated battery and electrolyzer, and what would be the overall energy efficiency of such a device?"

The main research-question will be answered by means of the following sub-questions:

1. What are the main components of Nickel-Iron batteries and alkaline electrolysis?
2. Can these components be used for a combined device or is it necessary to invent/assemble components?
    a. What is the best choice for the positive electrode?
    b. What is the best choice for the negative electrode?
    c. What is the best choice for the diaphragm?
    d. Which electrolyte should be applied?
3. Does the concept of the battolyzer work?
    a. Do the electrodes withstand severe overcharging?
    b. Does overcharging lead to gas production?
    c. Do side reactions occur?
    d. Is the system efficient, and what factors influence the efficiency?
4. How can the system be classified compared to state-of-the art alkaline electrolyzers and batteries?

1.3 Birth of the battolyzer

From here on, the name battolyzer will be used for the combined battery - electrolyzer cell. Merging *BATT*-ery and electr-*OLYZER* simply forms *BATTOLYZER.*

I define the battolyzer as follows:

"The battolyzer is a device that works as a rechargeable battery, and that is capable of performing highly efficient electrolysis with any excess electricity."

In other words, the battolyzer accepts unlimited electrical energy as input and provides electrical and chemical energy as output.

1.4 Methodology

To answer the first two sub-questions, available resources as academic papers, journals, reports, textbooks, and web pages will be consulted.

Chapter 2 covers the theoretical background of this work.

Chapter 3 describes the design process of the battolyzer. First I investigated the components of an existing Ni-Fe cell. Furthermore, materials are defined which are suitable for a test cell. Together this together leads to the final layout for the battolyzer.

Chapter 4 describes tests that are performed with commercial cells and with the battolyzer to evaluate the relative efficiency of those systems. Besides variations in charge/discharge rates and temperature, variations in the electrolyte composition are tested. Furthermore, a test-series is contemplated and recorded to be able to provide results about the cycle life of the cells.

Chapter 5 provides an overview of the results.

In chapter 6, the results are compared with state-of-the-art batteries and alkaline electrolyzers. Furthermore, possible discussions are set out, and suggestions are made for further research.

2 Background information

This chapter describes the theoretical and technical framework of this thesis. Electrochemistry and the operating principle and related thermodynamics of an electrochemical cell are introduced. This section is not restricted to batteries only, but also explains the basics of electrolysis. The next two sections elaborate on Ni-Fe batteries and alkaline electrolysis, as these two technologies are the basis for this thesis. Furthermore, the stability of the materials is discussed by means of Pourbaix diagrams and an extra section is spent on the alkaline electrolyte. The efficiency of a combined device is defined as well. The final part of this chapter covers the theory behind the experimental methods that were applied.

2.1 Introduction to electrochemistry

2.1.1 Cell operation

A battery is a device that transforms chemical energy into electricity while discharging the cell. Batteries can be categorized as primary batteries or secondary batteries. The chemical processes in a primary battery are irreversible, while those in a secondary battery are reversible. Consequently, a secondary battery can be charged by transforming electrical energy back into chemical energy. So primary batteries can be used once, where secondary batteries can be recharged and therefore cycled, alternating charging and discharging. Ni-Fe batteries are secondary batteries.

Figure 2.1 shows the working principle for the Ni-Fe battery with the associated chemical reactions. Next to charging and discharging, electrolysis and self-discharge are displayed.

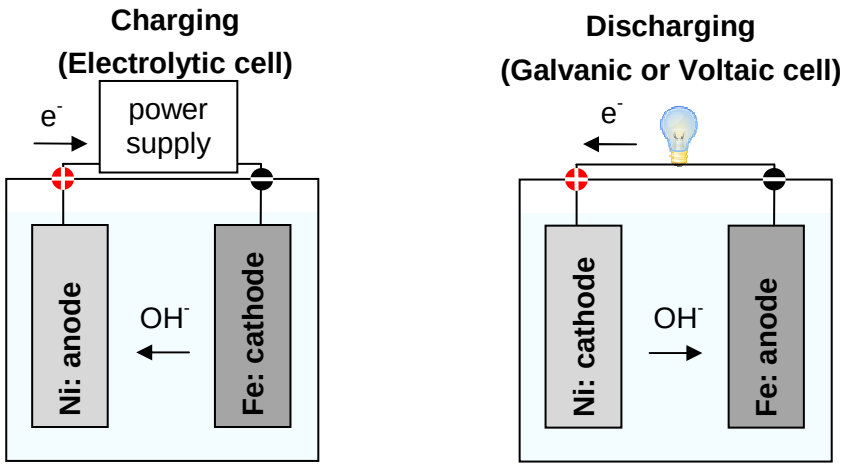

Cathode: $Fe(OH)_2 + 2e^- \rightarrow Fe + 2OH^-$ $NiOOH + H_2O + e^- \rightarrow Ni(OH)_2 + OH^-$

Anode: $Ni(OH)_2 + OH^- \rightarrow NiOOH + H_2O + e^-$ $Fe + 2OH^- \rightarrow Fe(OH)_2 + 2e^-$

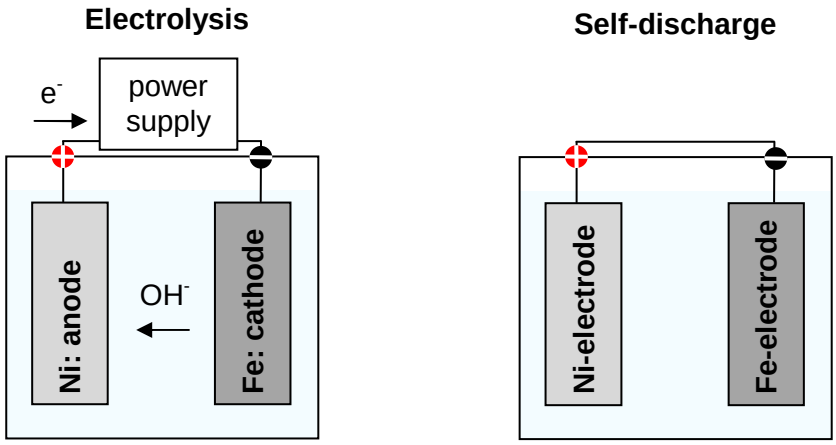

Iron/Cathode: $2H_2O + 2e^- \rightarrow H_2 + 2OH^-$ $Fe + 2H_2O \rightarrow Fe(OH)_2 + H_2$

Nickel/Anode: $4OH^- \rightarrow 2H_2O + O_2 + 4e^-$ $2NiOOH + H_2O \rightarrow 2Ni(OH)_2 + {}^1/_2\,O_2$

Figure 2.1: Working principle of Ni-Fe battery with associated reactions.

The nickel electrode is the positive electrode (see red sign Figure 2.1) and the iron electrode is the negative electrode (black sign). Chemical reactions which include electron transfer from one reactant to another, and thus cause a change in the oxidation state of the reactants, are called reduction-oxidation reactions, or in short redox reactions. Since oxidation (the loss of electrons, an increase of oxidation number) always occurs at the anode, and reduction (the gain of electrons, a decrease of oxidation number) always occurs at the cathode, the sites of the anode and cathode change when reversing the electron flow. In other words, when switching from discharging to charging or vice versa. Redox-reactions are balanced reactions. This means, that the oxidation of one atom is accompanied by the reduction of another atom.

Discharging a battery is a spontaneous redox-reaction; the difference in Gibbs free energy (ΔG) is less than 0. At the anode, metallic iron (Fe^0) is oxidized to iron-hydroxide (Fe^{2+} in $Fe(OH)_2$) whereas at the cathode nickel-oxyhydroxide (Ni^{3+} in NiOOH) is reduced to nickel-hydroxide (Ni^{2+} in $Ni(OH)_2$). Electrons flow from the anode to the cathode through an external circuit. The alkaline electrolyte closes the circuit as hydroxyl ions flow from the cathode to the anode. The released chemical energy can be used to perform electrical work, e.g. to power a light bulb. This type of cells where spontaneous redox-reactions ($\Delta G<0$) occur, is also called a Galvanic or Voltaic cell.

Charging on the other hand, is a forced redox reaction; the difference in Gibbs free energy is greater than 0. This means that electrical energy is required to drive the chemical processes inside the battery. At the anode nickel-hydroxide ($Ni(OH)_2$) is oxidized to nickel-oxyhydroxide (NiOOH), whereas at the cathode iron-hydroxide ($Fe(OH)_2$) is reduced to iron (Fe). Electrons flow again from the anode to the cathode via an external circuit and the alkaline electrolyte closes the circuit. This type of cells, where energy is required ($\Delta G>0$) to drive the redox reaction, is called an electrolytic cell.

Electrolysis is also a forced redox reaction, so the cell operates as an electrolytic cell. However, not the state of the electrode material is changed, but water is decomposed. At the Iron (negative) electrode, H_2O is reduced to H_2 and OH^- ions, while at the Nickel (positive) electrode OH^- ions are oxidized to H_2O and O_2. The Nickel electrode operates as anode, the Iron electrode as cathode, the same configuration as during charging.

The state of charge (SoC) of a battery is the ratio of available discharge energy to the discharge energy of a fully charged battery. A value of 1 (=100%) is equivalent to a fully charged battery while a value of 0 (=0%) is equivalent to a completely discharged battery.

2.1.2 Gibbs free energy, cell potential and Nernst equation

The Gibbs free energy is defined as:

$$G = H - TS \tag{1}$$

where G equals the Gibbs free energy, H the Enthalpy, S the Entropy, and T the absolute temperature. The Enthalpy H is related to the internal energy U via the following equation where p stands for pressure and V for volume.

$$H = U + pV \tag{2}$$

which leads to:

$$G = U + pV - TS \tag{3}$$

and to dG the differential of G:

$$dG = dU + pdV + Vdp - TdS - SdT \tag{4}$$

The 1st law of Thermodynamics states that energy is conserved:

$$dU = \delta Q + \delta W \tag{5}$$

The change in internal energy equals the amount of heat transfer (δQ) plus the amount of work (δW) added. Work can be pressure work (-pdV), electrical work (EdQ), or adding mass work ($\Sigma \mu_i dn_i$). Considering a reversible process δQ can be substituted by TdS. This results in the following equation for dU when electrical work is not considered:

$$dU = TdS - pdV + \Sigma \mu_i dn_i \tag{6}$$

Substituting equation (6) into equation (4) leads to the differential equation for the Gibbs free energy:

$$dG = Vdp - SdT + \Sigma \mu_i dn_i \tag{7}$$

When the pressure and the temperature are constant ($dp = 0$ and $dT = 0$) the equation reduces to:

$$dG = \Sigma \mu_i dn_i \tag{8}$$

This means, that the change in Gibbs free energy is equal to the chemical potential times the change of amount of matter. At equilibrium dG equals 0. A process is called a spontaneous process when dG is smaller than 0, whereas a process is called non-spontaneous when dG is larger than 0.

The potential E of an electrochemical cell is related to Gibbs free energy, the relationship is displayed by the following equation:

$$dG = -nFE \quad (9)$$

where *n* represents the number of moles of electrons (without units) and *F* is Faraday's constant (*F* = 96 485 C/mol). The Gibbs free energy at standard conditions (ΔG^0) (1 bar and 1 molar) is related to the Gibbs free energy at non-standard conditions (ΔG) by the following equation:

$$\Delta G = \Delta G^0 + RTlnK \quad (10)$$

where *K* is the reaction quotient of the mixture of interest. Substitution of equation (9) into equation (10) leads to the Nernst equation:

$$\Delta E = \Delta E^0 - \frac{RT}{nF} lnK \quad (11)$$

Expressing the equation in terms of a base-10 logarithm and filling in the values for R (=8.314 J/(mol.K)) F and T (=298 K) leads to:

$$\Delta E = \Delta E^0 - \frac{2.303RT}{nF} logK = \Delta E^0 - \frac{0.0592}{n} logK \quad (12)$$

At standard conditions K equals 1, therefore $\Delta E = \Delta E^0$. ΔG^0 and ΔE^0 are usually tabulated values for 25°C. The Gibbs free energy can be calculated for different temperatures by applying equation (1).

The standard cell potential can be calculated with the following equation:

$$\Delta E^0 = E^0_{red}(cathode) - E^0_{red}(anode) \quad (13)$$

where E^0_{red} represents the standard reduction potential.

2.1.3 Electrolysis and water consumption

Electrolysis is the decomposition of water into its components hydrogen and oxygen.

$$2H_2O \rightarrow 2H_2 + O_2 \quad (14)$$

The overall reaction for water splitting or electrolysis can be decomposed in two half reactions, one at the anode and one at the cathode:

Fe - cathode: $$2H_2O + 2e^- \rightarrow H_2 + 2OH^- \quad (15)$$

Ni - Anode: $$4OH^- \rightarrow 2H_2O + O_2 + 4e^- \quad (16)$$

The cell potential at 25˚C equals E^0_{cell} = 1.229V. The cell potential is constant for different concentrations of pH, however both half-cell reaction-potentials shift the same way according to the Nernst equation with changes of the pH value:

$$E_{H_2} = -\frac{2.303RT}{F} pH \quad (17)$$

$$E_{O_2} = 1.229 - \frac{2.303RT}{F}pH \quad (18)$$

At pH 14 the potentials result in E_{H_2} = -0.829 V and E_{O_2} = 0.4V.

However, applying just the cell potential is not enough to perform electrolysis. As both hydrogen and oxygen experience a phase change from the liquid phase to the gas-phase the entropy of the system increases. To compensate for the entropy change additional energy (TdS, see equation (1)) is required. The thermo-neutral potential is defined in a way that takes both the change in chemical energy and the change in Entropy into account:

$$E_{thermo-neutral} = -\frac{\Delta H_0}{nF} = -\frac{\Delta G_0 + T_0 \Delta S_0}{nF} \quad (19)$$

Table 2.1 provides an overview of thermodynamic properties for electrolysis. The enthalpy and the thermo-neutral potential hardly change with increasing temperature while the Gibbs free energy and the cell potential slightly decrease with increasing temperature.

Table 2.1: G_0, H_0, E_0 and $E_{thermo-neutral}$ for electrolysis at different temperatures

Temperature		25°C	30°C	35°C	40°C
ΔG_0	[J/mol]	237.1	236.3	235.5	234.7
ΔH_0	[J/mol]	285.8	285.7	285.5	285.4
E_0	[V]	1.2289	1.2247	1.2204	1.2162
$E_{thermo-neutral}$	[V]	1.4812	1.4804	1.4795	1.4787

The amount of gas production is related to the amount of charge inserted. One Ampere-hour (Ah) can be converted to Coulomb (C, 1 Ah = 3600 C) by multiplying Amperes (C/s) by seconds/hour (3600). This number can further be converted to moles of electrons by dividing by Faraday's constant. This leads to:

$$1\ Ah \propto 3{,}600\ C \propto \frac{3{,}600\ C}{96{,}485\frac{C}{mol}} = 0.0373\ mol\ (e^-) \propto 0.01866\ mol\ (H_2O) \propto 0.336\ g\ (H_2O)$$

Four electrons are required to produce oxygen, two to produce hydrogen. This finally results in the production of 0.0093 moles of oxygen (O_2) and 0.0186 moles of hydrogen (H_2) per Ah of inserted charge. In other words, 0.0186 moles of H_2O can be split by inserting 1Ah of charge. The molar weight of H_2O is 18.02g/mol, so decomposing water with 1Ah charge insertion causes a water consumption of 0.336 g H_2O.

The ideal gas law relates the volume of a gas to the number of moles under given environmental conditions (temperature and pressure). The ideal gas law is given by:

$$pV = nRT \quad (20)$$

R represents the universal gas constant (R=8.3145 J/(mol.K)). Under lab conditions (25°C = 298,15K; 1atm =101325Pa) the volume of one mole of gas results in:

$$V = \frac{nRT}{p} = \frac{8.3145 * 298.15}{101{,}325} * 1000 = 24.5 \frac{l}{mol}$$

The following gas flow-rates can be expected when performing electrolysis at a charge rate of 1 A:

Table 2.2: Gas-flow rate for a charge rate of 1 A

Charge rate [A]	Oxygen flow-rate [ml/min]	Hydrogen flow-rate [ml/min]
1	3.8	7.6

2.2 Working principle and components of the Nickel-Iron battery

The nickel-iron battery consists of a positive electrode, which uses nickel as its active material, and a negative electrode, which uses iron. The overall reaction is given by:

$$Fe + 2NiOOH + 2H_2O \underset{Charge}{\overset{Discharge}{\rightleftarrows}} Fe(OH)_2 + 2Ni(OH)_2 \quad (21)$$

Water is decomposed during discharging, to form iron hydroxide and nickel hydroxide, while water is released during charging to form iron and nickel oxyhydroxide. Consequently, the concentration and density of the electrolyte change slightly during one cycle, as well as the filling level.

The charging/discharging of the iron electrode is a two-step process characterized by the following equations:

$$Fe + 2OH^- \underset{Charge}{\overset{Discharge}{\rightleftarrows}} Fe(OH)_2 + 2e^- \quad (22)$$

$$Fe(OH)_2 + OH^- \underset{Charge}{\overset{Discharge}{\rightleftarrows}} FeOOH + H_2O + 2e^- \quad (23)$$

The standard potentials for both reactions are -0.88 V and -0.55V relative to the standard hydrogen potential (SHE). Normal operation is limited to reaction (22) due to the higher potential of this reaction and the limited reversibility of reaction (23). In the process of reaction (22), iron changes its oxidation state from 0 to +2.

Reaction (22) is a heterogeneous mechanism with the dissolute intermediate $HFeO_2^-$ that can be described by (for solubility of $HFeO_2^-$ see chapter 2.2.2.2):

$$Fe + 3OH^- \rightleftarrows HFeO_2^- + H_2O + 2e^- \quad (24)$$

$$HFeO_2^- + H_2O \rightleftarrows Fe(OH)_2 + OH^- \quad (25)$$

The charging/discharging of the nickel electrode can be characterized by the following equations:

$$NiOOH + H_2O + e^- \underset{Charge}{\overset{Discharge}{\rightleftarrows}} Ni(OH)_2 + OH^- \quad (26)$$

In the process of reaction (26), nickel changes its oxidation state from +3 to +2. The standard potential of the electrode is 0.49 V relative to SHE. The total cell voltage, resulting from the standard potentials of both electrodes, is 1.37 V.

The overall reaction is electrochemically balanced if the electrodes are present in the ratio of Fe/Ni = 1/2. Normally cells are arranged in such a way that the nickel electrode is the limiting electrode (Ni). [2]

The electron transfer is directed through an external circuit, which is connected to both electrodes, while the alkaline electrolyte completes the system by providing hydroxide conductivity. KOH and NaOH in combination with LiOH are used as electrolytes. KOH has a higher conductivity, while NaOH is cheaper and easier to handle. Operation at low temperature requires KOH in higher concentrations as the electrolyte. LiOH is added for its stabilizing effect on the capacity of the positive electrode during charge/discharge cycles. LiOH minimizes the coagulation of the active material [2, 3]. LiOH is added to all the available Nickel-Iron batteries, as they are built up of pocket type electrodes. However, LiOH is not applied in the case of Nickel-Cadmium batteries operating with sintered electrodes, because of the high stability of these types of electrodes.

2.2.1 Advantages and disadvantages of the nickel-iron battery

Nickel-iron batteries, also known as “Edison cells”, are known for their long lifetime. Such cells can be operational for as much as 80 years after having been produced [4]. They are known as being almost indestructible. Besides, they can withstand electrical abuse in the form of over-charge and deep discharge; discharge stands for extended periods and short-circuiting. Therefore applications where high cycle-lives and/or repeated deep discharge are required are ideal for these batteries. Several poor performance indicators historically formed the main drawback of these batteries. This led to a loss in market shares from the 1970s on. A low power density, poor low-temperature performance, poor charge retention, and gas evolution on stand are the main limitations. Last but not least, Ni/Fe batteries are costlier than lead-acid batteries. These drawbacks led to the near-extinction of this type of batteries [3].

Nickel-Iron batteries suffer from self-discharge, rates of 1-1.5 % per day are common [5]. The self-discharge is a result of the hydrogen evolution reaction (HER) occurring at the iron electrode, and of the oxygen evolution occurring at the nickel electrode:

$$Fe + 2OH^- \rightleftharpoons Fe(OH)_2 + 2e^- \quad (22)$$

$$2H_2O + 2e^- \rightleftharpoons H_2 + 2OH^- \quad (27)$$

$$2NiOOH + H_2O \rightleftharpoons 2Ni(OH)_2 + \frac{1}{2}O_2 \quad (28)$$

Reaction (22) characterizes the charging/discharging of the electrode. Reaction (28) shows the hydrogen evolution reaction with a standard potential of -0.827 V. Combining reactions (22)and (28) leads to:

$$Fe + 2H_2O \rightarrow Fe(OH)_2 + H_2 \quad (29)$$

which means that the iron electrode is not stable in an alkaline environment due to the lower potential of the hydrogen evolution reaction. Hydrogen evolution, also known as corrosion, occurs under charging conditions and on stand.

The faradaic efficiency - the ratio of retrieved charge to inserted charge - is 60% to 80%, depending on the charging rate. Faster charging results in higher gas production. Due to the gas production the amount of water in the electrolyte decreases, so regular watering is required to keep the electrolyte above a minimum level. Exposure of the electrodes to air would lead to irreversible

damage. The requirement for regular maintenance precludes the use of these batteries as stand-alone devices.

2.2.2 Past and current developments

Nickel Iron batteries are known for their physical indestructibility and for their resistance to electrical abuse. However, hydrogen evolution was identified as a major drawback, and efforts were made to solve this problem. Furthermore, the high internal resistance, due to the limited conductivity of the active material, is known, and attempts have been made to improve the conductivity.

2.2.2.1 Nickel electrode

The first nickel electrodes were pocket and tubular types. The active material was mixed with conductive material, nickel flakes or graphite, and inserted into the pocket/tube. The Nickel-electrode experiences a substantial volumetric change during the charge/discharge process, which necessitated these robust electrode types. Nowadays, nickel-iron batteries are equipped with pocket electrodes because of their low cost.

A small amount of Cobalt hydroxide (5wt%) is often added to increase capacity and cycle-life. The addition of cobalt reduces electrode swelling and raises the overpotential at which oxygen is liberated [6].

Sintered nickel electrodes have been developed for Nickel-Cadmium batteries, however these types of electrodes were not applied to Nickel-Iron batteries. Nickel-Cadmium batteries behave differently from Nickel-Iron batteries; the oxygen evolution occurring at the positive electrode is a weakness, not the hydrogen evolution. Therefore, the positive nickel electrode had to be improved. The sintered electrode type increases both the stability and the conductivity of the electrode.

Both nickel hydroxide and nickel oxyhydroxide exist in different phases. Batteries usually employ the β/β couple, which is characterized by a layered structure with an interslab distance of about 4.6/4.8 Å respectively. The interspacing distances match well, which explains the high cycle life of Ni - electrodes, as the material hardly experiences structural changes during charging/discharging [7]. Upon overcharge γ- NiOOH forms from β- NiOOH. A layer of H_2O is incorporated into the structure and the lattice distance increases to 7 Å. The γ- NiOOH forms a cycling couple together with the α- $Ni(OH)_2$ phase with a lattice constant of 8 Å. However, the α-phase is not stable in alkaline electrolyte and alters back to the β-phase [8].

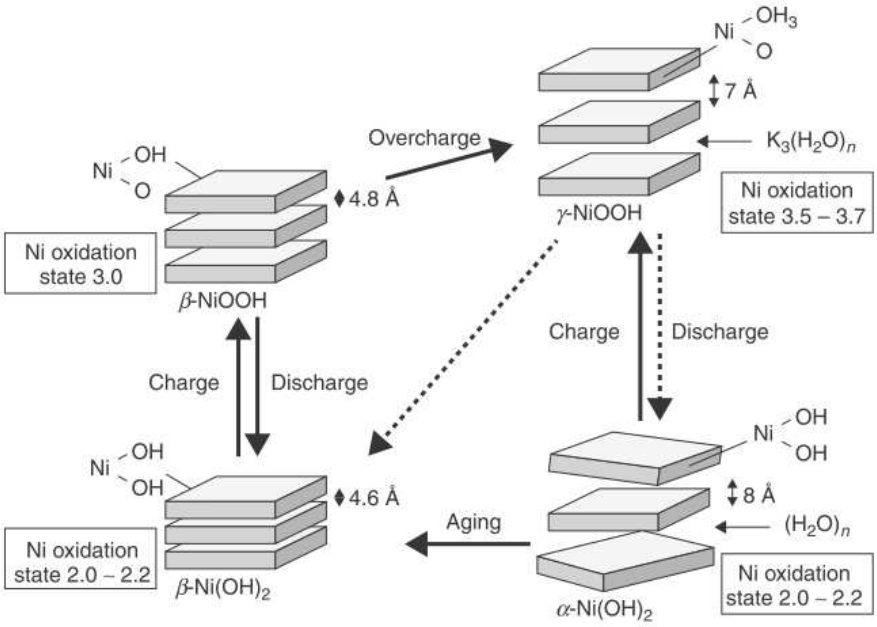

Figure 2.2: Bode diagram illustrating the phase transformation of nickel hydroxide/oxyhydroxide with various Ni oxidation states [9].

It is advantageous to utilize the α/γ couple as the difference in oxidation state increases. In other words, less active material is required for the same storage capacity.

$Ni(OH)_2$ is a proton conductor, not an electrical conductor, while NiOOH conducts both protons and electrons. Upon charge, protons from inside the structure move towards the electrode/electrolyte interface, forming NiOOH at the current collector. Continued charging shifts the $Ni(OH)_2$/NiOOH front also to the electrode/electrolyte interface. Oxygen evolution occurs only if the electrolyte is in contact with NiOOH, meaning that the electronic circuit is closed [7].

2.2.2.2 Iron electrode

Iron electrodes have been developed and tested in the form of sintered, pocket and rolled electrodes [10-13]. Rolled electrodes are cheaper than sintered electrodes and they outperform the pocket type. However, sintered electrodes show the best performance. Sintered electrodes were developed to serve as electrodes in iron-air batteries for vehicle propulsion around 1980 [14].

One of the first studies concerning the corrosion rates of the alkaline iron electrode concludes that adding additives to the active material before sintering does not seem to significantly decrease corrosion rates, but that additives in the electrolyte do have a considerable effect [15]. The temperature dependence of the iron electrode was investigated by the same author. The discharge capacity of the electrodes was found to increase with increasing temperature. Furthermore the solubilities of the intermediate ions ($HFeO_2^-$ and FeO^{2-}) increase with increasing temperature. This explains the poor performance at low temperatures, and increased self-discharge at high temperatures [16, 17]. The solubility of $HFeO_2^-$ and FeO^{2-} at varying temperatures is depicted in Figure 2.3.

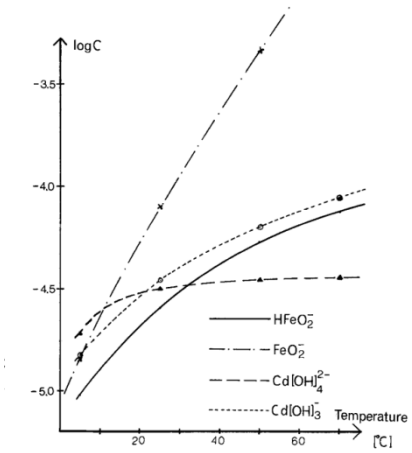

Figure 2.3: Calculated solubilities in 5M KOH of Fe and Cd ions at different temperatures [17].

The additive Bi_2S_3 decreases the activation barrier of the iron discharge reaction, which increases the reversibility of the reaction. Furthermore, this additive suppresses the evolution of H_2 [12]. Another way to decrease the hydrogen evolution from the iron electrode is to add FeS to the active material, or Na_2S to the electrolyte. Besides the depression of hydrogen evolution during charging, the capacity of the electrode is enhanced, while the self-discharge during storage is suppressed [18].

Other concepts mainly aiming to decrease the hydrogen evolution for a better performance of the iron electrode are:

- the self-assembling of a monolayer of n-Alkanethiols [19]
- the addition of bismuth/bismuthsulfide [20-22]

2.2.2.3 Other developments

Two more research directions have been identified, firstly to investigate nano-scale electrodes to improve their performance characteristics [23, 24], and secondly the development of sealed batteries to eliminate maintenance [25]. The second direction employs a combination of reduced gas evolution and the addition of a ceria-supported platinum catalyst to recombine oxygen and hydrogen to make a sealed arrangement possible.

2.2.3 Available batteries

Three companies that currently produce Nickel-Iron batteries have been identified: Changhong in China, Kursk in Russia and Ukr Bat in the Ukraine.

The Batteries manufactured by Changhong are pocket-type batteries that use potassium hydroxide and lithium hydroxide as electrolyte. Batteries with a rated capacity of 10Ah up to 1000Ah are offered for sale [26]. For this research we purchased batteries from Changhong with a rated capacity of 10Ah.

The batteries manufactured by Kursk Plant are also pocket type batteries. Depending on the battery's size, a solution of sodium hydrate containing lithium hydroxide or a potassium solution containing lithium hydroxide is applied. The rated capacities range from 250Ah up to 950Ah [27].

The company Ukr Bat manufactures cells from 250Ah up to 550Ah. No information is available about the type of cells or electrolyte used in these batteries. [28].

2.3 Alkaline electrolyzes

Electrolysis produces hydrogen with high purity and few contaminants. This is an advantage over hydrogen production from fossil fuels, which dominates the market. Different techniques are available for electrolysis. This section is limited to the alkaline electrolysis, the most applied and mature technology. Compared to other electrolysis technologies alkaline electrolysis has the advantage that it uses abundant materials [29].

An electrolysis setup consists of electrodes and a diaphragm for gas separation. These are immersed in alkaline electrolyte. Hydrogen evolves at the cathode, oxygen at the anode. The diaphragm separates the evolving gasses while it allows the hydroxyl ion transport required for the process.

Electrolyzers operate at cell temperatures between 60°C and 80°C and at pressures up to 30 bar. The alkaline electrolyte consists of a 30wt% potassium hydroxide (KOH) solution, the concentration with highest conductivity. Alkaline electrolyzers operate at a current density up to 0.4 A/cm² [30].

Asbestos was often used as material for the diaphragm. Research is ongoing to replace asbestos, because of its toxicity and its high resistance. A modern alternative is Zirfon® Perl, a porous membrane, which is considered state of the art. It is built up as a composite of a polysulphone network (15%) with zirconium oxide as an inorganic filler (85%). For technical information see [31]. Advanced membranes, constructed from two single layers of Zirfon® with an intermediate free electrolyte channel to reduce gas crossover, are currently being developed [32].

The main active components are Ni metal-based electrodes. Other metals, such as Fe, Co, and Mo, can be incorporated to increase the catalytic activities for oxygen and hydrogen evolution [33, 34].

Operation at high pressure is worthwhile, as compressing the initial liquid costs much less energy than compressing the produced gasses. Furthermore, the size of the gas bubbles is reduced and a larger amount of gas can be dissolved in the electrolyte. Smaller gas bubbles increase the conductivity of the electrolyte, since gas bubbles are not conductive. Dissolving more gas in the electrolyte does have a disadvantage: gas crossover through the diaphragm increases proportional to the partial pressures of the gasses [30].

Hydrogen production by electrolysis leads to hydrogen with high purity, only containing oxygen and water vapor as impurities. Oxygen is not generally a useful product, as extraction from air is simpler. Purification of hydrogen should only be applied if necessary for the application, as this step results in 5-10% loss of hydrogen and therefore loss in efficiency [35].

2.4 Pourbaix diagrams

In chapter 2.1.3 the Nernst equations for oxygen evolution and hydrogen evolution were presented. In the same way the equilibrium conditions for charging and discharging the electrodes can be derived. Figure 2.4 and Figure 2.5 display Pourbaix diagram for an iron-water system at 25˚C. The first one considers Fe_3O_4, the second one $Fe(OH)_2$ next to Fe in the area of interest. Equation (31) and (32) show the belonging equilibrium potentials.

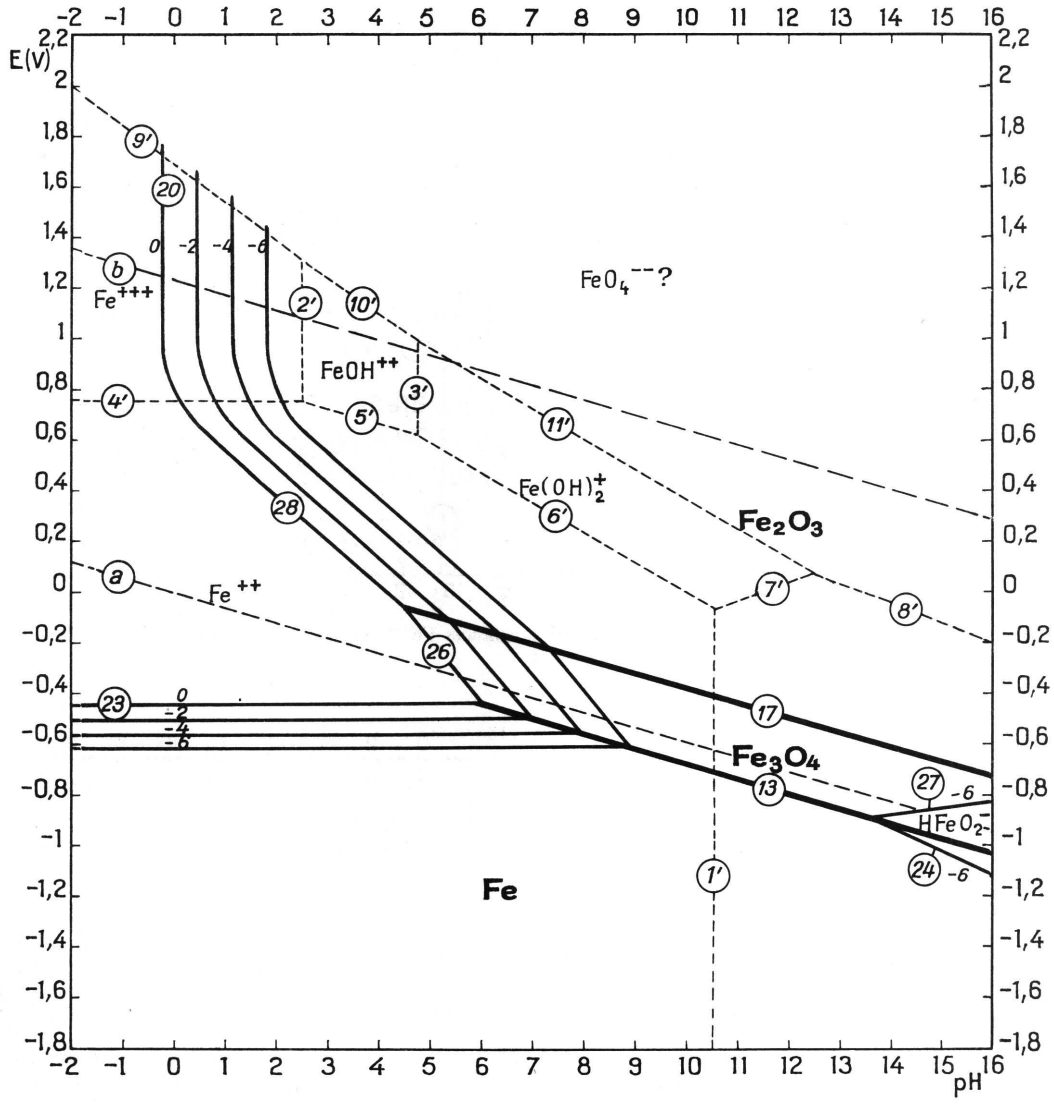

Figure 2.4: Potential-pH equilibrium diagram for system iron-water, at 25˚C (considering as solid substance only Fe, Fe_3O_4 and Fe_2O_3). [36]

Line 13 in Figure 2.4 represents the following reaction with the corresponding potential:

$$3Fe + 4\,H_2O = Fe_3O_4 + 8H^+ + 8e^- \quad (30)$$

$$E_{Fe \Leftrightarrow Fe_3O_4} = -0.085 - 0.0591pH \quad (31)$$

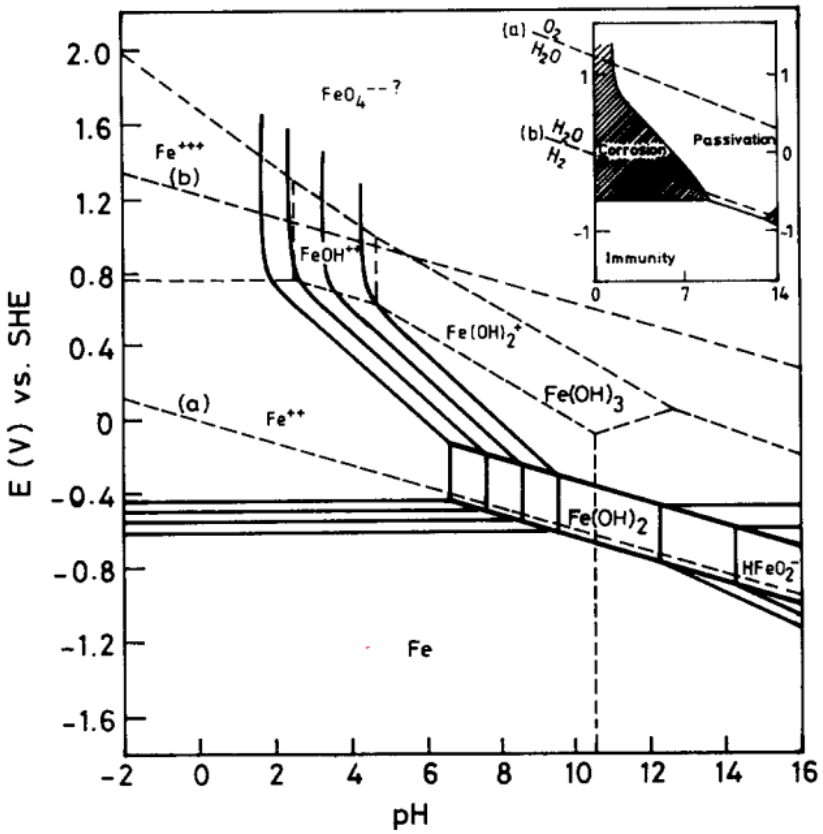

Figure 2.5: Potential-pH equilibrium diagram for system iron-water, at 25˚C (considering $Fe(OH)_2$) [37]

The Nernst equation for charging the iron electrode ($Fe(OH)_2$ -> Fe, see equation (22)) is given by [38]:

$$E_{Fe \Leftrightarrow Fe(OH)_2} = -0.0633 - \frac{2.303RT}{F} pH \quad (32)$$

In these diagrams, it can be observed that the equilibrium area for the two compounds Fe_3O_4 and $Fe(OH)_2$ are in the same region, where Fe_3O_4 is thermodynamically considered to be more stable [37]. Transformation occurs according to the Schikorr reaction:

$$3Fe(OH)_2 \rightarrow Fe_3O_4 + 2H_2O + 8H^+ + 8e^- \quad (33)$$

This reaction is reported to be slow at low temperatures but fast at high temperatures [39].

The potentials shift with pH, and are lower than the potential for hydrogen evolution (see line(a) in Figure 2.4 and in Figure 2.5).

Figure 2.6 shows the dependence of the potential on the pH of a nickel water system. Phase (III) represents $Ni(OH)_2$ and (V) represents NiOOH. Equation (26) describes the pH dependence. Regarding lines (a) and (b), it should be mentioned that they are obviously drawn incorrectly as the potential for oxygen evolution should be 0.045 V and the potential for hydrogen evolution should be -1.184 V at a pH value of 20. The potentials at pH 0 are correct. The corrected lines are added to the figure (red lines).

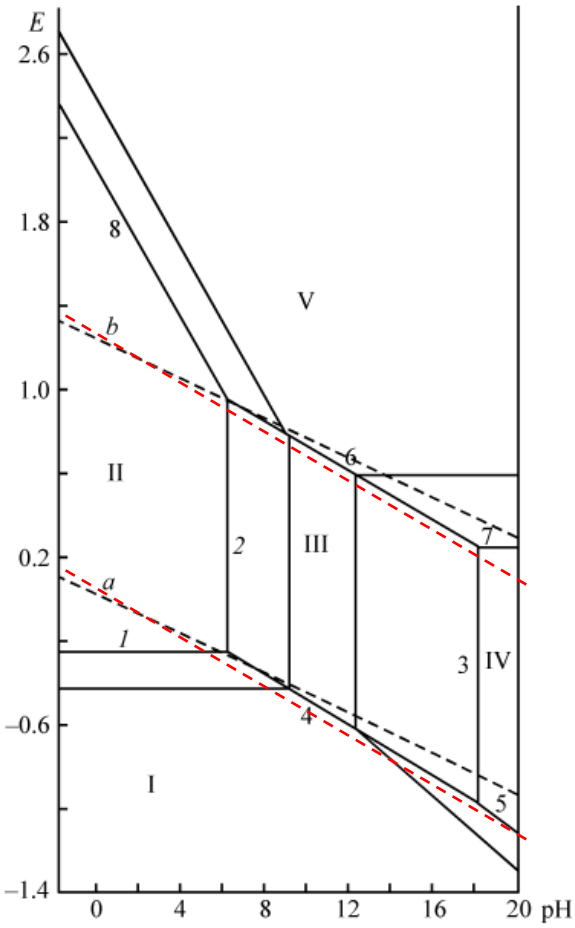

Figure 2.6: Dependence of potential E(V) on pH for the nickel-water system containing nickel(III) metahydroxide at 25˚C. (I) Ni, (II) Ni^{2+}, (III) $NI(OH)_2$, (IV)$HNiO^{2-}$,(V) NIOOH. [40] with corrected lines (a) and (b), see red lines

The Nernst equation for charging the nickel electrode ($Ni(OH)_2$ -> NiOOH, see equation (26) is given by [40]:

$$E_{NiOOH \Leftrightarrow Ni(OH)_2} = 1.319 - 0.0592pH \quad (34)$$

The potential for oxygen evolution is below the potential for this redox-reaction.

As the potentials for oxygen evolution and hydrogen evolution are both within the potential area of cell operation, gas evolution occurs during charge insertion, and self-discharge takes place when the battery is in the charged state.

Table 2.3: Potentials for cell operation at pH 14 and 25˚C

		$E_{NiOOH \Leftrightarrow Ni(OH)_2}$	$E_{Fe \Leftrightarrow Fe(OH)_2}$	E_{O_2}	E_{H_2}
Potential	[V]	0.49	-0.892	0.40	-0.829

According to these values the cell potential results in 1.382 V. This is in agreement with the reported value of 1.37 V from chapter 2.2. The small deviation is caused by the fact that the potential of the iron electrode is reported to be -0.88V.

Moreover Figure 2.6 shows that the material used for alkaline electrolysis, NiOOH for oxygen evolution at the anode and Ni for hydrogen evolution at the cathode are stable at a potential above respectively below their evolution potential considering some overpotential for oxygen evolution.

2.5 Electrolyte

Ni-Fe batteries and alkaline electrolysis both use potassium hydroxide (KOH) as electrolyte [2, 5, 30].

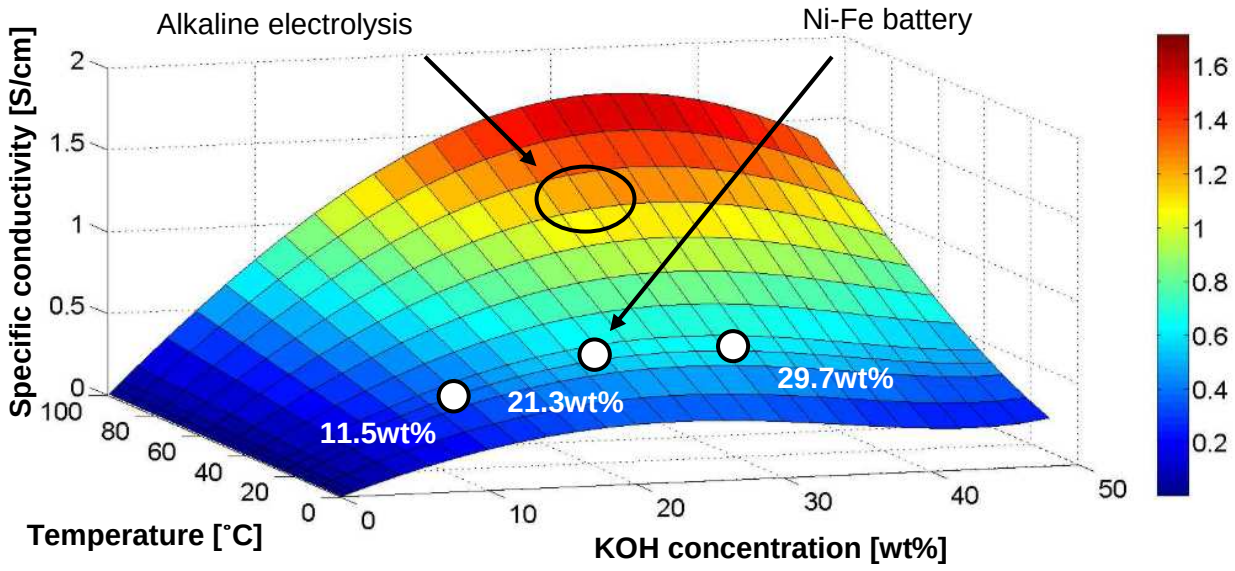

Figure 2.7: Conductivity of KOH, data from [41]

In addition to KOH, Ni-Fe batteries use lithium hydroxide (LiOH) as an additive. The concentration of KOH is around 20wt%. The concentration of LiOH is 4 wt% (50g/l LiOH) for first electrolyte filling, and 2 wt% (25g/l LiOH) for electrolyte replacement [2, 5]. Recent instruction manuals [42, 43] specify the density of battery KOH electrolyte as 1.2 g/ml. This corresponds to a concentration of 21.25 wt% KOH. Furthermore, 20g/l to 40 g/l of $LiOH.H_2O$ has to be added to the electrolyte.

KOH is preferred due to its high specific conductivity, the highest among alkaline electrolytes [44]. An electrolyte with a concentration of 21.25 wt% KOH at 25˚C (4.53M) possesses a specific conductivity of 0.60 S/cm. Increasing the molarity by 50% to 6.79 M (29.7 wt%) increases the conductivity to 0.62 S/cm, this is close to the maximum conductivity of 0.63 S/cm at 28wt%. However, from the figure and the values it can be deduced that there is hardly any variation in conductivity between 21wt% and 30wt%. Decreasing the molarity by 50% to 2.27M (11.5wt%) leads to a significant reduction in conductivity to 0.41 S/cm. The conductivity of KOH at 70˚C and 28wt%, typical operational parameters for electrolysis, is 1.22 S/cm, two times higher than for normal battery operation.

The addition of LiOH is reported to have a beneficial effect, especially on the nickel electrode. It stabilizes the positive electrode, extending its cycle life and its capacity. The content of LiOH is limited as it reduces to conductivity of the electrolyte. [2, 3, 5].

An alternative to KOH is sodium hydroxide (NaOH). It has a lower conductivity, the maximum value at 25˚C is 0.4 S/cm at 20wt% NaOH [30]. Russian supplied Ni-Fe batteries [45] operate with sodium hydroxide as electrolyte and also contain LiOH.

Another compound that is added to the electrolyte is sodium sulfide (Na_2S). [46] Sulfide attaches to the iron electrode surface and improve the discharge kinetics. The combination of NaOH, LiOH, and Na_2S (1-2wt%) is claimed to further improve charge efficiency, charge retention and cycle life of Ni-Fe batteries [47].

Carbon dioxide from the air in combination with the hydroxyl ion can form carbonate plus water.

$$CO_2 + 2OH^- \rightleftharpoons CO_3^{2-} + 2H_2O \quad (35)$$

Carbonate plus the potassium ion form the salt K_2CO_3. This characteristic is also known and applied in alkaline CO_2 removal systems and forms an adverse effect for alkaline fuel cells as it means that air cannot be used directly as reactant. Carbonate causes the following effects [44]:

1. reduced OH- concentration interfering with kinetics
2. electrolyte viscosity increases, resulting in lower diffusion rate and lower limiting currents;
3. precipitation of carbonate salts in the porous electrode, reducing mass transport
4. reduced oxygen solubility
5. reduced electrolyte conductivity

In short, the electrodes become sluggish and the electrode's capacity decreases [16, 17]. Beyond a certain carbonate concentration, electrolyte replacement is required for the Ni-Fe batteries.

The oxygen evolution at the anode of the nickel-iron battery can also lead to the formation of carbon dioxide if the electrode contains carbon. Carbon is a good conductor and is therefore applied to increase the electrode's conductivity of pocket and tubular types of nickel-iron batteries. The application of sintered electrodes avoids the carbon component and its potentially negative effects.

2.6 Efficiency, kinetics and losses

The Nernst equation (10) defines the potential for equilibrium conditions. When operating, cell overpotentials (polarization) occur. Overpotentials cause losses and decrease the efficiency. The next two subchapters explain the cause of overpotentials, and define the efficiency of the battolyzer.

2.6.1 Overpotential

Three separate terms contribute to voltage losses through overpotential [2]:

1. η_o = ohmic polarization
2. η_c = concentration polarization (mass-transfer limiting)
3. η_a = activation polarization (charge-transfer limiting)

Ohmic losses are caused by resistances of the electrolyte, the membrane, or the electric circuit. Ohmic losses are also called IR losses, as these losses scale with the applied current (I) and the resistance (R). They are equal to zero when no current is applied.

Concentration overpotentials are also current - to be precise current density - dependent. The following equation defines the relationship between current density, limiting current density, and overpotential [2]:

$$\eta_c = \frac{2.303RT}{nF}\log\left(1 - \frac{i}{i_{lim}}\right) \quad (36)$$

The limiting current density i_{lim} depends, among others, on the diffusion coefficient, the diffusion layer thickness, and the concentration of the electroactive species. Because of the log-term in equation (36): the contribution of concentration overpotentials is low at low currents and significant at high currents, both relative to the limiting currents.

The kinetics of electrochemical charge transfer with activation overpotential for each electrode can best be described by the Butler-Volmer equation [48]:

$$i = i_0\left\{exp\left[\frac{\alpha zF\eta}{RT}\right]_f - exp\left[-\frac{(1-\alpha)zF\eta}{RT}\right]_r\right\} \quad (37)$$

At equilibrium the overpotential is zero. Furthermore, the forward and reverse current are equal, and the net current flow is zero. Both currents are equal to i_0, the exchange current density. A high value for i_0 indicates faster kinetics. The other parameters have the usual meaning, α is the transfer coefficient.

Two limiting cases for the Butler-Volmer equation are important: low overpotentials and high overpotentials. In the case of low overpotentials a Taylor expansion performed for exp(x), and ignoring higher order terms leads to:

$$i \cong i_0\left(\frac{zF\eta}{RT}\right) \quad (38)$$

In the case of high overpotentials the forward current density outperforms the reverse current density, leading to:

$$i = i_0\left(exp\left[\frac{\alpha zF\eta}{RT}\right]_f\right) \quad (39)$$

Equations (39) can be rewritten to

$$\ln(i) = \ln(i_0) + \frac{\alpha zF\eta}{RT} \quad (40)$$

Equations (38) and (40) can serve for interpretation of Tafel plots, graphs were the overpotential is plotted against the natural logarithm of the current density.

2.6.2 Efficiency

The energy efficiency η_{total} for each charge and electrolysis and subsequent discharge cycle is calculated from the equations:

$$\eta_{total} = \eta_{battery} + \eta_{electrolyser} \quad (41)$$

$$\eta_{battery} = \frac{\int_{t_c}^{t_c+t_{dc}} V_{dc}I_{dc}dt}{\int_0^{t_c} V_cI_cdt} = \frac{E_{dc}}{E_c} \quad (42)$$

$$\eta_{electrolyser} = \frac{\int_0^{t_c+t_{dc}} H_{el}I_{el}dt}{\int_0^{t_c} V_cI_cdt} = \frac{1.48(C_c - C_{dc})}{E_c} \quad (43)$$

V_c, I_c are the applied cell voltage and current during the charge and electrolysis cycle with duration t_c, E_c the resulting energy during these cycles, V_{dc} and I_{dc} are the discharge voltage and current

during the discharge time t_{dc}, and E_{dc} the discharge energy, I_{el} the current for electrolysis (and hydrogen evolution induced battery self-discharge) with an energy yield corresponding to the thermo-neutral potential H_{el}. The H_{el} equals 1.48 V at room temperature (RT) while 2eH_{el} equals the higher heating value of hydrogen of -286 kJ/mol H_2. I_{el} results from the difference between the total current inserted in the battery electrolyzer and the subsequent integrated current during discharge:

$$C_c = \int_0^{t_c} I_c dt = \int_0^{t_c+t_{dc}} I_{el} dt + \int_{t_c}^{t_c+t_{dc}} I_{dc} dt = C_{el} + C_{dc} \quad (44)$$

A cycle is counted from full discharge to full discharge with various full or partial (over/dis)charge programs within the indicated cycle. As a consequence the cycle discharge capacity can exceed the normal battery discharge capacity as the monitored discharge capacity is the sum of all sub-cycle discharges and the final full discharge.

2.7 Theory on experimental methods

This section presents a brief overview of the used experimental methods with their theoretical background.

2.7.1 Electrochemical measurements

The following methods have been applied for Electrochemical measurements:

- Chronopotentiometry (CP)
- Galvanostatic Electrical impedance spectroscopy (EIS)

Chronopotentiometry is a technique where a constant current is applied to an electrochemical cell and the cell potential is measured. CP is applied for charging and discharging the cell. The amount of inserted charge was regulated by changing the charging time. The discharge was regulated by ending the discharge based on a threshold cell voltage, 1.1 V for standard cycles.At the end of the discharge, the next charging cycle could be started. However, for tests concerning fast cycling and switching, time was the default value for discharging steps as well.

Galvanostatic EIS is a technique to determine the impedance (Z) of a system by applying a sinusoidal (AC) current across a cell and measuring the resulting AC potential along with phase shifts between the AC voltage and the AC current.

A multichannel Maccor 2000 battery cycling system for CP, and a potentiostat 4000, as well as Parstat MC: PMC-1000 for CP and EIS were used to perform the experiments.

2.7.2 Material Characterization

The following methods have been applied for material characterization:

- X-Ray Diffraction (XRD)
- Scanning Electron Microscopy (SEM) and Energy-dispersive X-ray spectroscopy (EDS)
- Inductively Coupled Plasma Optical Emission Spectrometry (ICP OES)

XRD is a technique to determine the crystalline phases as well as their particle size and lattice parameters. For the measurements the X-Ray diffractometer Bruker D8 Advance was used, all samples were powder samples.

SEM together with EDS was applied to visualize and determine the material composition and structure.

SEM uses a focused beam of electrons that scans the probe to generate high-resolution images of the sample. This technique is also called secondary electron imaging (SEI). The generated electron beam interacts with the atom at or near the surface. This generates a detectable signal. Conducting probe material leads to increased interaction and signal intensity. A surface coating can be applied to generate high-resolution surface images for non-conductive or weakly conduction material.

EDS is often combined with SEM and operates at higher voltages. EDS usually operates at 20 kV, compared to 5 kV for SEM. The higher voltage beam in the EDS excites electrons from the ground state. X-rays are generated when these excited electrons return to their ground state. These X-rays can be detected. The detected energy corresponds to well-defined energy levels of elements, therefore this technique is suitable to determine the material composition. However, the elements Lithium, Hydrogen and Beryllium cannot be detected.

ICP is a technique to determine trace elements of an aqueous sample. The sample is first converted into a fine mist by a nebulizer. This mist is transferred into a high temperature plasma flame, where it collides with charged ions and electrons. The structure collapses immediately into individual atoms. These atoms then start a cycle of losing and regaining electrons. This process causes the generation of element-specific wavelengths that can be analyzed by optical detectors.

2.7.3 Gas analysis (Hiden)

A Hiden 3F-PIC series Quadrupolar Mass Spectrometer was used for gas analysis. During operation gas molecules are converted to, typically positively charged, particles. The particles are ionized by impact of thermionically emitted electrons from a hot filament. These ionized particles are extracted to a mass filter and analyzed. The Hiden analytical website [49] provides additional information.

Hiden Analytical provides different modules for operation. The following three modules were used for gas detection:

- Profile Mode: Displays shape peaks across a range of masses
- Bar Mode: Displays a histogram of peak intensities across a range of masses
- MID mode: Multiple Ion Detection mode measures selected individual masses

3 Cell design

This chapter describes the design process of the battolyzer. First, the construction of the available Ni-Fe batteries has been studied. The electrodes of this type of battery will be used for the combined cell, so the dimensions of the electrodes determine the minimal compartment size of the combined device. Next, the design requirements with respect to material selection and handling are defined. These inputs then led to the final design.

3.1 Examination of available Ni-Fe battery

Ni-Fe batteries were purchased by the Australian supplier Ironcore Batteries. The cells, with cell type NF10-S and a rated capacity of 10Ah, were manufactured by Sichuan Changhong Battery Co., LTD [26]. The installation and maintenance manual [42] provides essential information about charging, discharging, and maintenance (e.g. replacement of electrolyte).

The batteries were delivered with a small amount of electrolyte. Most of the electrolyte has been removed, and was delivered in a glass jar with a label "6M KOH", which encouraged us to investigate further.

The cell is contained in a sealed, transparent polypropylene container with outer dimensions of 35 mm x 82 mm x 110 mm (length (L) x width (W) x height (H) without terminals and vent). Terminal poles and ventilation vent are located on the top of the battery. After removing the casing the internal structure of the battery was visible (see Figure 3.1).

Figure 3.1: Ni-Fe cell without casing

One battery consists of seven alternating Ni- and Fe- electrodes with separators between each of the plates. The electrode assembly is pressed and kept together with nylon tape. The electrodes

and terminal poles are welded onto a current collecting bar, one for the positive pole and one for the negative pole. All in all, this is a very compact and robust design.

The battery has 4 Nickel electrodes and 3 Iron electrodes, Nickel electrodes are on the outside. The electrode center distance is approximately 4mm, divided over 1mm of separator and 3 mm of electrode thickness. The total width is approximately 30 mm. One single electrode has a height of 85mm (up to the current collecting bar) and a width of 70mm. The active area of the electrodes is 55mm x 65mm (W x H). The active material is placed in the pockets of the electrodes. These pockets are encased by perforated nickel-plated steel plates, which form the visible surface of the electrodes.

3.1.1 Electrolyte

According to the label on the glass jar, the provided electrolyte should be 6M KOH. As a first test the density of the provided electrolyte was measured. It was found to be 1.209 g/ml at 20˚C; 6M KOH should possess a higher density, 1.26 g/ml.

As a next test, the molarity of the electrolyte was determined to be 5.7M, by means of titration. Phenolphthalein was used as indicator, changing color from pink at pH10, to colorless at ph8. 1M nitric acid from the storage cabinet was used as titrant. However, the determined molarity should rather be considered as an upper limit for the molarity than as the real value for the molarity, as the density of the titrant was lower than expected for a 1M nitric acid solution.

SEM/EDS was used to determine the chemical elements of the electrolyte. First, salt deposits around the vents of the batteries were collected and analyzed. Besides potassium, sodium was identified as a main component of the electrolyte. This observation was supported by tests performed with electrolyte that was deposited on carbon paper and vacuum dried (see appendix A). Dependent on the point analyzed all variations of zero potassium and only sodium to only potassium and no sodium have been identified. The composition of the individual crystals was found to vary. Tests were performed with electrolyte dried on carbon paper, but this approach was not successful. The hygroscopic properties of the electrolyte did not allow the probe to be completely dried. Even worse, dried surfaces (which could be analyzed with SEM/EDS under vacuum) turned liquid again while preparing XRD experiments. This led to amorphous test results. Electrolytes with various combinations of Na/K/Li have been prepared for XRD reference purposes, but those did not yield any usable result either.

Finally, ICP was used to determine the electrolyte composition. Two samples were analyzed, one diluted a 100 times, the other one diluted 100*100 times. Table 3.1 shows the detected elements.

Table 3.1: Results ICP measurement

	K [g/l]	Na [g/l]	Li [g/l]	Ba [mg/l]	Cd [mg/l]	S [mg/l]	Si [mg/l]
1 sample 100*diluted		28		0.50	0.44	**650**	51
1 sample 100^2*diluted	**150**	**30**	**0.3**				
Concentration in mol/l	**3.84**	**1.30**	**0.04**			**0.02**	

The atomic weights of the main elements K, Na, Li, and S are: K: 39.1 g/mol, Na: 23.0 g/mol, Li: 6.94 g/mol and S: 32.1 g/mol. Applying these values leads to the molar concentrations depicted in Table 3.1. Assuming that all detected alkali metals (K, Na and Li) contribute to the concentration of

OH^- ions, this concentration would be around 5.2 mol/l. Assuming this concentration composed of 25% NaOH and 75% KOH would result in a density of 1.206 g/ml. This closely matches the initially determined density of 1.209 g/ml.

3.1.2 Ni - electrode

SEM/EDS and XRD were used to investigate the composition of the Nickel electrode.

EDS shows that not only Nickel is incorporated in the electrode, but that cobalt is present too. The atomic ratio of Nickel to Cobalt is 5/1.

XRD-Tests were performed with the electrode material before activation and with the activated, discharged material. Figure 3.2 depicts the data of the two measurements. (The background has been removed).

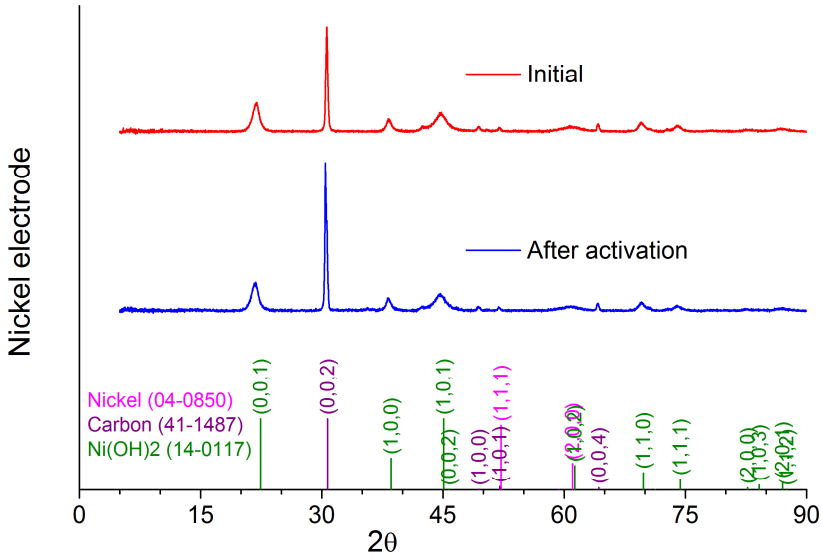

Figure 3.2: XRD-data of new and of activated Nickel electrode in discharged state ($Ni(OH)_2$), wavelength 1.78897, the background is removed. For the sake of clarity, Cobalt and Cobalthydroxide are not added to the data. Their peaks are close to Nickel and Nickelhydroxide, due to their neighboring position in the periodic table. See appendix A for raw data.

The XRD data reveals that the Nickel electrode undergoes no structural change during the activation process. The graph for the material before activation is identical to the graph after activation. Carbon is visible in the XRD data, too.

Carbon is often added to the active material of the electrode to increase the conductivity. Cobalt is often incorporated in the Nickel lattice to reduce the electrode potential and with that to reduce oxygen evolution.

More SEM/EDS data is provided in Appendix A.

3.1.3 Fe - electrode

SEM/EDS and XRD were also used to investigate the composition of the iron electrode.

EDS after activation shows that only iron is president as active material.

XRD-Tests were performed with the electrode material before activation and with the activated, discharged material. Figure 3.2 depicts the data of the two measurements. (The background has been removed).

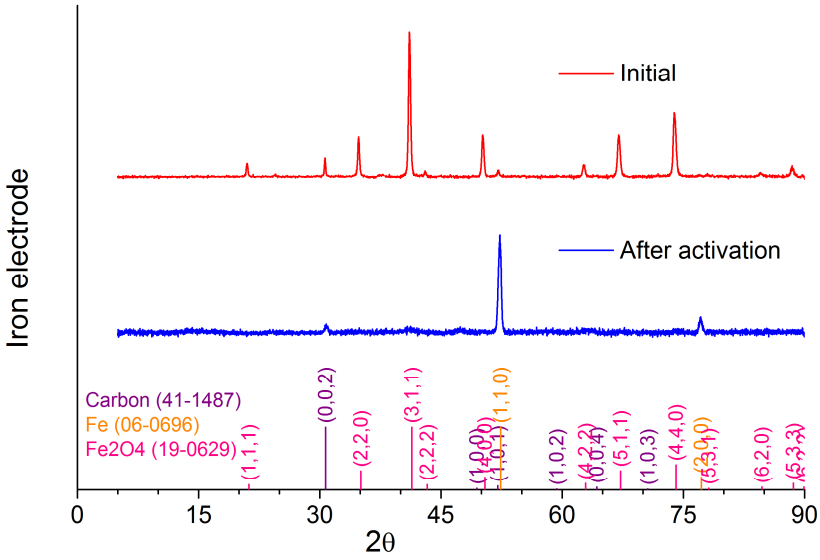

Figure 3.3: XRD-data of new and of activated Iron electrode in the discharged state ($Fe(OH)_2$), wavelength 1.78897, the background was removed. See appendix A for raw data.

The XRD data reveals, that the Iron electrodes undergoes an activation process, iron oxide (Fe_2O_4) is reduced to iron.

More SEM/EDS data is provided in Appendix A.

3.2 Cell design

The cell is built up from individual compartments that are enclosed by windows and supporting frames. The setup is screwed together through the supporting frame. The supporting frame has legs to allow access to underside of the device, and to detect any leakages that might occur. Each individual compartment has three holes drilled in the top and one hole drilled in the underside. The holes in the top allow for simultaneous electrical connection, gas connection, and refill. The hole in the underside allows draining of the device. Alternatively, this hole could serve as inlet for a capillary connection or for additional forced gas bubbling.

The dimensions of the electrode (85mm x 70mm x 4mm) are the starting point for the cell design. The chamber size is specified as 120mm x 80mm x 4mm to accommodate the electrode and the electrolyte reservoir. For practical reasons, the frames surrounding the electrodes have a width of 30mm and a thickness of 6mm, resulting in dimensions 180mm x 140mm x 6mm. Next to the electrode compartment, a double-sided recess (5mm x 1mm each) is milled into the frame to hold and fix the membrane support (130 mm x 90mm x 1mm). An O-ring around the recess seals the compartment. The sealing plane is surrounded by drill holes necessary to screw the individual components with windows and supporting frame together.

The membrane support has a row of three cutouts of 18mm x 65 mm each, to enable electrolyte flow between the compartments with a total open area of 3510 mm². The membrane is cut to 70 mm x 75 mm to cover the cutouts and overlap their edges by 5mm. For stability reasons, three cutouts were created, with 3mm separation, rather than one large cutout.

3.2.1 Material selection

The design requirements for materials are:

- Resistance to KOH and NaOH at all concentrations
- Resistance to temperatures up to 50˚C
- Resistance to H_2 and O_2
- Transparent windows
- Affordable

The following materials were chosen as meeting these requirements:

- Frames: polypropylene (PP)
- Windows: rigid ployvinylchloride (PVC)
- Membrane supports: rigid PVC
- O-rings: ethylene propylene diene monomer (EPDM)

The screws are made from stainless steel, while the supporting frame, which is not in direct contact with the electrolyte, is made from aluminum. Nickel is used for wiring inside the cell, Zirfon® Perl (see chapter 2.3) is used for the diaphragm.

3.2.2 Final layout

The final cell that was used for testing, was built up with two negative and two positive electrodes. Figure 3.4 shows a picture of the assembled cell, and an exploded view of the configuration.

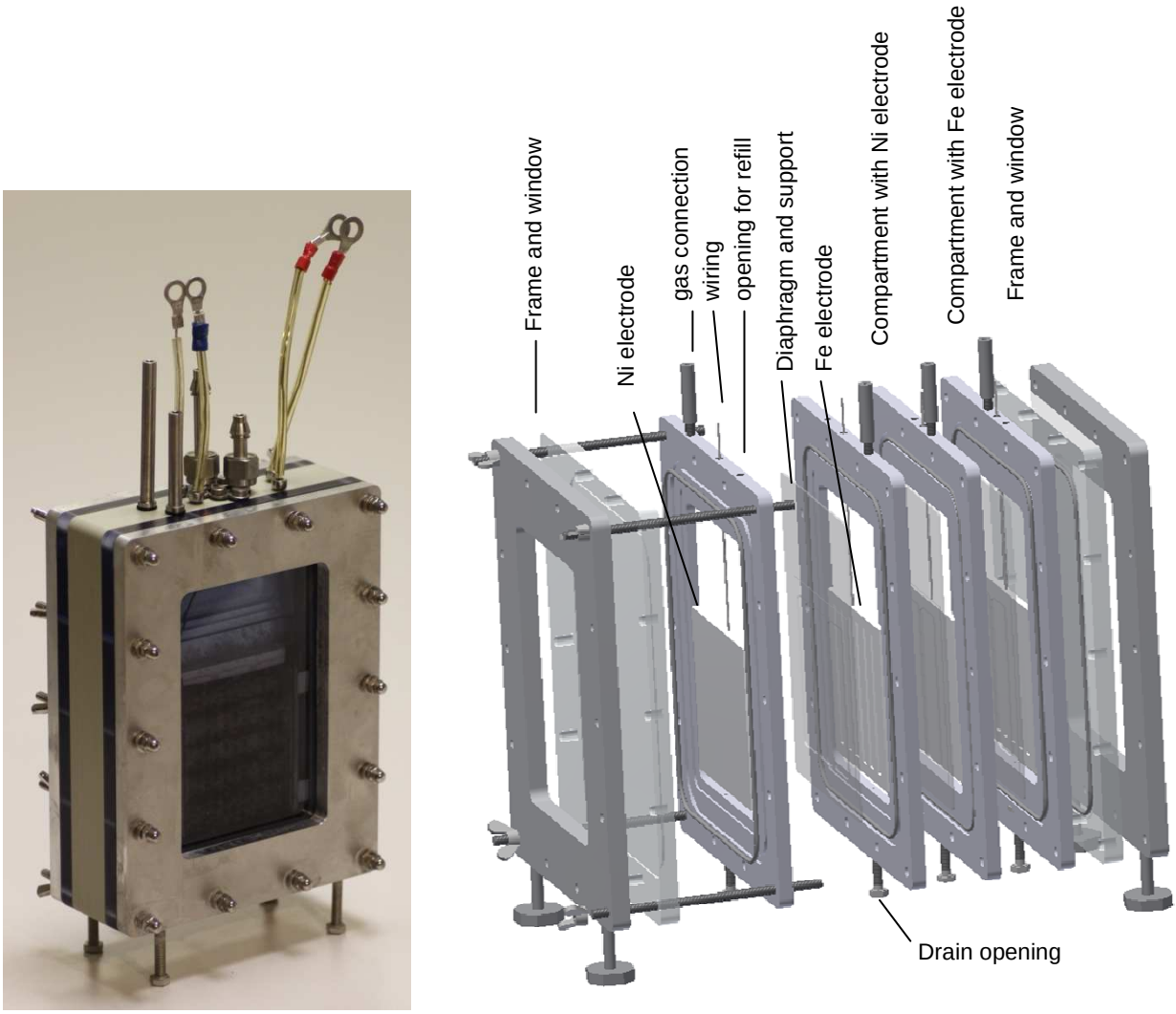

Figure 3.4: The final battolyzer, left: picture; right: exploded view

The nickel wires are welded to the electrodes, as clamping was found to be insufficient to maintain a constant resistance (the contact between electrode and wire got lost). The resistance of the connection point of the wire to the electrode was determined to 27-30mΩ for the individual electrodes. As the assembly consists of two iron and two nickel electrodes in a parallel setup, the total Ohmic resistance is approximately the same value of 27-30mΩ; The added resistances of having two electrode resistances (Ni and Fe) in series is cancelled out by the doubling of the electrodes in parallel.

4 Experimental details

Experiments have been performed for three purposes:

- Examination of durability and flexibility of available Ni-Fe batteries
- Study effects of different electrolyte compositions
- Testing the battolyzer

The durability and flexibility (battery cells C1-C4), and the effects of different electrolyte compositions (battery cells C6-C8) of commercially available Ni-Fe batteries were tested. For this purpose, Ni-Fe batteries (see chapter 2.2.3) with a rated capacity of 10Ah were purchased. While the test-series for durability and flexibility uses the supplier-provided electrolyte (composition see chapter 3.1.1), the test-series concerning electrolyte composition uses electrolytes that we prepared ourselves (see chapter 4.2.1). The battolyzer too operates with an electrolyte that we prepared ourselves.

All cells have mainly been tested by chronopotentiometry (CP). Electrical impedance spectroscopy EIS was only applied to gain further insight into cell characteristics. As mentioned in chapter 2.6, a cycle is counted from full discharge to full discharge. Water consumption, charge energy, discharge energy, and capacity were recorded. The cycle definition that we used has the advantage that water consumption can always be related to the recorded amount of charge insertion and withdrawal as the end state of the battery is the same (SoC=0).

The charge rate and discharge rate of batteries are usually indicated as the (dis)charge rate “C/x”. This means that the full capacity C in [Ah] is (dis)charged in a duration of x hours. All mentioned charge rates are given relative to the nominal capacity of the device used. In our tests, the nominal capacity of the commercially available batteries is 10Ah, and the nominal capacity of the battolyzer is 5Ah.

The instruction and maintenance manual of the purchased batteries [42] suggests standard charging as 8 hour charging at a C/5 rate. For these tests, a standard cycle (SC) is defined as 8 hour charging at a C/5 rate combined with a discharge at a C/10 rate until the cell voltage drops below 1.1V.

The charge retention test (CR-test) is another test that was executed a number of times. The charge retention is investigated by charging the battery to a certain state and then discharging it. Previous experiments revealed that the discharge capacity (C^*) of the commercially bought batteries in an SC is approximately 12Ah (=C^*). The CR-tests were executed with charge-insertions ranging from 0.25C^* (3 Ah) up to 5C^* (60 Ah). The charge insertion was limited to 60Ah as the battery reservoir has a storage limit of 15 ml H_2O, which is the amount of water consumed during such a cycle. Of the 60 Ah charge, approximately 15Ah were utilized for charge retention, and the remaining 45Ah were used for electrolysis. This corresponds to the electrolysis of 15g of H_2O. Charge retention tests were performed at different rates and temperatures.

Most tests were performed using the Maccor for battery testing. The Maccor has various channels and each channel was assigned to a certain cell. In these tests, some cells appeared to perform better than others. To eliminate the possibility of instrument error, different channel/battery configurations were tested. From these tests, we learned that the measured voltages were not battery-, but channel-dependent. The voltages from the Maccor were monitored with a Keithley.

The output from the Keithley indicated that the Maccor device was not calibrated correctly. However, the deviation was constant and only occurred during charging. Table 4.1 shows the measured deviations for each channel. A negative value means, that the displayed voltage as measured by the Maccor is too low. A positive value means that the measured voltage is too high.

Table 4.1: Maccor voltage correction

Channel	1	3	5	7	9	10	11	12
Correction [V]	-0.010	0.008	0.012	-0.020	0.002	0	-0.008	-0.006

All plots and data in this work are corrected with above values. However, raw data on the server is not corrected. All data files from the Maccor have an ending `.00X` for channel 1-9 or `.0XX` for channels above 9, where X and XX represent the channel number.

In November 2015 the Maccor was re-calibrated. Consequently, voltage correction was not necessary anymore. However, because other groups were using the Maccor for their own experiments, only two test channels were available for further testing. As one test channel can handle a voltage of up to 10V, tests with cells C1-C4 were continued with the batteries connected in series on one test channel. The second channel was reserved for tests with the battolyzer. The maximum allowable current for both available channels was 2A. The maximum allowable current for previous tests with cells C1-C4 was 4A as two test channels were combined into one.

4.1 Experiments for durability and flexibity, Cells C1, C2, C3 and C4

This test-series is designed to simulate real-life situations, including full and partial charging and discharging, rapid switching, continuous overcharging, and around-the-clock cycling over a period of months. Rapidly changing charge-discharge cycles are designed to mimic application as a peak-shaving battery and electrolyzer. Such a system would experience a varying renewable electricity input (charge/electrolysis) interspersed with electricity demand at times when the renewable electricity production is less than the electricity consumption. Experiments were performed with four separate cells to verify reproducibility between the cells.

Tests were performed either in a temperature-controlled oven, or in an insulated box in which the temperature development was monitored with thermocouples (see chapter 4.1.5). Tests in the oven were performed at temperatures of 30°C, 35°C, or 40°C.

4.1.1 Cycling experiments

The majority of all tests start with charge insertion, followed by a discharge. Cycling tests, in the form of charge CR-tests, were carried out at different temperatures and at different rates of charge and discharge. The most applied test is the standard cycle, which is executed between varying programs to equilibrate rate and temperature effects.

Rate tests were performed at rates ranging from C/10 to C/2.5 for charging, and from C/10 to C/3.33 for discharging. During each of the test-series, two of the three parameters (Temperature, charge and discharge rate) were kept constant to explore the effect of the third.

4.1.2 Intermittent charge-discharge of the electrodes

In a renewable-energy-based future, we believe that hydrogen will be produced from energy overproduction mainly during summer months. With this idea in mind, the test-series for

intermittent charge-discharge of the electrodes was devised. The expected pattern of use in such a scenario is partial discharge (during excess power consumption) followed, by charge insertion higher than the previous discharge (during excess power production). As a result, the electrodes will reach a steady-state situation at the charged state over successive partial overcharge cycles.

Intermittent charge-discharge programs were executed with different charge and discharge rates as well as different charge and discharge times. The programs were executed in the controlled-temperature setup and in the insulated box setup. The programs were designed to exploit the cell's water reservoir. All programs were completed with a final discharge, so that the water loss could be measured. As stated in the cycle definition, one cycle is counted from final full discharge to final full discharge, therefore all sub cycles included in a program contribute to the overall cycle being tested.

Two aspects are of main interest:

- Will intermittent charge-discharge cycles influence the cell's efficiency?
- Do the cells withstand partial discharge with successive overcharging?

4.1.3 Switching tests

The switching tests are a continuation of intermittent charge-discharge of the electrodes, but then with decreased switching times. Two types of switching tests have been performed: tests with a continuous switching program, and tests with a periodic switching program consisting of different sequences.

Tests with a continuous switching program were executed with steadily decreasing switching times. The shortest switching cycle that was tested consisted of 25 seconds charging at rates of C/2.5 (4 A - maximum possible current with Maccor) followed by 5 seconds discharging at a rate of C/5 (2 A). The average charge rate for this time interval is C/3.33 (3 A). These initial tests did not show any detrimental effects. To further evaluate the effects of periodic switching programs on system performance, programs consisting of different sequences were created.

All sequences have the same average charge rate of C/3.33 (3A), and the same sequence duration of 30 minutes. The first sequence (A), constant current charging at 3A without switching, is added for reference. Sequence A is followed by four sequences (B-E) with decreasing switching time and increasing cycle number. A rest period of 1 minute was applied between the sequences. This combination of sequences was repeated four times during each test. Prior to switching, an initial charge insertion (5 hour, 3A) was applied to activate the electrodes. Tests were performed at 30°C, 35°C and 40°C, Table 4.2 provides detailed sequence characteristics.

Table 4.2: Sequence characteristics to switching tests.

Sequence	Charge	Discharge	#sub-cycles
A	3A	-	-
B	4A / 300 sec	2A / 60sec	5
C	4A / 150 sec	2A / 30sec	10
D	4A / 50sec	2A / 10sec	30
E	4A / 25sec	2A / 5sec	60

Since all sequences imply the same average charge rate of 3A, the average rate of electrolysis is constant throughout all sequences. However, the amount of current that passes the circuit is 22.2% higher during the switching sequences (B-D) compared to the reference sequence A. This fraction is used for electrical energy storage. Sequences B-E provide electrolysis and 10% extra energy storage while sequence A provides only electrolysis.

4.1.4 Electrolysis tests

Electrolysis tests were performed to determine the rate and temperature dependence of the electrolysis potential of the charged electrode. Tests were executed at RT and in the oven at 30°C, 35°C and 40°C. These tests were performed with cells C1, C2, and C3. Between the electrolysis tests SC were performed to equalize effects of overcharging and temperature. Again the water loss was recorded.

The battery is initially charged by charge insertion at 0.35 C for 5 hours, followed by charge insertion at 0.4 C for 1 hour to activate the electrodes. Subsequently the batteries are charged at decreasing rates. Each charge rate is held for one hour. The following rates have been tested: 0.4C, 0.375C, 0.35C, 0.325C, 0.3C, 0.275C, 0.25C, 0.225C, 0.2C, 0.18C, 0.16C, 0.14C, 0.12C, 0.1C, 0.08C, 0.06C, 0.05C, 0.04C, 0.03C, 0.02C, 0.01C, 0.0075C, 0.005C, 0.0025C and 0.001C. (Contrary to the notation used in the introduction of this chapter, the rate is expressed here as 1/x C. This representation allows us to derive the step size quickly and avoids unaesthetic numbers with lots of decimal places.)

The approach with steadily decreasing rates was applied as these test conditions lead to equilibrium potential for the various test rates. A larger rate step size does not lead to equilibrium within the one-hour step time. Increasing the rate was also not an option, as it would not be possible to get to charged electrodes in the first place at these very slow rates tested.

4.1.5 Temperature monitoring

Aside from initial tests under laboratory conditions, testing was performed either in an oven with temperature control, or in an insulated-box with temperature monitoring.

Since the efficiency of the batteries is less than 100%, there should be a net temperature increase. With the insulated-box setup, it is possible to determine when the main heat generation from losses takes place, and if these losses could be reused in efficiency gains.

The thermal insulating box-setup was built up from two polystyrene boxes and polystyrene chips. The outer box has outer dimensions of 390 mm x 290 mm x 370 mm (L x W x H) with a wall-thickness of 50 mm. The inner box has outer dimensions of 225 mm x 160 mm x 190 mm with a thickness of 30 mm. Figure 4.1 shows a schematic drawing of the box- setup.

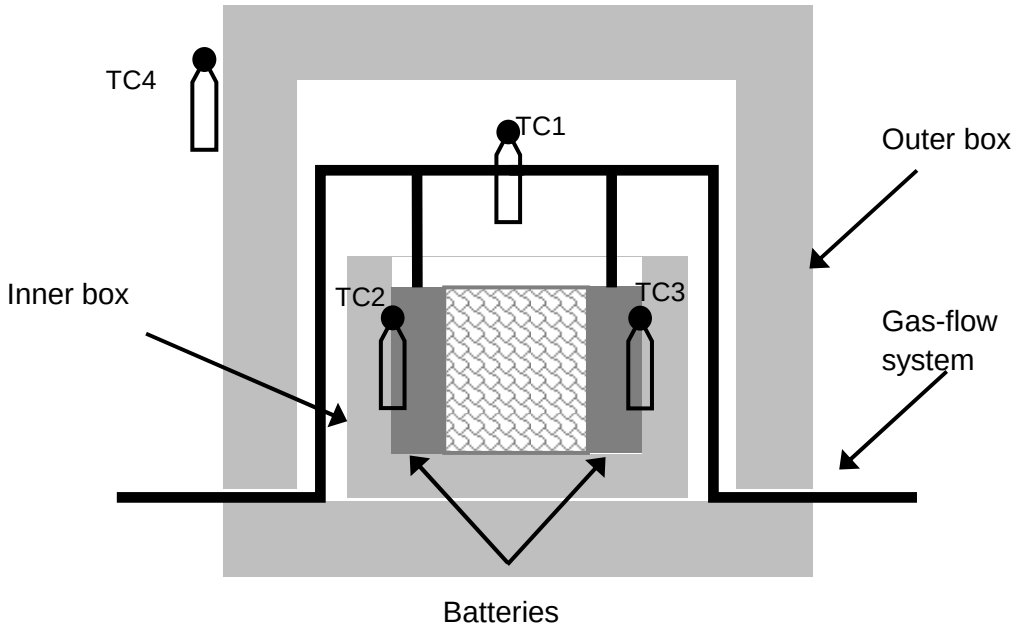

Figure 4.1: Schematic drawing of insulated box-setup

The two test cells were located in the inner box, each next to a side wall. The remaining space between the batteries was filled up with polystyrene chips. The inner box itself stood on the cover of the outer box which was placed upside down. The outer box was used as removable cover.

The box-setup is equipped with 4 thermocouples (TC). The thermocouples measure the temperature of each of the cells, the temperature in the box, and the temperature of the surroundings. The thermocouples that were used to measure the cell temperature were attached to the batteries with thermally conducting tape, located on the face next to the side walls of the inner box. A Swagelok gasflow system was used to purge produced gasses completes the box-setup.

4.1.6 Gas measurements

Complementary to the cycling of the batteries, gas measurements were performed to determine the time frame of gas production and the gas quality. Gas analysis was executed with a mass spectrometer (see chapter 2.7.3). The mass spectrometer was attached to the gas-flow system with a bypass.

The gas flow system was directly connected to the cells (see Figure 4.1), so no gas separation was possible in this case. Therefore, argon was used as purge gas to avoid an explosive gas mixture. In order to prevent the gas mixture from being explosive, the concentration of O_2 or H_2 must remain below 4%. Testing was limited to a charging rate of 3A for each cell, leading to a gas production rate of 6A, equivalent to a production rate of 22.8 ml/min for O_2 and 45.6 ml/min for H_2 (see chapter 2.1.3). A purge flow of Argon of 520 ml/min suffices to avoid an explosive gas composition. Moreover, the purge gas transports the product gasses quickly to the bypass, while spare gas is transported to the exhaust system.

Tests with gas measurements were executed as charge retention tests and as intermittent charge - discharge tests.

4.1.7 Tests in series array configuration

Since November 2015 cells C1 to C4 were arranged in an electrical-series-connected setup. Cycling, charge retention and intermittent charge-discharge tests were performed as described earlier with regulated temperature in the oven.

The available Maccor channel has a current limit of 2A, thus tests were limited to this current. Voltage limits were set to 7V (4x 1.75 V) for charging and 4.7 V for discharging, bearing in mind that the capacities of the 4 cells are not the same. By the time, that the first cell reaches 1.1V, the other cells will have a voltage around 1.2V, therefore the voltage limit was set to 3x1.2 + 1.1 = 4.7V. Handling a lower voltage limit (e.g. 4.4 V = 4 x 1.1V; 1.1V = voltage limit SC) would expose the limiting cell to cell voltages below 1.1V, which might activate the second discharge-plateau.

4.2 Experiments with different electrolytes, Cell C6, C7, C8

As mentioned in chapter 2.5, Ni-Fe batteries and alkaline electrolyzers both operate with potassium hydroxide as electrolyte. Only the concentrations of potassium hydroxide differ between these two applications. The electrolyte of Ni-Fe batteries additionally contains Lithium hydroxide. The objective of this test-series is to find the best electrolyte for the battolyzer. Points of interest are especially:

- Charge retention
- Efficiency
- Electrolysis potential

The charge retention is investigated by charging the battery to various states, with a subsequent discharge. The following states are defined to be tested: 0.25C*, 0.5C*, 0.75C*, 1C*, 1.25C*, 1.5C* and 2C*. These states correspond with the following amounts of charge insertion: 3Ah, 6Ah, 9Ah, 9Ah, 12Ah, 15Ah, 18Ah and 24Ah. To avoid possible effects of rigorous overcharge, charge insertions were limited to 24Ah for these test-series. The efficiency was evaluated as described in chapter 2.6. The electrolysis potential is visible in the voltage plots as final potential of the cycles with 24Ah charge insertion. Charging was performed at charge rates of 2A and discharge at rates of 1A. These cycling experiments were accompanied by EIS experiments.

Starting point for the test-series is an electrolyte with 21wt% KOH, the concentration which is normal for Ni-Fe batteries, but without the addition of LiOH. Three cells - C6, C7 and C8 - were activated and tested with this "standard" electrolyte to obtain reference values for further tests.

In a following test-series, the effect of KOH concentration was evaluated. The electrolyte of the cells was replaced with varying concentrations of KOH, ranging from 50% to 150% of the original concentration. Cell C6 was tested with a concentration of 11wt% KOH (-50%), cell C7 with 21wt% KOH (=initial concentration) and C8 with 30wt% KOH (+50%).

In two subsequent tests, the effect of LiOH was investigated while keeping the KOH concentrations from the previous test-series unchanged. In a first step, 20 g/l $LiOH.H_2O$ was added to the electrolytes, in the second step another 20g/l resulting in a total addition of 40g/l $LiOH.H_2O$.

4.2.1 Preparation of electrolyte

Demineralised water from a Merck Milli-Q Plus 185 water purification system was used for the preparation of the electrolytes. Furthermore, potassium hydroxide flakes 85% from Alfa Aesar

(remaining 15% H_2O) and Lithium hydroxide monohydrate ($LiOH.H_2O$) from Sigma with a purity ≥ 99.0% have been employed.

Mixing guidelines [42, 43] define a weight ratio of alkali:water of 1:3 and a guiding value of 1.20 +/- 0.01g/cm³ for the density of the electrolyte. A KOH concentration of 1:3 (25wt%) corresponds to a density of 1.23 g/cm³ [50], which leads to a contradiction in specifications. However, considering that KOH flakes have a purity of 85% (the rest is H_2O), results in a ratio of alkali:water of 0.85:3.15 (=21.25 wt% KOH), which is in accordance with a density of 1.20 g/cm³ at 15˚C. This ratio is the starting point for preparing the electrolyte. This mixing ratio leads to a density of 1.196 g/cm³ and molarity of 4.53 M at 25˚C. The densities of the self-made mixtures have been verified. The concentration of the electrolyte was varied with respect to the molarity of 4.53M. Molarity and density are related via the following equation were 5.611 originates from the molar weight of KOH (56.11 g/mol) [2]:

$$Molarity = \frac{density * wt\% \, KOH}{5.611} \tag{45}$$

The information about the electrolyte mixes is summarized in Table 4.3.

Table 4.3: Electrolyte mixing

	Initial electrolyte	reduced concentration (- 50%)	reference	Increased concentration (+50%)
wt%	21.25	11.53	21.25	29.73
Molarity	4.53	2.265	4.53	6.795
density at 25˚C	1.196	1.102	1.196	1.283
Cell	C6,C7,C8	C6	C7	C8

Around 100ml of electrolyte has been prepared in the appropriate concentration for each cell. Part of this volume was used to fill the cell (~70ml). The remainder was stored. At the end of each test-series, the electrolyte was removed from the cell, and added to the remainder.

After the test-series with pure KOH solution, 2g of $LiOH.H_2O$ was added to each solution (corresponding to 20 g/l of LiOH). The solution was then mixed until the LiOH had fully dissolved. The test cells were filled with the new electrolyte for the next series of experiments.

After the first series of experiments with 20 g/l of LiOH, this procedure was repeated, to bring the LiOH concentration to 40 g/l.

The molar weight of $LiOH.H_2O$ is 41.96 g/mol, hence the content of Li and OH ions increases with 0.48 mol/l with each addition. After finalizing the last cycles the electrolyte was replaced with the initial electrolyte, which has been stored until then.

4.2.2 Cycling experiments and history

All cells performed 189 cycles with almost identical programs. The tests took place in the laboratory, at room temperature.

After activation, the first series of charge retention tests was carried out with the "standard" electrolyte. After 28 cycles, the electrolyte of each cell was replaced. Before and after each charge

retention test-series, and before and after each electrolyte replacement, a series of SC was scheduled to stabilize the cell with the new electrolyte concentration.

In the first test-series, the batteries operated with pure KOH electrolyte, at the same concentration, in the second series at varying concentrations.

The next CR-test-series, with 20 g/l of $LiOH.H_2O$, started after cycle 74 for cells C6 and C7, and after cycle 77 for cell C8.

The test-series with 40 g/l of LiOH.H2O started after cycle 156, for each of the cells.

Again, after a series of SCs, charge retention tests and SCs, the electrolyte was replaced with the initial solution. For the last 7 SCs (182-189) the cells operated with the initial electrolyte.

As mentioned earlier, during experimentation, differences in the recorded voltages between the Maccor and the Keithley systems were identified, see Table 4.1.

To investigate suspected measurements errors, the channel/battery configuration was changed. Cell C6 had been connected to channel 10, C7 to channel 11 and C8 to channel 12. For investigation of a possible error, the cells' connection was changed two times. After the first change, C6 was on Channel 11, C7 on Channel 12, and C8 on Channel 10. After the second change, C6 was on Channel 12, C7 on channel 10, and C8 on channel 11. In each case 8 SCs were performed, corresponding to cycles 140-147 and cycles 148-155 respectively.

4.3 Experiments with the battolyzer

After the first month of successfully testing the commercial batteries it was apparent that they were robust and could withstand great abuse, such as overcharging of multiple times their nominal capacity. This made their electrodes suitable for the battolyzer. Tests with the battolyzer were performed to demonstrate that this concept works. The following features were investigated experimentally:

- Cycling capabilities
- Resistance of the battolyzer with and without membrane
- Quantitative and qualitative gas characterization
- Electrode potentials relative to a reference electrode.

The first test with the battolyzer was started on the 19th of August 2015, the device has been operational ever since. The first test results showed instable voltage curves for performed cycling experiments. I found out that the clamped contacts between the nickel wire and the electrodes were poor. To improve the contacts, the nickel wires were welded to the electrodes. After this change reproducible results were obtained. Once the contacts were fixed, the testing started.

The construction of the battolyzer is described in chapter 3.2. As the test-series with different electrolytes were still underway, conventional electrolyte, composed of 21.25 wt% KOH and 20 g/l $LiOH.H_2O$ was used for the battolyzer. The total molarity of the electrolyte was 4.53 + 0.48 = 5.01M (see chapter 4.2.1), leading to a pH value of 14.7. At this concentration, the equilibrium potentials for the electrodes are: -0.932V for the iron electrode and 0.449 V for the nickel electrode. All tests were performed at room temperature.

4.3.1 Cycling capabilities

The battolyzer is constructed with half of the capacity of the normal battery, so that the nominal capacity for the battolyzer would be 5Ah. Standard cycles were performed with the same C/5 charge rate and C/10 discharge rate that were used for the conventional Ni/Fe batteries.

4.3.2 Tests with and without membrane

The membrane is an essential part of the battolyzer as it separates the hydrogen and oxygen that are produced. Because of this, it is interesting to study the effects of the membrane. Tests with and without membrane were performed to determine the effects on the cell performance. As CP-tests hardly showed any deviations in cell voltage between cases with and without membrane, supplementary EIS tests were carried out.

4.3.3 Tests for gas characterization

Contrary to the experiments performed with battery cells C1 to C4 (see chapter 4.1.6), the setup of the battolyzer allows for measurements of the gasses produced at the individual electrodes. Argon was used again as a purge flow to transport the product gasses to the mass spectrometer.

To test the hydrogen and oxygen quality, their respective compartments were merged and then connected to a bubbler filled with water to equilibrate the pressure throughout the device. Experience shows that the device is sensitive to differential pressure. This design issue can certainly be improved for battolyzer V2.0. Prior to testing, the electrodes were charged. Tests were performed at the charged electrode at the rates of, 0.5A, 1A, 1.5A and 2A. Short intermittent discharge steps at 0.5A and rest steps were also part of the program.

Trace gas measurements were performed to analyze the gas quality. Special attention was paid to gasses containing carbon, as carbon is incorporated in the electrodes as conductive additive. Traces of carbon could indicate the electrode´s destruction. For this reason, particle masses 12, 14, 15, 16, 17, 28 and 44 were added to the initial compilation consisting of masses 2, 18, 32 and 40. In addition, the relative sensitivity of all masses was set to 1. Actually the mass spectrometer does not measure the mass, but the mass/charge ratio, Table 4.4 provides a guideline for interpretation of the results.

Table 4.4: Peaks (mass/charge ratio) for common gasses in [%]

Gas	2	12	14	15	16	17	18	28	32	34	44
H_2	100										
O_2					9				100	0.4	
H_2O					2	21	100				
N_2			5					100			
CH_4			16	85	100						
CO		5			2			100			
CO_2			6		9						100

In addition to analyzing the composition of the individual gas streams, the gas production rate was determined by measuring the volume of produced gas by the charged electrodes over time. A

Fortuna 100 ml gas syringe with a 3-way valve was used for volumetric measurements. A stop watch was used for time measurements. The gas production rate was determined for charging rates of 1A, 1.5A and 2A. The setup was filmed to enable accurate evaluation of the rates.

The theoretical gas production rates for charge insertion of 1A, as well as the ideal gas law, are presented in chapter 2.1.3. During testing, the lab temperature was 20.8˚C and the air pressure was 102400 Pa. Tests were executed in two setups to avoid friction effects: one test where the plunger moved upwards with the evolution of gas (configuration "up"); one where the plunger moved downward with the evolution of gas (configuration "down").

The weight of the plunger causes a differential pressure of +/- 1290 Pa which needs to be taken into account. Moreover, gas syringes are not perfectly gas-tight, so gas loss factors for both setups were also determined. Interestingly, the loss-factor for the configuration "up" (1ml/2.25min) is more than two times higher than the loss factor for the configuration "down" (1ml/5min). Because of the overpressure in the configuration "up" gasses (hydrogen and oxygen) only escape from the syringe whereas in the configuration "down" gasses have to get into the gas syringe due to lower pressure. The gas composition of the gasses leaving/entering the syringe can cause the difference in loss factor.

The measurements show perfect reproducibility for each combination of setup and charge rate.For this reason, only two test runs per test combination were performed.

4.3.4 Tests with reference electrode

Towards the end of the project, the idea arose to determine the specific electrode potentials by means of a reference electrode, to complement the performed work.

First, tests using the reference electrode in combination with the battolyzer were not very encouraging. The reference electrode was connected via a capillary PTFE tube to the bottom hole of the battolyzer. Unfortunately this connection was not very stable, which led to random measurement results. Flushing the capillary led to ionic contact, however this lasted only for about 10 minutes. The obtained results reflect literature results, but they are not of sufficient quality to be presented in this thesis. A simple three electrode setup could serve to obtain meaningful data for future work. To be fair, it is not strictly necessary to perform these tests with the battolyzer.

For the sake of completeness, and to facilitate future work, general technical data for the work with reference electrodes is presented here. A mercury/mercury oxide (Hg/HgO) reference electrode is best suited for alkaline environment. The electrode is filled with a 1M KOH solution. The specifications define the reference potential for this filling solution as approximately -129mV with respect to a saturated calomel electrode (SCE; 0.241 V relative to a standard hydrogen electrode (SHE)). Thus the reference potential is 0.112 V relative to SHE. The reference potential is independent of the concentration of the test-electrolyte.

5 Results

Chapter 5 provides an overview of the obtained results. Experiments have been performed for three purposes:

- Examination of durability and flexibility of available Ni-Fe batteries
- Study effects of different electrolyte compositions
- Testing the battolyzer

The results are introduced in the order mentioned above, with little discussion. Pursuing discussion is presented in Chapter 6.

5.1 Durability and switchability

Tests of durability and switchability were performed with four commercially available Ni-Fe batteries, cells C1-C4. For the description of these tests, see chapter 4.

5.1.1 Charge retention and efficiency

Charge retention (CR) and efficiency were studied by varying three parameters: temperature, charge rate, and discharge rate. Figure 5.1 depicts the discharge capacity and efficiency, plotted against charge insertion for various temperatures. A charge rate of 3A and a discharge rate of 1A were used.

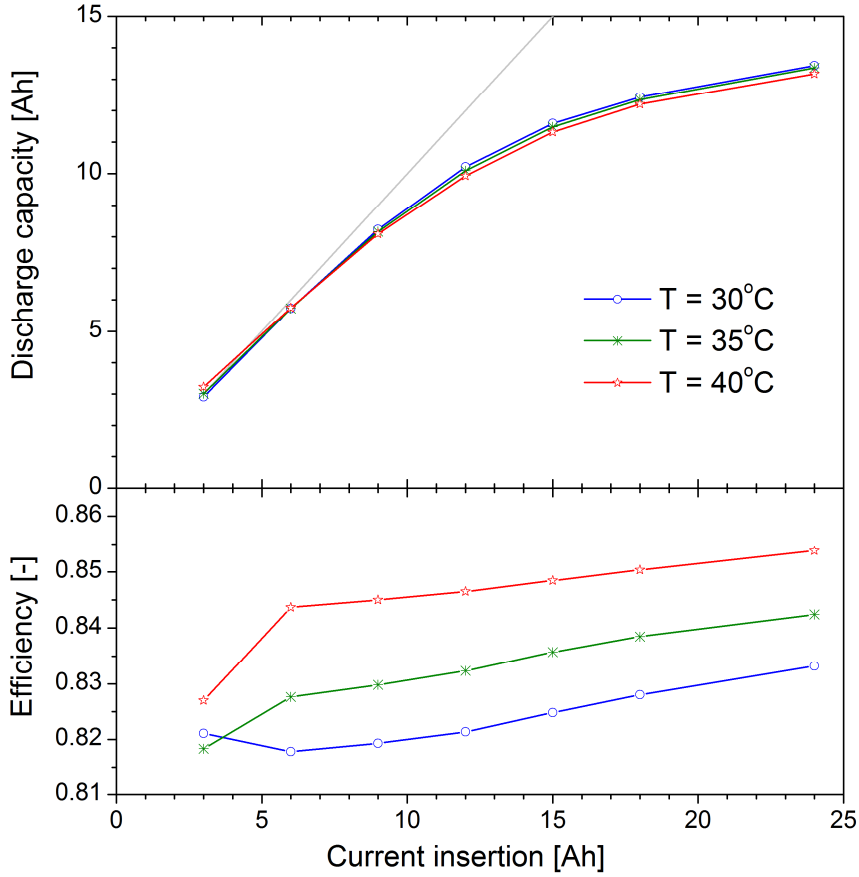

Figure 5.1: Charge retention (CR) and efficiency for a CR test performed with a charge rate of 3A and a discharge rate of 1A (cell C1).

In general it can be observed that the discharge capacity increases with increased charge insertion. Also the efficiency increases. The top figure shows that tests at 30˚C and 35˚C yield the same discharge capacity while tests at 40˚C yield less discharge capacity, and that the difference in discharge capacity is increasing with increasing charge insertion. The cycle-efficiency presented in the bottom figure clearly distinguishes temperature effects. Increasing the temperature with 5˚C leads to an increase in efficiency of about 1%, independent of the charge insertion. Only the first cycle of each series with 3Ah charge insertion shows deviations from these trends. This first cycle is used to equilibrate effects of the previous cycle, which explains these deviations. For example, the discharge capacity at 35˚C and 40˚C is above 100% leading to "negative" hydrogen production and therefore reduced efficiencies according to the applied efficiency definition (see chapter 2.6).

The same effect applies to the efficiencies presented in Figure 5.2, a comparable plot to the last figure, but then performed with varying charge rates while temperature (35˚C) and discharge rate (1A) are kept constant.

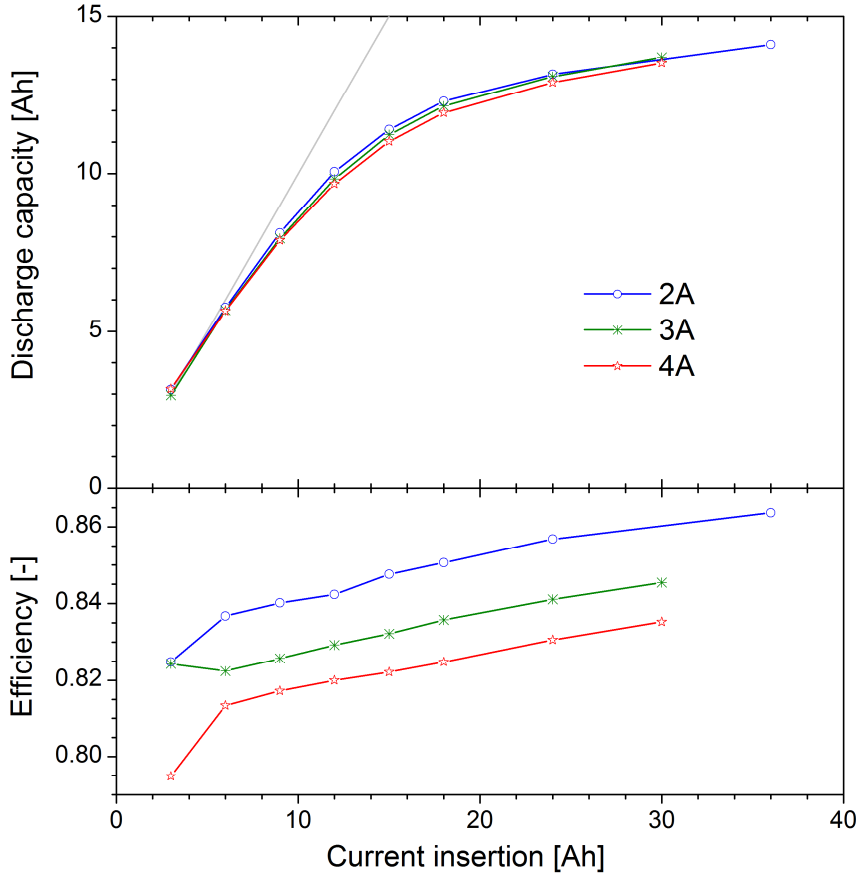

Figure 5.2: Charge retention and efficiency for a CR test performed at 35˚C and with a discharge rate of 1A (cell C2).

The top figure displays the discharge capacity versus charge insertion and shows that the charge retention is highest for low charge rates and lowest for high charge rates. Likewise, the efficiency depends on the charge rate and charge insertion, and again increased charge insertion leads to higher efficiencies. Lower charge rates also lead to higher efficiencies. The difference in efficiency between charge rate 2A and 3A is approximately 1.5% and the difference between 3A and 4A 1%, both almost independent of the charge insertion.

Overpotentials increase with increasing charge rate, which causes the efficiency to decrease with increasing charge rate. Steady increase in hydrogen and oxygen production with increased charge insertion leads to a subsequent increase of efficiency since the voltage associated with electrolysis is the thermo-neutral potential of 1.48V while the average potential for the discharge process is around 1.28V.

Figure 5.3 depicts typical discharge curves for different discharge rates and temperatures. All cycles were charged at the same rate (4A) and charge insertion (24Ah) prior to discharge, first at a rate of 1A, then at 2A and finally at 3A.

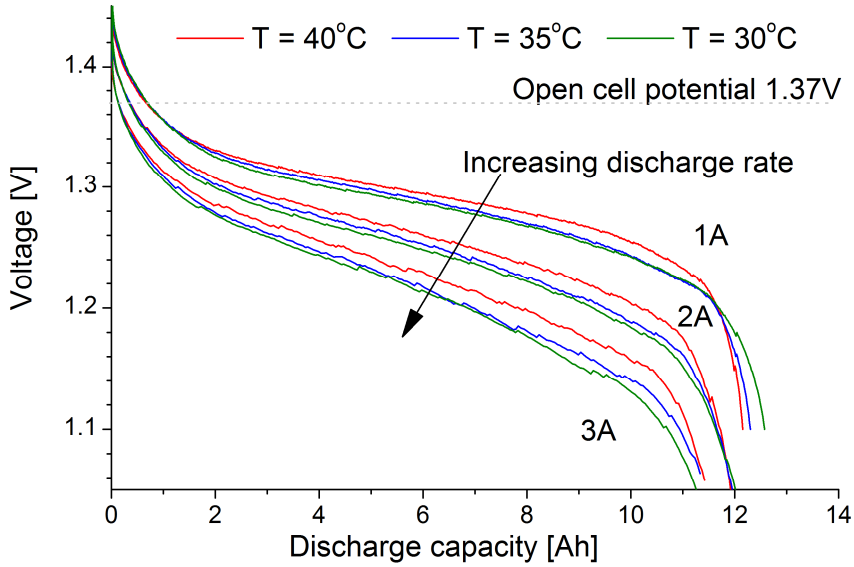

Figure 5.3: Rate and temperature effects on discharge characteristics

The above figure shows that the discharge voltage decreases with increasing discharge rate and increases with increasing temperature. The voltage curves are grouped together according to the three test discharge rates 1A on the top, 2A in the middle, and 3A at the bottom, each with the measurement at 40˚C on the top. The spacing between the measurement at 40˚C and the other measurements is significantly larger than the spacing between the voltage curves for 30˚C and 35˚C, which are close together. However, towards to the end of the discharge, the voltage at high temperatures decreases faster than at low temperatures. Furthermore, the discharge capacity decreases with increasing temperature and charge rate.

Discharge potentials that increase with temperature can be attributed to increasing electrolyte conductivity. The reduced discharge capacity at higher temperatures indicates higher electrolysis and self-discharge at higher temperatures.

Table 5.1 depicts the determined discharge capacity and the calculated average discharge voltage as a measure for the efficiency of the discharge process.

Table 5.1: Discharge capacity (Ah) and average discharge voltage (V) in dependence of discharge rate and temperature

Discharge rate	30 [°C]	35 [°C]	40 [°C]
1A	12.58Ah / 1.281V	12.30Ah / 1.285V	12.15Ah / 1.292V
2A	12.01Ah / 1.243V	11.95Ah / 1.248V	11.92Ah / 1.257V
3A	11.26Ah / 1.216V	11.38Ah / 1.219V	11.44Ah / 1.230V
cycles	94-96	82-84	77-79
weight loss ratio	100.5	96.8	96.1

The highest discharge capacity of 12.58Ah is obtained at low rate and low temperature whereas the highest discharge efficiency of 94.3% (1.292V / 1.37V = OCP) is given at low rate and high temperature. Clearly the effect of discharge rate dominates over temperature effects. Tests at lower rates are even more efficient.

Discharge at 1A was continued until 1.1V whereas discharge at higher rates was extended further until 1.05V. This was done in view of the observed larger overpotentials during higher rates. Either the batteries or the current control of the Maccor have problems handling high discharge rates (3A), as the current control got lost at the end of the discharge cycles at tests at 35˚C and 40˚C (see also Figure 5.3, the discharge curves for 3A do not proceed to 1.05V). The discharge rate of 3A or 0.3C should further be considered as an upper limit of discharge rate as tests at higher rates failed due to lost current control. One of the four test cells was not able to handle a discharge current of 2.75A, but tests at 2.5A were successful. Based on the literature [3], Ni-Fe batteries should be capable of handling a C/1 discharge rate, therefore, it is probably the current control of the Maccor that causes the instability.

Figure 5.4 shows a charge insertion of 60Ah or 6 times the nominal battery capacity for different charge rates at a temperature of 30˚C. The stable battery operation can be recognized from the voltage diagrams since the electrolysis potentials remain constant after the initial charging process.

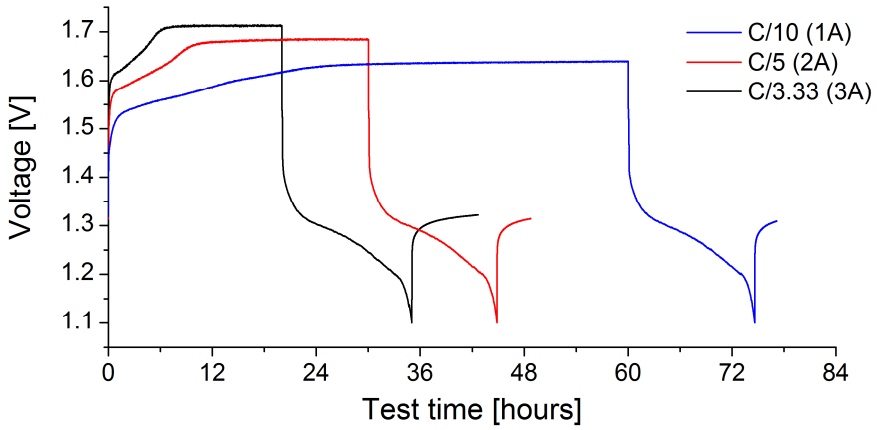

Figure 5.4: Voltage curve for a charge insertion of 60Ah (or 6 times the nominal battery capacity) for different charge rates at a test temperature of 30˚C (cell C2).

Table 5.2 provides the recorded data to the cycles shown in Figure 5.4. The measured electrolysis potentials for charging rates of 1A, 2A, and 3A are 1.631V, 1.676 V and 1.704 V respectively. These values are consistent with the electrolysis potentials of 1.627V, 1.680, and 1.710V determined through electrolysis tests presented in chapter 5.1.4Electrolysis potential. Cycle 81 was the last electrolysis test cycle while the first cycle of the long charging test was cycle number 213. In between these cycles, 3035Ah of charge - more than 300 times the nominal battery capacity - were inserted to the battery. Of this amount of charge, 1684Ah were regained through discharge, and 1351Ah were used for electrolysis of water. The variation of only about +/- 4mV between these electrolysis potentials at different currents after such large amount of charge insertions and battery cycling illustrates the stability and reproducibility of the performance of the electrodes.

Table 5.2: Cycle performance characteristics to Figure 5.4.

		Charging		Discharging		Electrolysis
cycle	Charge rate	Inserted Charge [Ah]	Energy [Wh]	Capacity [Ah]	Energy [Wh]	Capacity [Ah]
213	C/5	60.00	99.19	14.77	18.75	45.23
237	C/10	60.00	96.41	14.53	18.44	45.47
238	C/3.33	60.00	101.05	14.94	18.94	45.06

cycle	$\eta_{battery}$ [-]	$\eta_{electrolysis}$ [-]	$\eta_{overall}$ [-]	Monitored weight loss [g]	Weight loss electrolysis [g]	Weight loss ratio [-]
213	0.189	0.675	0.864	15.81	15.20	0.962
237	0.191	0.698	0.889	15.37	15.28	0.994
238	0.187	0.660	0.847	15.83	15.14	0.957

The highest efficiency of 88.9 % and water loss ratio 99.4% is achieved at low charge rates. Both efficiency and water loss ratio decrease with increasing charge rates. Interestingly, the charge retention of 14.94Ah was highest at a charging rate of 3A, and decreased to 14.77Ah and 14.53Ah for lower charging rates of 2A and 1A respectively. A trend not recognizable from Figure 5.2, were the highest charge retention is observed at low charge rates. A reference test with another cell shows the same results.

Figure 5.5 provides the charge retention for battery C2 for a charge insertion up to 6 times the nominal battery capacity, all cycles are performed at 30˚C with a C/3.33 charge rates and a C/10 discharge rates C/10.

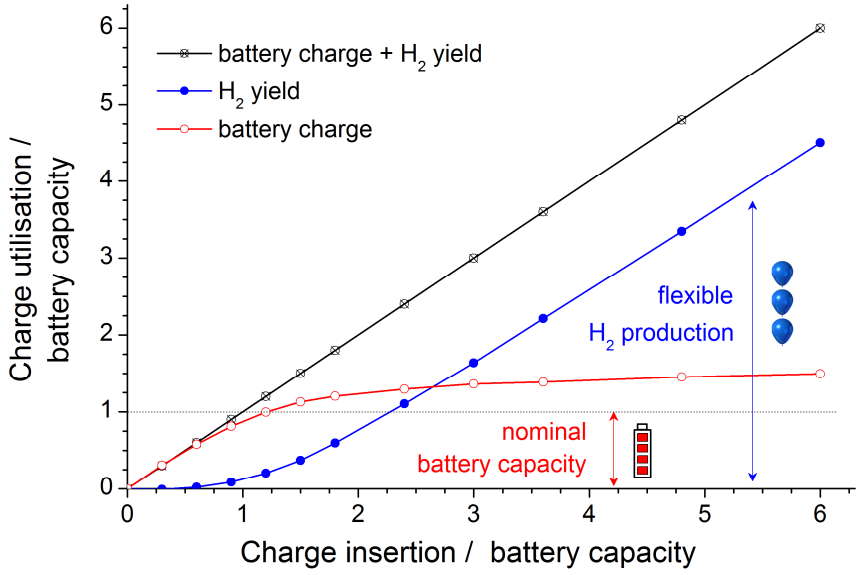

Figure 5.5: Utilization of charge in the battery and the H2 production divided by the nominal battery discharge capacity of 10Ah (cell C2 cycles 236, 238, 247-255, performed at 30˚C, charge rate C/3.33, discharge rate C/10).

Upon charge insertion of 0.5 times the battery capacity, nearly all charge inserted contributes to battery charging. About 1.2 times the nominal capacity needs to be added to retrieve this discharge capacity. At a charge insertion of 2.7 times the nominal capacity, the H_2 production is equal to the retrieved discharge capacity. The discharge capacity increases with increasing charge insertion, up to 1.5 times the nominal capacity for a charge insertion of 6 times the battery capacity. At this stage three times more H_2 is produced than charge is retrieved via discharge. The increase in discharge capacity between a charge insertion of 4.8 times and 6 times the battery capacity is 4% of the nominal capacity. This means that about 97% of charge inserted between these points is used for H_2 production, whereas 3% is used to increase discharge capacity. This illustrates that more electrode material becomes active upon extended charge insertion.

5.1.2 Intermittent charge-discharge of the electrodes

It is most likely, that intermittent charge-discharge of the electrodes will form the main operation modus for the battolyzer. Therefore, extensive tests have been performed for highly intermittent charge/discharge/overcharge conditions. Figure 5.6 depicts a voltage curve for a test-series executed at temperatures of 30˚C, 35˚C and 40˚C, carried out with the 4 cell array configuration. The displayed voltage is the average cell voltage to enable comparison with other results.

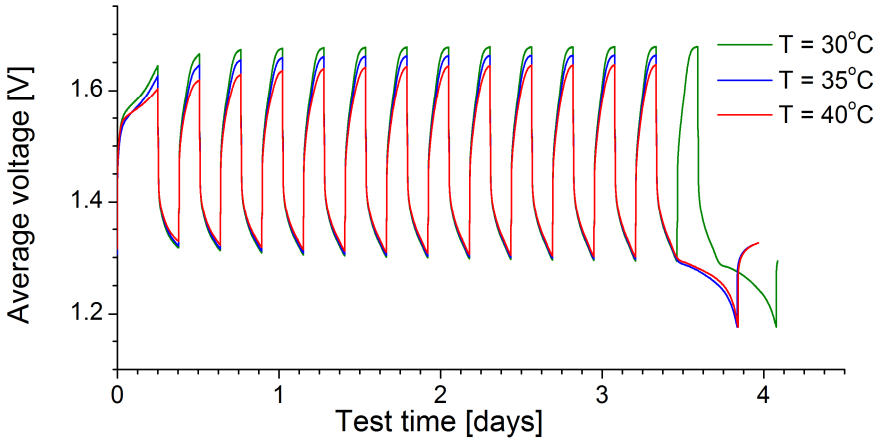

Figure 5.6: Voltage curve for intermittent charge-discharge cycles, cycle number 76 (T=30˚C), 77(T=35˚C) and 81 (T=40˚C). 4 cell array configuration; Initial 6h, 2A charge insertion followed by intermittent 3h 1A discharge and 3h 2A charge; completed by final discharge.

The voltage curves in Figure 5.6 show a stable and reproducible performance of the batteries at all assigned temperatures. It is recognizable that temperature influences the charge process more than the discharge process since the voltage curves are easy to distinguish with increasing voltage (charging process). Yet, the curves are hardly distinguishable while the voltage is decreasing. This observation indicates a temperature dependence of overpotentials related to charging and electrolysis, while overpotentials for discharging are less temperature dependent. Table 5.3 and Table 5.4 depict performance characteristics belonging to Figure 5.6 for the complete cycle and the last sub-cycle (consisting of a 3Ah discharge and a 6Ah charge insertion).

Table 5.3: Cycle performance characteristics to Figure 5.6

Cycle / temperature	Charging			Discharging			$\eta_{overall}$ [-]
	Capacity [Ah]	Energy [Wh]	Average cell voltage [V]	Capacity [Ah]	Energy [Wh]	Average cell voltage [V]	
76 / 30˚C	90.00	580.79	1.613	50.57	268.85	1.329	0.865
77 / 35˚C	84.00	536.69	1.597	47.94	255.29	1.331	0.873
81 / 40˚C	84.00	531.99	1.583	48.07	256.65	1.335	0.882

The overall efficiencies presented in Table 5.3 reveal that intermittent charge-discharge is highly efficient, between 86.5% and 88.2%. Cycles with a comparable discharge to charge capacity ratio of 56% executed with the same rates and temperatures also exhibit high efficiencies (see Table 5.5), but about 1.5% lower compared to intermittent charge-discharge cycles. Analyzing the last sub-cycles of the programs (see Table 5.4) indicates that these sub-cycles are even more efficient since the sub-cycle efficiency is 0.8% above the cycle efficiency. The charge utilization during the sub-cycles is 50% electrolysis and 50% discharge.

Table 5.4: Last sub-cycle (3Ah discharge + 6Ah charge) performance characteristics to Figure 5.6

Cycle / temperature	Charging			Discharging			$\eta_{sub\text{-}cycle}$ [-]
	Capacity [Ah]	Energy [Wh]	Average cell voltage [V]	Capacity [Ah]	Energy [Wh]	Average cell voltage [V]	
76 / 30˚C	6.00	38.83	1.618	3.00	16.10	1.342	0.872
77 / 35˚C	6.00	38.46	1.603	3.00	16.14	1.345	0.881
81 / 40˚C	6.00	38.12	1.588	3.00	16.17	1.347	0.890

Table 5.5: Cycles with a ratio discharge capacity/charge capacity of about 56% comparable to cycles plotted in Figure 5.6. (performed with cell C1)

Cycle / temperature	Charging			Discharging			$\eta_{sub\text{-}cycle}$ [-]
	Capacity [Ah]	Energy [Wh]	Average cell voltage [V]	Capacity [Ah]	Energy [Wh]	Average cell voltage [V]	
163 / 30˚C	24.00	38.47	1.613	13.45	17.31	1.287	0.851
151 / 35˚C	24.00	38.25	1.604	13.26	17.14	1.293	0.858
146 / 40˚C	24.00	37.95	1.591	13.09	17.01	1.299	0.868

A look at the average cell voltages reveals that the gains made result mainly from an increase in the average discharge voltage. Cycles with one charge insertion followed by a final discharge (see Table 5.5) have average discharge voltages between 1.287V and 1.299V. Cycles with intermittent charge-discharge of the electrodes have average discharge voltages between 1.329V and 1.335V. The individual sub-cycles have even higher average discharge voltages. Avoiding less efficient full discharge is thus beneficial.

Next to temperature variation, intermittent charge-discharge of the electrodes was executed with various charge/discharge rates and times. Figure 5.7 depicts a selection of such cycles, the associated cycle and sub-cycle performance characteristics are presented in Table 5.6 and Table 5.7.

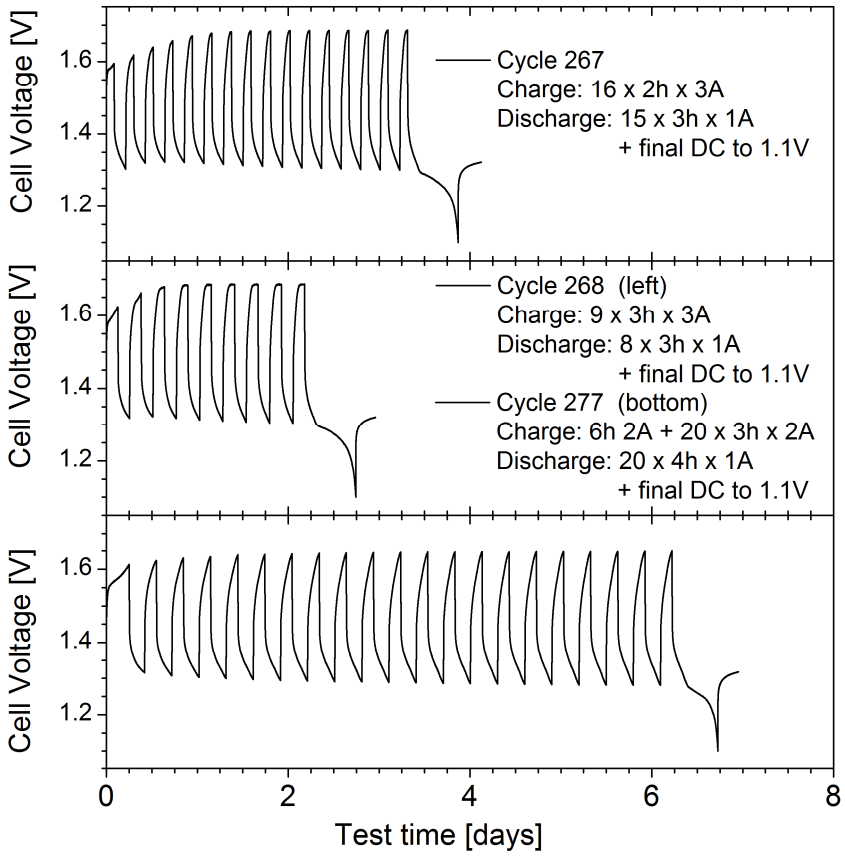

Figure 5.7: Voltage curve for intermittent charge-discharge cycles, all performed at 35˚C, detailed program see inserts; Top: cycle 267, Middle: cycle 268; Bottom: cycle 277 (all performed with cell C2)

Cycle 267, 268 and 277 present cycles comparable to those depicted in Figure 5.6, all performed at 35˚C. In case of cycle 267 the charge rate is increased while the amount of charge inserted is kept constant. This leads to a shorter charging time. In case of cycle 268, the charge rate is increased and the charging time is kept constant. This leads to increased electrolysis with a charge utilization of 2/3 electrolysis to 1/3 discharge. In the case of cycle 277, the discharge time is increased to 4 hours while the other parameters are kept constant. The charge utilization in this case is 1/3 electrolysis and 2/3 discharge.

Table 5.6: Cycle performance characteristics to Figure 5.7

Cycle / temperature	Charging			Discharging			$\eta_{overall}$ [-]
	Capacity [Ah]	Energy [Wh]	Average cell voltage [V]	Capacity [Ah]	Energy [Wh]	Average cell voltage [V]	
267 / 35˚C	96.00	155.38	1.619	58.27	77.71	1.334	0.859
268 / 35˚C	81.00	132.79	1.639	37.41	49.56	1.325	0.859
277 / 35˚C	132.00	207.96	1.575	92.01	122.41	1.330	0.873

Table 5.7: Last sub-cycle performance characteristics to Figure 5.7

Cycle / temperature	Charging			Discharging			$\eta_{sub\text{-}cycle}$ [-]
	Capacity [Ah]	Energy [Wh]	Average cell voltage [V]	Capacity [Ah]	Energy [Wh]	Average cell voltage [V]	
267 / 35˚C	6.00	9.76	1.627	3.00	4.04	1.348	0.869
268 / 35˚C	9.00	14.84	1.649	3.00	4.05	1.349	0.871
277 / 35˚C	6.00	9.45	1.575	4.00	5.34	1.336	0.878

The overall efficiencies in Table 5.6 show values of 85.9% to 87.3% indicating that all these cycles are highly efficient. Again the sub-cycle efficiencies presented in Table 5.7 are even higher.

Comparing the average charging voltage of 1.627V (last sub-cycle 267, Table 5.7) to 1.603V (last sub-cycle 77, Table 5.5) leads to the conclusion that increasing the charging rate while keeping the charge insertion constant leads to an increase in average charging voltage. Increasing both, charging rate and charge insertion results in an increase of average cell voltage to 1.649C (last sub-cycle 268, Table 5.7). The average sub-cycle discharge voltage increases in both cases, 1.348V cycle 267 respectively 1.349V cycle 268 only marginally compared to 1.345V cycle 77. The resulting sub-cycle efficiencies are with 86.9% and 87.1% approximately 1% lower than the efficiency of 88.1% for the reference case. Increasing the discharge time (cycle 277) causes a decrease in both, average cell voltage during charging (1.575V) and discharging (1.336). The sub-cycle efficiency is calculated to 87.8 %, which is close to our reference value (88.1%).

All voltage curves presented in Figure 5.6 and Figure 5.7 show a significant kink during the final discharge step at the discharge capacity were sub-sequent intermittent discharge was stopped. The question rises, is the edge formation of intermittent charge-discharge of the electrodes an enduring effect?

Figure 5.8 depicts a series of standard cycles (269-276) directly performed after intermittent charge-discharge tests. No sign of edge formation or deviation of proceeding discharge cycles is recognizable. No other test following intermittent charge-discharge shows signs of edge formation or deviant behavior. Decreasing discharge capacities, as the series of cycles 269 to 276 shows, are observed regularly as a consequence of successive over activation of the electrodes due to high charge insertion.

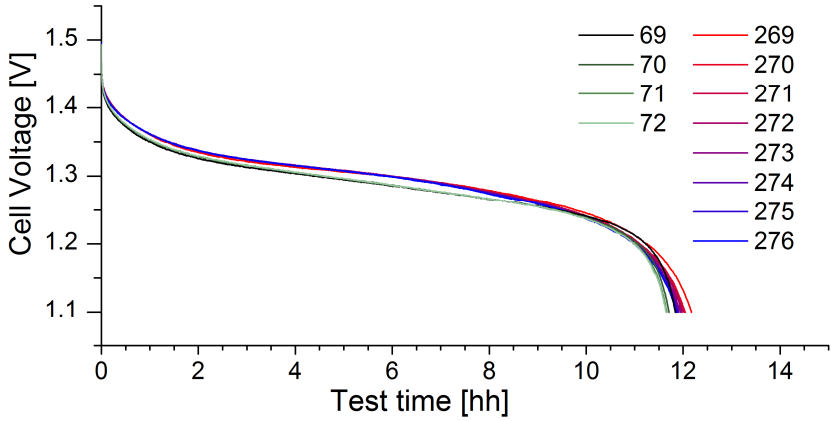

Figure 5.8: Discharge - series of SC at 35˚C proceeding tests with extended charge insertion (cell C2)

For comparison and for completeness the discharge curves of cycles 69-72, the first standard cycles performed at 35˚C, are added to Figure 5.8. Both, the discharge capacity and the discharge voltage are increased with lifetime. After cycle 72 an amount of 1437Ah of charge was inserted to the cell of which 546Ah were used for water splitting. Before cycle 269 an amount of 5931Ah of charge was inserted, of which 2511Ah were used for water splitting. Thus, over this period of testing, 450 times the nominal capacity of charge of the battery was inserted to the battery. Of this amount, 200 times the nominal capacity was used for electrolysis. No detrimental aging effect can be discerned.

5.1.3 Switching experiments

Figure 5.9 and Figure 5.10 present voltage curves of switching experiments, the first one shows continuous switching while the second one provides the results of a test program with various sequences.

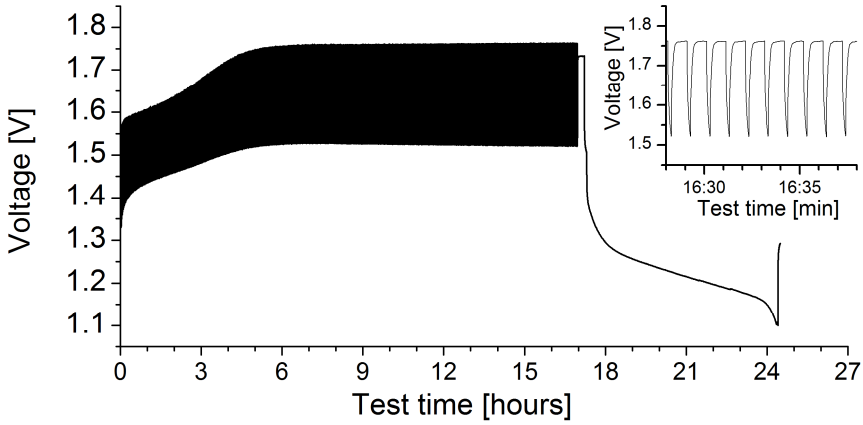

Figure 5.9: Continuous fast switching test, 1000 cycles of 50s charge insertion (C/2.5) and 10s of charge withdrawal (C/5) completed with a final discharge at RT (cell C4)

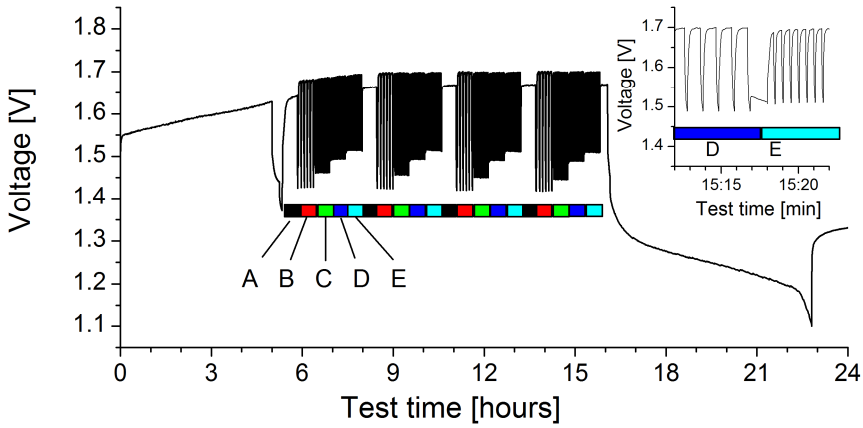

Figure 5.10: Switching test at charged electrodes: first 5 hour charge at C/3.33 rate then switching in sequence A to E, completed with a final discharge at 40˚C (cell C4, switching details see Table 4.2, chapter 4.1.3)

Stable operation under these harsh testing conditions is demonstrated by the fact that the maximum voltage during testing remains constant throughout the tests. The two inserts in the above figures show the reproducibility of the results; the voltage follows the applied currents directly without delay.

Figure 5.11 depicts the average sub-cycle efficiencies computed according to chapter 2.6.2 from the switching tests for sequences A-E. The calculation is based on the assumption, that all charge inserted is used for electrolysis or discharge, in other words, that the electrodes are fully activated. However, it can be concluded from Figure 5.10 that this assumption is not completely correct for the first cycle of sequence A-E because the potential during charge insertion did not reach a constant plateau as subsequent cycles show. Furthermore, it is known from previous charge retention tests, that the discharge capacity slightly increases with increased charge insertion (see Figure 5.5). The depicted efficiencies are the sequence average.

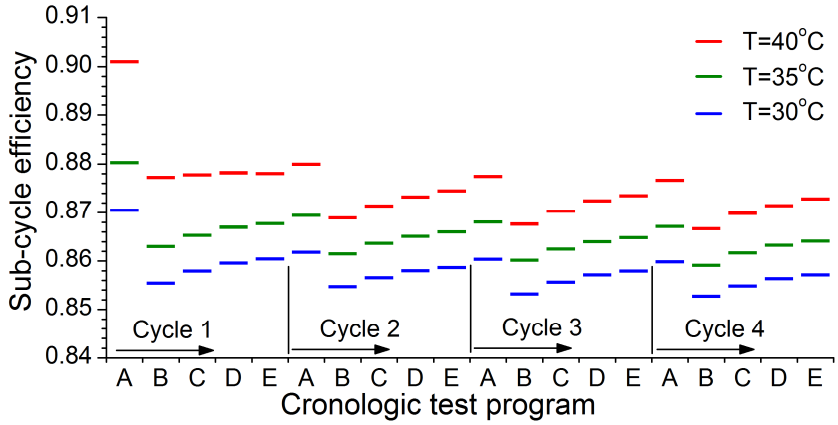

Figure 5.11: Sub-cycle efficiency for switching test at charged electrodes; tests performed at 30˚C, 35˚C and 40˚C.

Figure 5.11 shows that sequence A - constant charge insertion - has the highest efficiency in all cycles. Besides it can be observed that the efficiencies increase from sequence B to sequence E, meaning that short switching times are beneficial. It is remarkable that the efficiency of sequence E deviates less than 0.4% from sequence A considering that the potential for performing electrolysis at 4A are 1.4% higher than at 3A. Figure 5.12 presents the average charging/discharging potentials associated with each of the test programs.

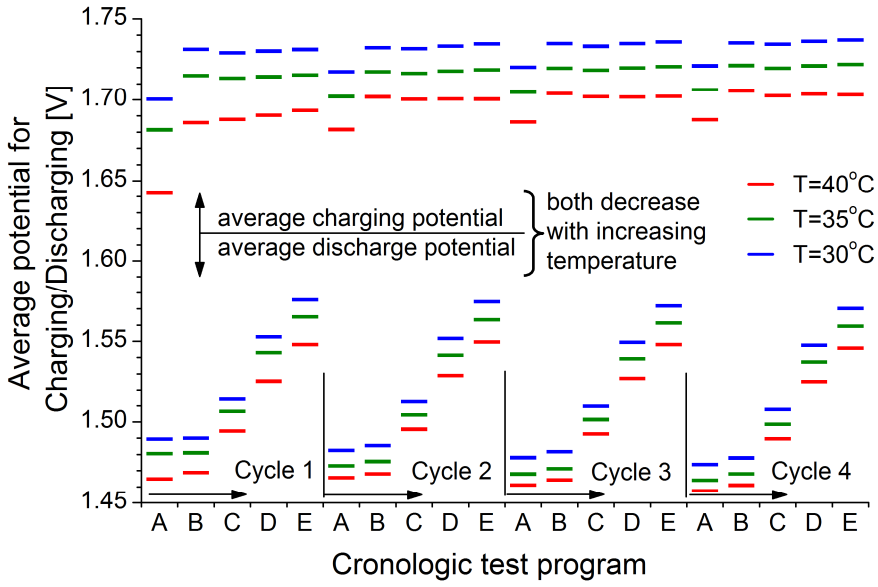

Figure 5.12: Average charging/discharging potentials for switching test at charged electrodes; tests performed at 30˚C, 35˚C and 40˚C.

The average potentials for charging are in line with what can be expected from electrolysis tests (see next chapter). For comparison the electrolysis potentials and efficiencies for charging rates of 3A and 4A are depicted in Table 5.8.

Table 5.8: Electrolysis potentials and efficiencies determined for charge rates of 3A and 4A at temperatures 30˚C, 35˚C and 40˚C (for details see chapter 5.1.4)

Charge rate	30 [°C]	35 [°C]	40 [°C]
3A (A)	1.712 / 0.865	1.695 / 0.873	1.676 / 0.883
4A (B-E)	1.736/ 0.853	1.718 / 0.861	1.699 / 0.871

However, the discharge potentials plotted in Figure 5.12 are remarkable: firstly because the average potentials increase with decreasing temperature; secondly because the magnitude of the average potential is far beyond the open circuit potential of 1.37 V, and even above the thermal neutral potential associated with water splitting for discharge times below 30 seconds (sequence C-E). This explains why shorter switching intervals are accompanied by higher efficiencies. It is also noteworthy that all switching sequences exhibit efficiencies above 85% despite elevated charge rates.

It is likely that these high potentials are caused by concentration effects. During electrolysis OH^- ions are formed at the Fe-electrode and consumed at the Ni-electrode. This effect would shift both electrode's equilibrium potentials according to the Pourbaix diagrams and the Nernst equation. The result would be a higher open cell potential.

5.1.4 Electrolysis potential

Tests were performed with the cells C1, C2 and C3. The results of the individual cells are reproducible. Figure 5.13 depicts the electrolysis potential dependence on applied current and temperature for cell C1.

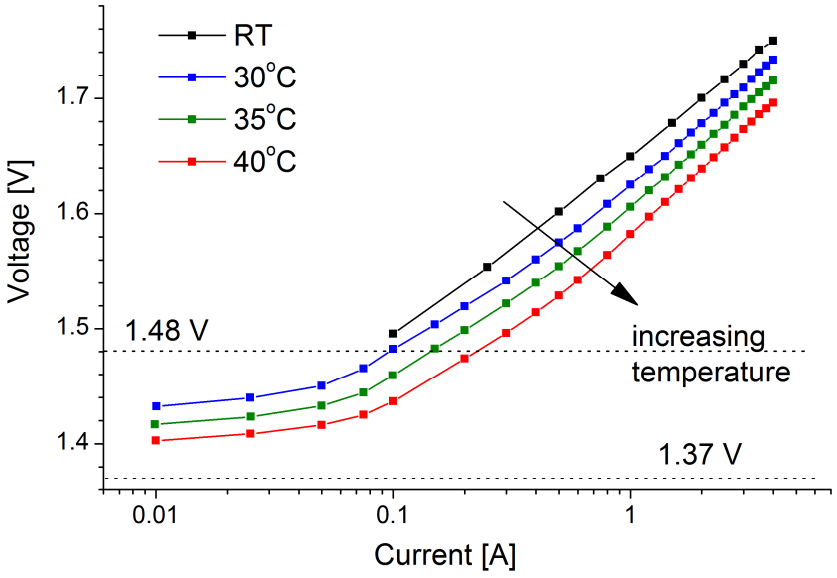

Figure 5.13: Electrolysis potential dependence on applied current for several temperatures (cell C1).

The electrolysis potentials increase with increasing current whereas the potentials decrease with increasing temperature. The tests were performed in an oven, heat was provided. For comparison electrolysis tests were also executed in an insulated box-setup without heat addition. Figure 5.14 provides the voltage and current curves as well as the temperature development during the tests (detailed test configuration see chapter 4.1.5).

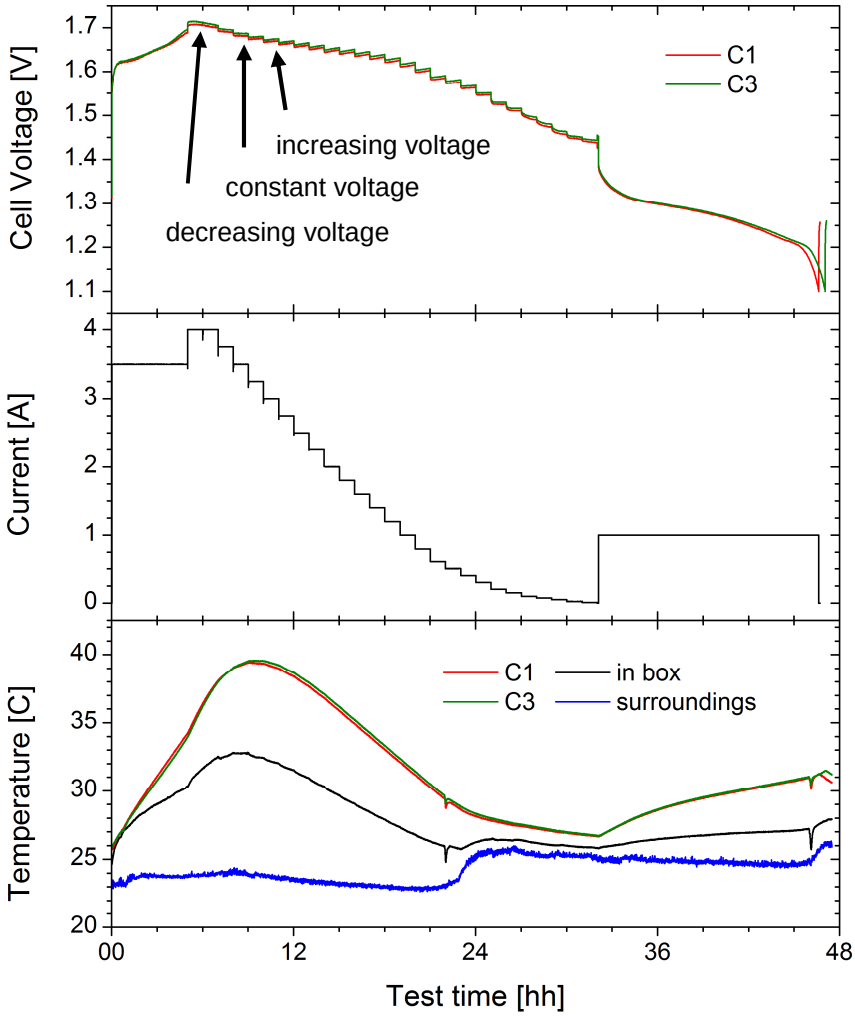

Figure 5.14: Electrolysis test in box-setup; Top: voltage curve of cell C1 and C3; Middle: applied current; Bottom: Temperature development of cell C1 and C3 as well as temperature in box and surroundings.

Figure 5.14 is a perfect example of the reproducibility of the test results. Not only are the voltage curves for cell C1 and C3 the same (aside from a slightly lower discharge capacity of cell C1, recognizable from the slightly earlier drop in cell voltage at the end of the program), but also the temperature development throughout the test is equal. For that reason, I conclude that the cells have the same overpotentials leading to the same heat production.

A detailed look at the voltage curve reveals (see inserts top of Figure 5.14) that cell voltage is decreasing at the start of the test, when the cell temperature is increasing, and that the cell voltage is constant at a current of 3.5A. At the same time the temperature in the box and cell temperatures are constant and at a maximum, meaning that there is equilibrium between heat production and heat losses. For the remainder of the procedure, the cell temperatures are decreasing. Because of that the potentials are increasing for a constant current insertion while the tests proceed at lower charge rates.

Figure 5.15 overlays the results of the electrolysis test of the insulated setup for cell C1 on the results presented in Figure 5.13. The electrolysis potentials that were observed with monitored temperature are in line with the potentials observed at constant temperature. The cell temperature is highest at currents of 3.0-3.5 A. At these current levels, the data points match the graph of 40°C, at current rates of 1.6A and 0.6A, the generated graph "in Box" passes the graphs for 35°C respectively 30°C, corresponding to the recorded cell temperature.

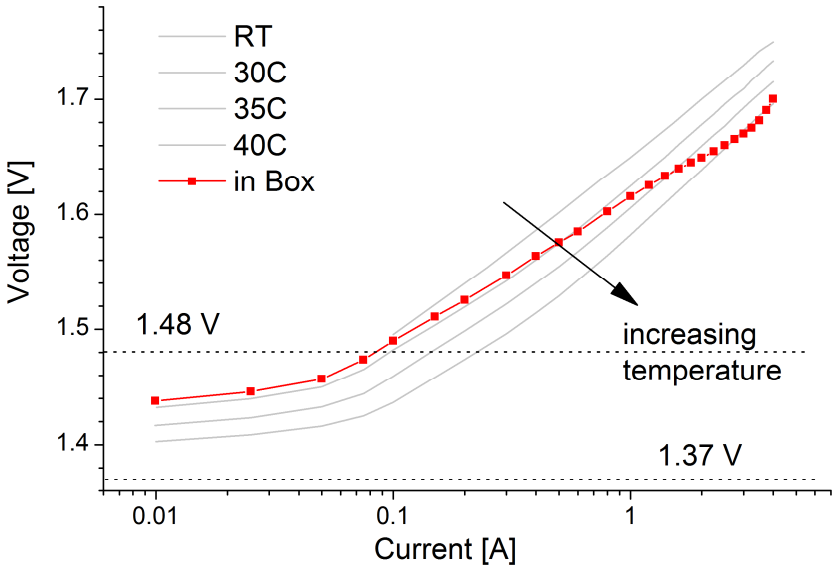

Figure 5.15: Electrolysis potential dependence in insulated box-setup in comparison with temperature controlled tests (see Figure 5.13).

I conclude that losses through overpotentials are converted to heat, leading to an increasing cell temperature in the box-setup. As the electrolysis potentials decrease with temperature, the cell operates more efficiently compared to a cell with no insulation at RT. The electrolysis potential at a current of 3.5A decreased from 1.742V at RT to 1.682V in the insulated setup, resulting in an efficiency increase from 85.0% at RT to 88.0 % with respect to the HHV.

Incidentally, the quality of the thermal insulation can be estimated from Figure 5.14. At a current of 3.5A the system is in equilibrium, heat generation equals heat losses leading to constant temperatures. The heat production can be estimated to:

$$\text{Heat production} = \#\text{cell} * \text{overpotential} * \text{current}$$
$$2 * (1.682 - 1.48)\text{V} * 3.5\text{A} = 1.414\ \text{W} \qquad (46)$$

and the heat transfer coefficient to:

$$\text{Heat flux} = \text{heat transfer coefficient} * \text{driving force}$$
$$\dot{Q} = \bar{h} * \Delta T \Rightarrow \bar{h} = \frac{\dot{Q}}{\Delta T} = \frac{1.414}{(32.8 - 24)} = 0.16\ W/K \qquad (47)$$

$\dot{Q}$ (W) and $\bar{h}$ (W/K) indicate heat flux and the heat transfer coefficient for the complete system. This estimated value is in agreement with the calculated heat transfer coefficient of 0.17 W/K for the system (see appendix C). No gas measurements were made during this test, so there was no Argon purge flow, which might otherwise have caused cooling.

Really large scale applications would necessitate further consideration of heat generation and insulation, as cooling may be required to limit the operating temperature. Figure 5.14 also indicates

that overpotentials during discharge lead to heat generation, since the cell temperature increases compared to the temperature of the surroundings.

For completeness, the monitored water loss (due to electrolysis and in the form of water vapor) of the mentioned electrolysis cycles is reported in Table 5.9. Again, water loss is highest at high operation temperature, which is caused by the larger amount of water loss in the form of water vapor.

Table 5.9: Measured weight loss ratio of electrolysis cycles for cell C1, C2 and C3; this is the expected water loss due to electrolysis divided by the actual water loss, which includes both electrolysis and water vapor loss (in %)

cycle	Temperature [°C]	C1 [%]	C2 [%]	C3 [%]
53	RT	96.7	98.2	97.0
68	40 °C	92.4	93.1	91.6
73	35 °C	93.5	94.5	93.1
81	30 °C	94.3	96.8	95.3
228/199	in box	92.4	-	92.8

5.1.5 Combined temperature and gas measurements

Gas measurements form an essential part of the work, as they are needed to verify the assumption that all the charge difference between insertion and withdrawal is used for water electrolysis. This is related to the Coulombic/Faradaic efficiency of the process. Figure 5.16 and Figure 5.17 depict results of combined temperature and gas measurements. In Figure 5.16, the results from the charge retention tests are shown, and in Figure 5.17, the results from the intermittent charge-discharge tests. The figures show voltage and current graphs on top, normalized electrolytic gas production in the middle, and temperature development against test time at the bottom. The tests were performed in the thermally insulated setup, see chapter 4.1.5.

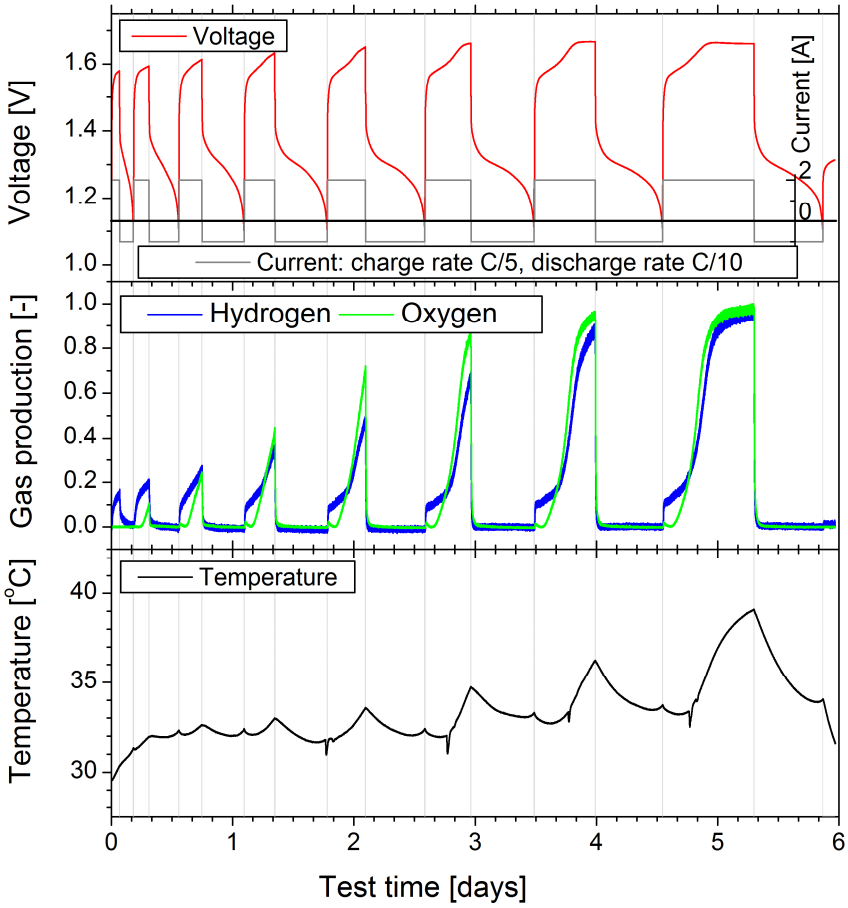

Figure 5.16: Battery and electrolysis yield. Top: Observed potential during constant current insertion over increasing durations, followed by a full discharge to 1.1V. Middle: Resulting normalized hydrogen and oxygen evolution. Bottom: Temperature development for the thermally insulated cell.

Hydrogen evolution starts immediately at small rates, while the onset for oxygen evolution is delayed. The normalized oxygen evolution catches up later and surpasses hydrogen evolution at about 0.8C (4 hours after the start of each current insertion). Overall, stoichiometric gas evolution takes place. During discharge, a fast decrease of gas evolution towards zero is observed. This is in line with earlier gas measurements of Ni-Fe batteries that were performed to characterize the composition of the produced gas to evaluate explosion risk [51]. During battery charge and discharge, or electrolysis, the temperature increases when the overpotential increases relative to the open-circuit voltage of the battery, or the thermoneutral potential. Interestingly the gas evolution is not constant during electrolysis. This is explained by increasing device temperature, which promotes self-discharge and electrolysis, as both processes lead to increased gas yield and reduced discharge capacity.

Figure 5.16 shows the following: the decrease in cell voltage caused by increasing cell temperature recognizable during the last current insertion step; self-discharge visible through detected hydrogen evolution during the rest period after the final discharge; and cell decreases temperature when the cell voltage is between 1.25 V and 1.58 V. Beyond these values, the overpotentials heat up the cell. The onset potential for oxygen evolution can also be estimated at 1.58V under the condition that one from an uncharged nickel electrode ($Ni(OH)_2$).

Figure 5.17 provides additional information about intermittent charge, discharge, and rest periods. The program starts with 12 cycles of 3/5 hours charge insertion at a rate C/3.33 with subsequent 1/5 hour discharge at alternating C/5 and C/10 rates and 1/5 hour rest. Again it can be observed,

that hydrogen evolution starts immediately, while oxygen evolution is delayed but catches up, when the electrode nickel becomes charged (NiOOH). NiOOH is clearly the more active oxygen evolution catalyst.

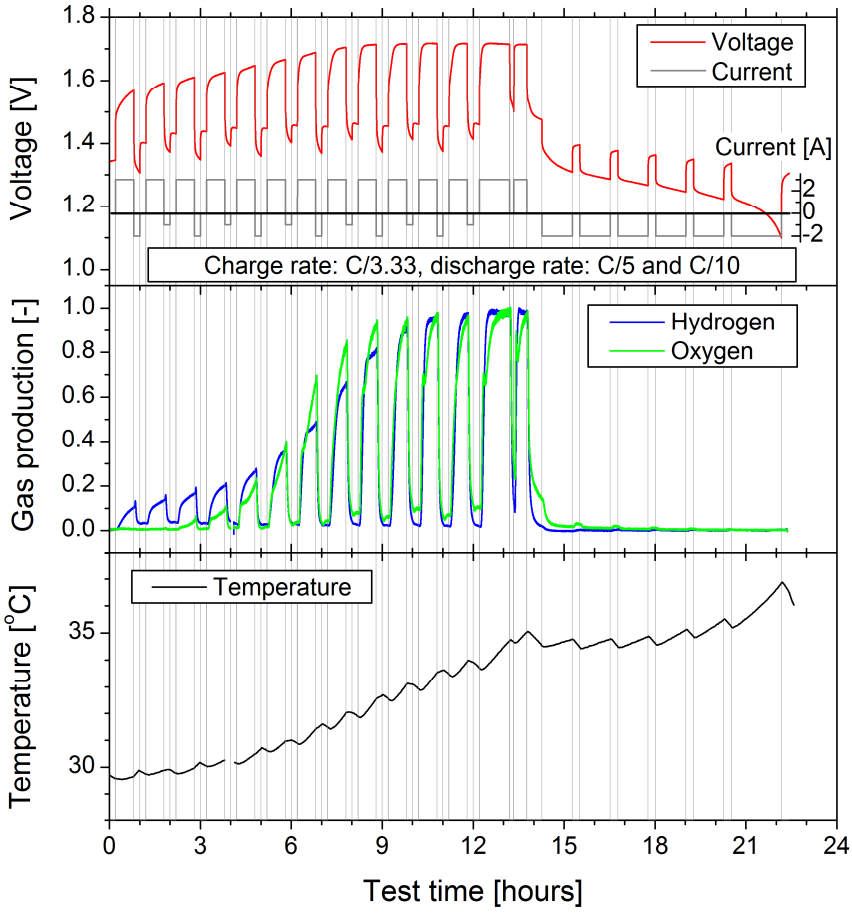

Figure 5.17: Intermittance and current handling. Top: Sequence of intermittent charge, discharge, and rest steps that show the switching capabilities of charge insertion followed by immediate current withdrawel, rests, and electrolytic gas evolution. Middle: the measured hydrogen and oxygen yields. Bottom: the temperature of the insulated cell following the instantaneous heating from residual overpotential losses due to Ohmic resistances.

Interestingly, after onset of oxygen evolution in sub-cycle three, oxygen evolution starts immediately in subsequent sub-cycles, partial discharge does not lead to delays but just to a drop in magnitude. Furthermore, the rate of discharge effects not only the cell potential but also the magnitude of oxygen evolution. Sub-cycles 7,9 and 11 with a C/5 discharge rate indicate a faster decrease and lower magnitude of oxygen evolution compared to sub-cycles 8, 10 and 12 performed with a C/10 discharge rate. The magnitude of oxygen evolution increases in adjacent rest periods. It appears that the hydrogen evolution is not affected by discharge rates.

After final charging and a rest period, the discharge program starts. After 30 minutes resting the cells start with discharging. The discharge program consists of five discharge steps of an hour with subsequent rest periods of 15 minutes and final discharge to 1.1 V are . It can be observed, that during the initial rest period the gas evolution rate of hydrogen drops much faster than the rate of oxygen. Even after 30 minutes rest the oxygen evolution rate is at about 10 % of the maximum value. Discharging causes both rates to drop to zero while intermittent rest periods show increased gas detection.

Analyzing the cell temperature during the test program reveals that the cell temperature always increases during charging and discharge at a C/5 rate and that the cell temperature decreases during rest periods and discharge at a C/10 rate. During discharge it can be observed that the overpotential increases with time as the slope of the temperature graph increases.

5.1.6 Water loss

The results presented so far show increased water losses with increasing temperature and charge rate, see Table 5.1, Table 5.2 and Table 5.9. To further support this statement, Table 5.10, and Table 5.11 provides additional weight loss data to the numbers provided before.

Table 5.10: Cycle number and water loss ratio (%) to charge retention tests of Figure 5.1 (cell 1), and equivalent performed with cell C4 (Charge rate 3A and discharge rate 1A)

Test temperature	30 [°C]	35 [°C]	40 [°C]
C1, Cycle numbers	128-134	121-127	139-145
C1, weight loss ratio (%)	97.4	94.9	92.6
C4, Cycle numbers	58-64	51-57	69-75
C4, weight loss ratio (%)	99.2	97.1	94.9

Table 5.11: Cycle number and water loss ratio to charge retention tests of Figure 5.2 (cell 2) and equivalent performed with cell C4 (Temperature 35˚C and discharge rate 1A)

Test charge rate	2 [A]	3 [A]	4 [A]
C2, Cycle numbers	149-156	157-165	169-176
C2, weight loss ratio (%)	97.9	96.7	94.2
C4, Cycle numbers	115-122	123-131	135-142
C4, weight loss ratio (%)	97.9	97.2	94.6

The water loss presented in Table 5.1 (with a charge rate of 4A) might seem low in this context, but it should be kept in mind that the cycle with a discharge rate of 3A was the last one this test-series. As the discharge capacities decrease with increasing discharge rates , the cell was not discharged to the same state and charge remained in the cell. Subsequent cycles show increased water loss leading to an overall compensation for this effect, see Table 5.12.

Table 5.12: Cycle number and water loss ratio to switching tests Figure 5.9 to Figure 5.12(cell 4)

Test temperature	RT (Figure 5.9)	30 [°C]	35 [°C]	40 [°C] (Figure 5.10)
C4, Cycle number	36	97	85	40
Test	Continues switching	Tests with various switching sequences		
C4, weight loss ratio	97.6	94.6*)	94.5*)	93.2

*) both tests follow test programs with a final discharge performed at high discharge rates (see Figure 5.3 and Table 5.1). Consequently, the calculated water loss might be too high.

5.1.7 Summary

The test-series that was designed to simulate various real-life situations, including partial and full charging and discharging, rapid switching, continuous overcharging, as well as the around-the-clock cycling, has by now been operational for over a year. The results until November 2015 for cell C2 are presented in Figure 5.18. After November, the array configuration was used. The results from then until now are presented in Figure 5.19. Table 5.13 provides an overview for all batteries. The experiments prove to be fully reproducible between the cells. The remarkable finding is that the energetic efficiency is stable at 80-90% over many different types of cycles, as are the reversible discharge capacities of the battery. Neither the battery, nor the electrolysis are harmed by the many cycles that include battery overcharges of up to 6 times the nominal capacity, rapid current reversals and deep discharges for each cycle. During the test period, cell C2 consumed 1073.6 g of water, of which 1038.7 g (96.7%) was expected from electrolysis. The remainder is lost through evaporation via the exhaust valves, together with the gas release. Since the cell contains around 70 ml electrolyte, the contents has been replaced over 15 times, the cells still operate with the initial electrolyte, only demineralised water was added.

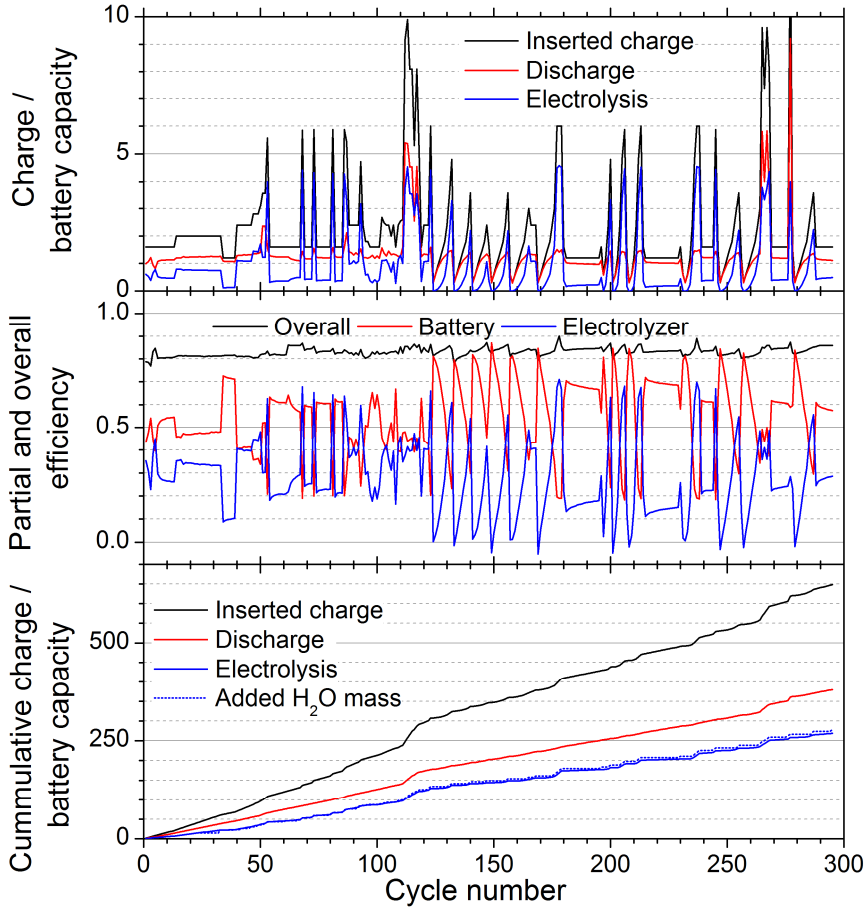

Figure 5.18: Long-term cycling and efficiencies of cell C2. Top: Inserted charge and discharge capacity for each cycle. Middle: Overall energy efficiency as sum of partial battery plus hydrogen gas efficiency. Bottom: cumulative inserted charge and breakdown in battery charge and electrolysis, and the cumulative H_2O mass to replenish the electrolyte expressed with respect to the battery capacity.

Certain trends can be distinguished in Figure 5.18 and Figure 5.19. Cycles with high battery efficiency go along with low charge insertion and cycles with high electrolysis efficiency with high charge insertion. Subsequent increasing charge insertion as visible between cycle 120 and 160

represent charge retention test, starting with low charge insertion up to several times the nominal capacity.

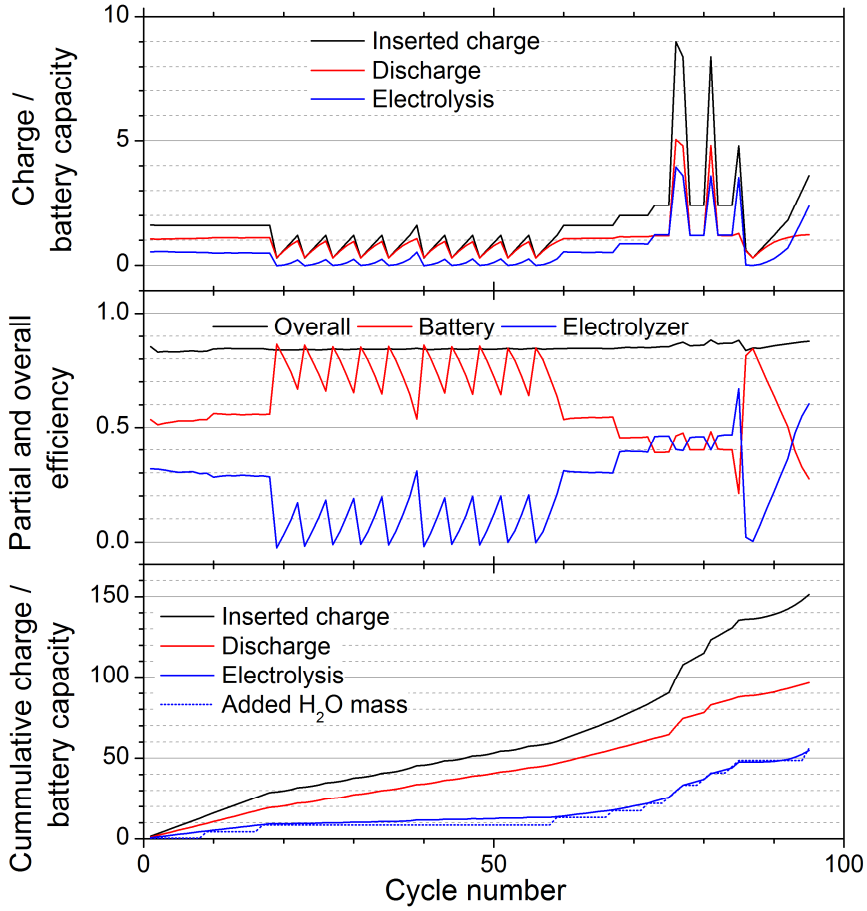

Figure 5.19: Long-term cycling and efficiencies of series array configuration. Top: Inserted charge and discharge capacity for each battery and cycle. Middle: Overall energy efficiency as sum of partial battery plus hydrogen gas efficiency. Bottom: cumulative inserted charge and breakdown in battery charge and electrolysis, and the cumulative H_2O mass to replenish the electrolyte expressed with respect to the battery capacity. (The latter was often only replenished after many cycles, which explains why the dotted line is often below the electrolysis line.)

Table 5.13 depicts performance characteristics of the cells. Adding up the inserted charge respectively electrolytic electrolysis of the single cell setup (C1-C4) with the array configuration shows that nearly 8000Ah of charge were inserted, 800 times the nominal cell capacity, and that electrolysis was performed up to 320 times the nominal cell capacity Executing tests in the array configuration with 4 cells in series demonstrates that scaling up the system in a series connection of cells is feasible.

Table 5.13: Performance characteristics - overview

cell	Counted cycles	Inserted charge [Ah]	Discharge [Ah]	Electrolysis [Ah]	Water usage [g]	Added H_2O mass [g]	ratio [%]
C1	298	6341	3880	2461	791.40*)	840.4*)	106.2
C2	295	6487	3798	2689	854.8*)	885.1*)	103.5
C3	268	6255	3781	2474	785.6*)	826.6*)	105.2
C4	261	5415	3075	2340	786.3	808.0	102.8
Array C1-C4	95	1513	966	547	183.9	188.5**)	102.5

*) Added H_2O mass for cell C1, C2 and C3 was recorded continuously from cycle 23 on. Water usage is computed from cycle 23 onwards.

**) average water replenishment per cell.

The following general conclusions can be drawn so far:

- The cycle efficiencies are stable and range between 80 and 90%
- The cycle efficiencies increase with increasing temperature, increasing charge insertion and decreasing charge and discharge rates
- Intermittent charge-discharge is always beneficial in the view of efficiency
- Switching is beneficial in the view of efficiency
- Operation at higher temperatures and charge rates cause additional water consumption due to evaporation
- The results are reproducible, also in the array-configuration, scaling up is feasible
- The cells show stable operation and they withstand the applied abuse

5.2 Tests with varying electrolytes

Ni-Fe batteries and alkaline electrolyzers both operate with potassium hydroxide as electrolyte, only the concentrations of potassium hydroxide are different. Moreover Ni-Fe batteries additionally utilize Lithium hydroxide, as it should have a positive effect on the electrodes cyclability. The addition of LiOH increases the overpotential for water splitting, which leads to less water splitting and decreases the conductivity of the electrolyte. The objective of this test-series is to find the best electrolyte for the battolyzer. Points of interest are primarily:

- Charge retention
- Electrolysis potential
- Efficiency

All three cells, C6, C7, and C8 were activated and tested with the same electrolyte as a reference point for further testing. Figure 5.20 displays the voltage capacity curve for charging the cells to 24Ah and for discharging the cells after a charge insertion of 3Ah, 6Ah, 9Ah and 24Ah. Figure 5.21 displays the discharge capacity of the performed charge retention tests.

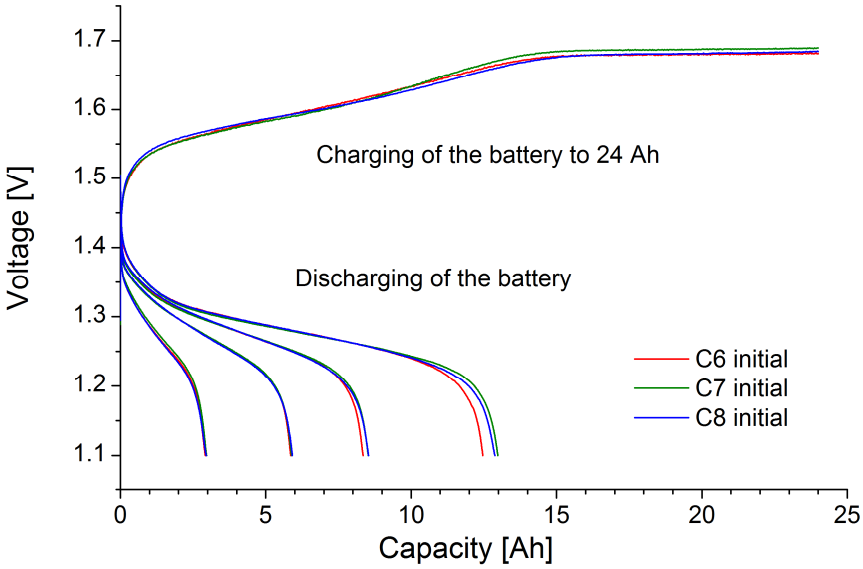

Figure 5.20: Voltage vs. capacity curves with initial electrolyte; plotted charge curve: charge insertion 24Ah; plotted discharge curves for prior charge insertion of 3Ah, 6Ah, 9Ah and 24Ah.

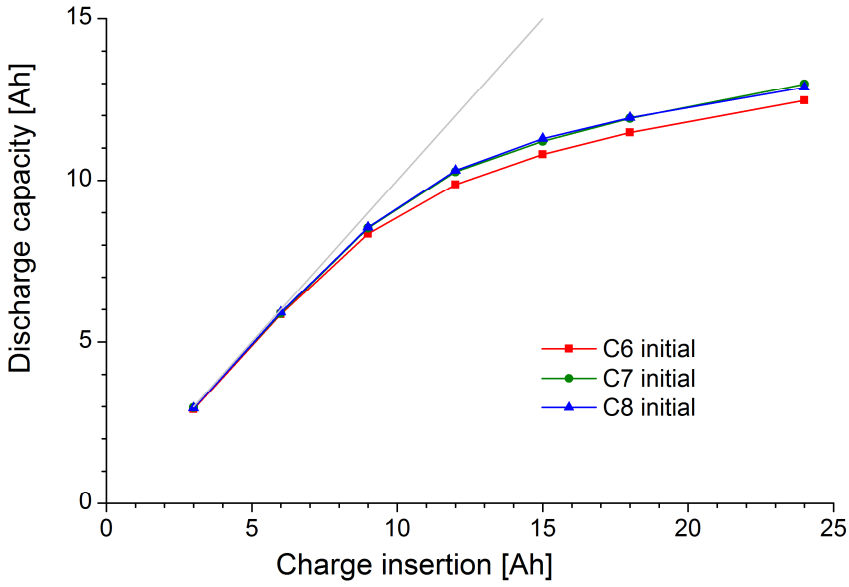

Figure 5.21: Discharge capacity vs. charge insertion with initial electrolyte

The cells are nearly equivalent as the graphs for charging and discharging follow the same pattern (see Figure 5.20). However, from the discharge curves it can be observed that the voltage of C6 starts to drop earlier, resulting in a lower discharge capacity for this cell. Figure 5.21 reflects this observation, all cells have the same discharge capacity up to a charge insertion of 6Ah. After higher charge insertion, the discharge capacity of cell C6 slightly decreases relative to the other cells.

5.2.1 Characterization of charge insertion and electrolysis potential

Figure 5.22 shows the measured voltage capacity curves for charge insertion of up to 24Ah for the three test cells for all executed experiments. As the cells vary slightly, the results are plotted per cell to be able to monitor changes caused by electrolyte change.

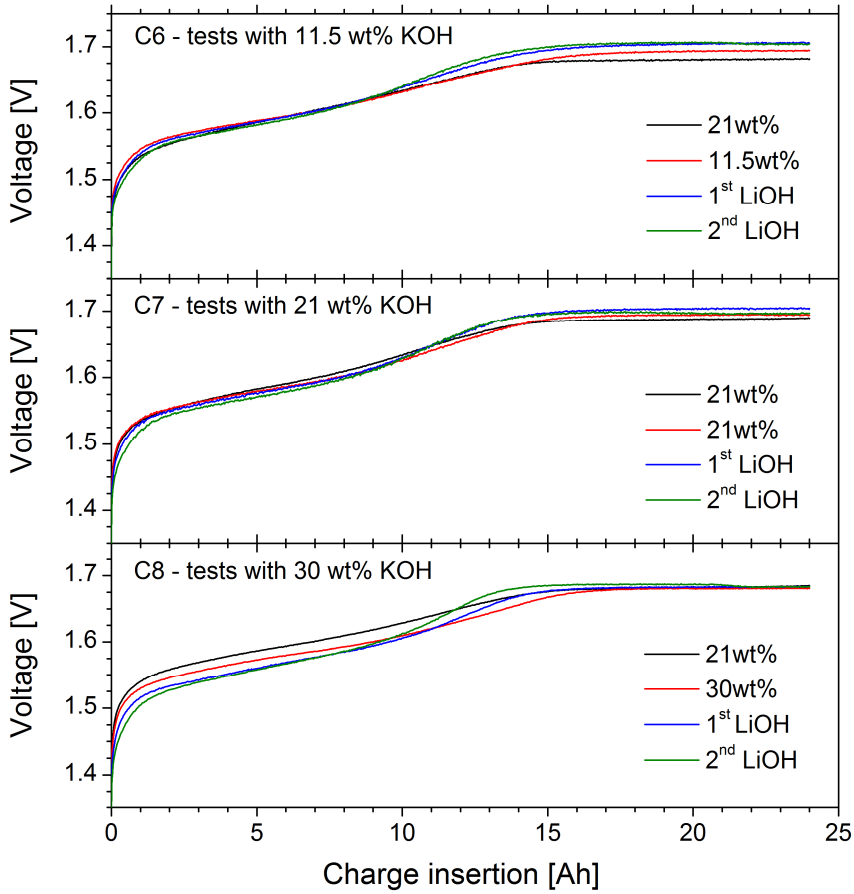

Figure 5.22: Voltage vs. capacity curve for charge insertion up to 24Ah for cells C6,C7 and C8 operated with various electrolytes.

Reducing the electrolyte concentration (cell C6) leads to an increase in initial potential and electrolysis potential, while the intermediate area (between 3Ah and 14Ah charge insertion) remains unchanged. Keeping the concentration constant (cell C7) shows no initial change, while the potential during charging is slightly decreased and the potential for electrolysis is increased. A rise in electrolyte concentration of up to 30 wt% KOH (cell C8) has the most recognizable effect, the voltage during charging drops around 25 mV, the electrolysis potential remains unchanged.

Furthermore it can be observed from all three curves that the onset of the electrolysis potential is delayed when comparing initial tests (black lines, constant potential for charge insertion above 15Ah) to the 2nd test-series (red lines, constant potentials for charge insertion above 17Ah). Adding LiOH reverses this effect, the onset for a constant potential for electrolysis is shifted back to 15Ah charge insertion.

The effect of LiOH addition is twofold: charge insertion is favored at the start of the charging process, resulting in lower potential, while electrolysis is not favored, resulting in a higher electrolysis current. The first effect is best visible at high KOH concentrations (cell C8, 30wt% KOH) while the second effect is best visible at intermediate and low KOH concentrations. Figure 5.23 shows the measured electrolysis potentials. The displayed potentials are computed as average potential for the last 15 test minutes.

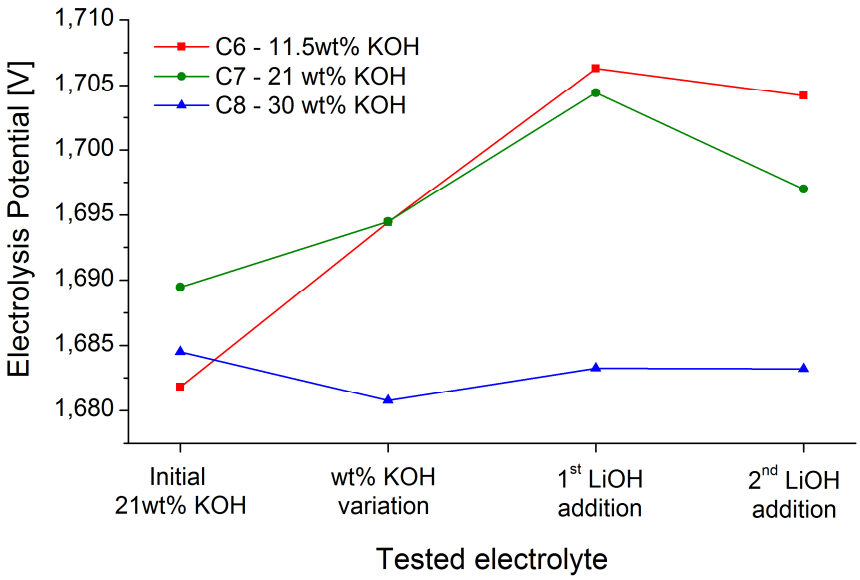

Figure 5.23: Electrolysis potential (average potential for last 15 test minutes)

Interestingly, the potential increases after the 1st addition of LiOH, while it decreases after the 2nd addition of LiOH. In both cases, the potential is higher than the potential determined with the pure KOH solution. Table 5.14 depicts the determined electrolysis potentials.

Table 5.14: Determined electrolysis potential for 24 Ah charge insertion

Electrolysis potential [V]	Initial 21wt% KOH	wt% KOH variation	1st LiOH addition	2nd LiOH addition
C6 - 11.5 wt% KOH	1.682	1.694	1.706	1.704
C7 - 21 wt% KOH	1.689	1.694	1.704	1.697
C8 - 30 wt% KOH	1.685	1.681	1.683	1.683

5.2.2 Characterization of discharge potential and charge retention

Figure 5.24 shows the discharge curves measured after charge insertion of 24Ah. LiOH favors, besides charging, as observed during charging, also discharging. This can be seen from the fact that the initial discharge-potential is higher when LiOH is added. However, this effect decays as the potential drops below the potentials of pure KOH electrolytes with time. This effect can be attributed to the reduced conductivity of the electrolyte upon LiOH addition [2], best visible at high KOH concentrations (cell C8).

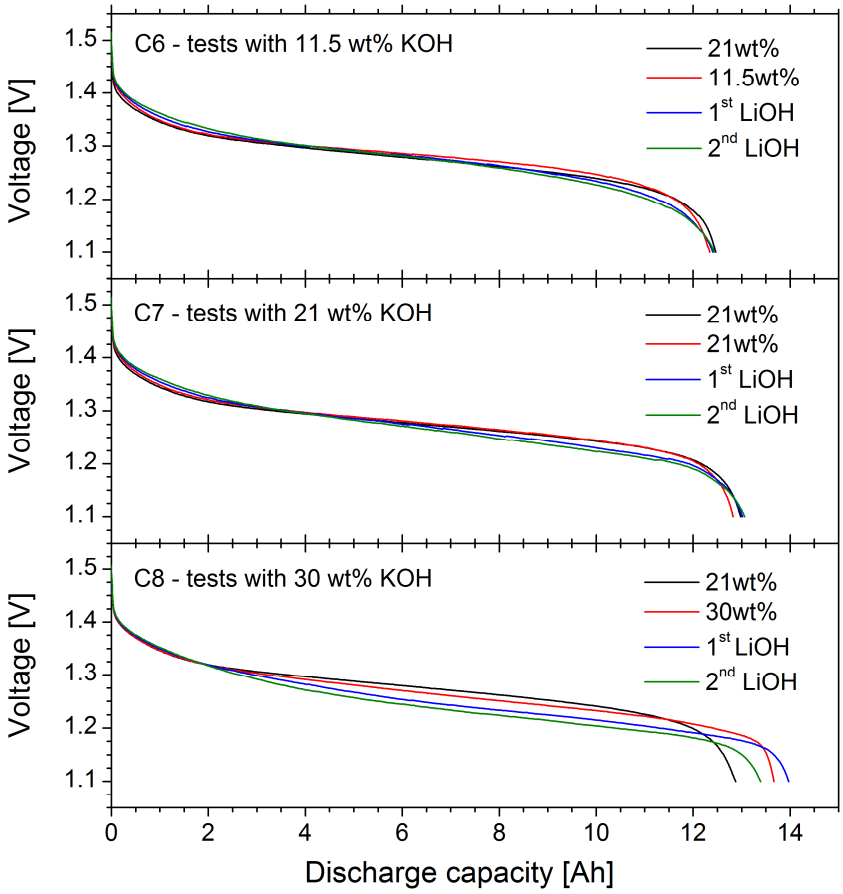

Figure 5.24: Voltage vs. discharge capacity curves determined subsequent to a charge insertion of 24Ah

Reducing the electrolyte concentration (cell C6) hardly has an effect on the discharge curve. The observed voltage is even - against expectations, considering the conductivity of the electrolyte - slightly higher than the voltage of the reference case. Only at the end of the discharge process, does the voltage drop faster, leading to a lower discharge capacity. Keeping the electrolyte concentration constant (Cell C7) displays two almost identical discharge curves, only the voltage drop at the end of the discharge cycle is faster. Remarkable is the effect of increasing the concentration of KOH (cell C8), as the discharge capacity increases from 12.9Ah to 13.7Ah. The observed discharge voltage of the high concentration electrolyte (red line) is below the discharge voltage of the reference case, again this is against expectations considering the conductivity of the electrolyte.

In all cases the discharge capacity increases with the first addition of LiOH, compared to an electrolyte with the same concentration of pure KOH, see Table 5.15 (column wt% KOH variation vs. 1st LiOH addition).

Table 5.15: Determined discharge capacity for a previous 24 Ah charge insertion

Discharge capacity [Ah]	Initial 21wt% KOH	wt% KOH variation	1st LiOH addition	2nd LiOH addition
C6 - 11.5 wt% KOH	12.47	12.34	12.41	12.44
C7 - 21 wt% KOH	12.98	12.82	13.02	13.06
C8 - 30 wt% KOH	12.88	13.67	13.97	13.39

Further addition of LiOH leads to an increase in discharge capacity for the case of low and intermediate KOH concentration, but the discharge capacity decreases for the high concentration case. This could be attributed to the higher resistance of the electrolyte, recognizable in the lower discharge voltage curve, see Figure 5.24, green line vs. blue line in bottom graphic. The determined charge retention for all tested values of charge insertion is depicted in Figure 5.25.

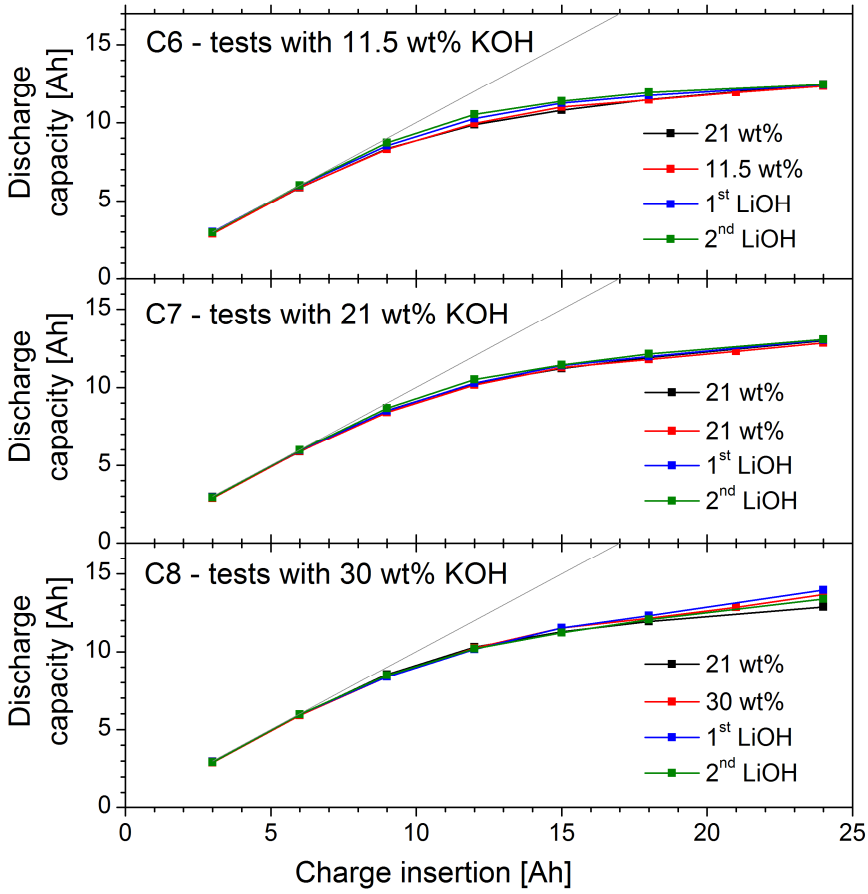

Figure 5.25: Discharge capacity for previous charge insertion from 3Ah to 24Ah

Changing only the KOH concentration of the electrolyte has limited effect on the discharge capacity. In all cycles apart from the high concentration charge cycle with 24Ah charge insertion (cell 8, Figure 5.24) mentioned above, the effect is within a bandwidth of 2% of the initial capacity.

Adding LiOH has a positive effect on the charge retention of the cells with low and intermediate KOH concentrations electrolytes. The highest effect, of +3% for the 1st LiOH addition, and +6% for the 2nd LiOH addition, is determined for cell C6 (low KOH concentration) at a charge insertion of 12Ah. The effect wears off to both sides and is not visible anymore for a charge insertion below 6Ah or 24Ah. C7 (standard KOH concentration) shows an increase of +1.5% for the 1st LiOH addition and +3% for the second 2nd LiOH addition for all values of current insertion. The effect of adding LiOH to 30 wt% KOH electrolyte (cell C8) varies for charge insertion up to 15Ah, the values are close together. For higher charge insertion, the discharge capacity increases after the 1st addition of LiOH while it decreases after the 2nd LiOH addition, both compared to the case with pure KOH electrolyte, see also Figure 5.24.

5.2.3 Efficiency

The last two chapters show, that changing the electrolyte concentration and adding LiOH has an influence on charge and discharge characteristics. Both the charge characteristics and the discharge characteristics affect the cycle efficiency. A higher voltage during charging and a lower voltage during discharging decrease the efficiency, while a lower voltage during charging and a higher voltage during discharging increase the efficiency.

Figure 5.26 depicts the cycle efficiency of the charge retention tests as defined in chapter 2.6. The following trend can be observed from all tests: a high efficiency for a charge insertion of 3Ah, followed by a decrease in efficiency with a minimum at a charge insertion of 6Ah for tests with the initial electrolyte (black lines; 21wt%) and for the test with 30wt% KOH with LiOH, and 9Ah for the other tests. Further charge insertion leads to an steady increase in efficiency. Low resistance to charge insertion at the start of the charging process, recognizable at the low voltage, leads to high efficiencies for low charge insertions. Increasing the charge insertion induces higher voltages for the charging process, which causes a decrease in efficiency. Steady increase in hydrogen and oxygen production with increased charge insertion leads to a subsequent increase of efficiency, since the voltage associated with electrolysis is the thermo-neutral potential of 1.48V, while the average potential for the discharge process is around 1.28V. Further charge insertion would further increase the efficiency up to a limit of approximately 87% which is the efficiency of 100% electrolysis with an assumed potential of 1.7 V for additional charge insertion (see Table 5.14).

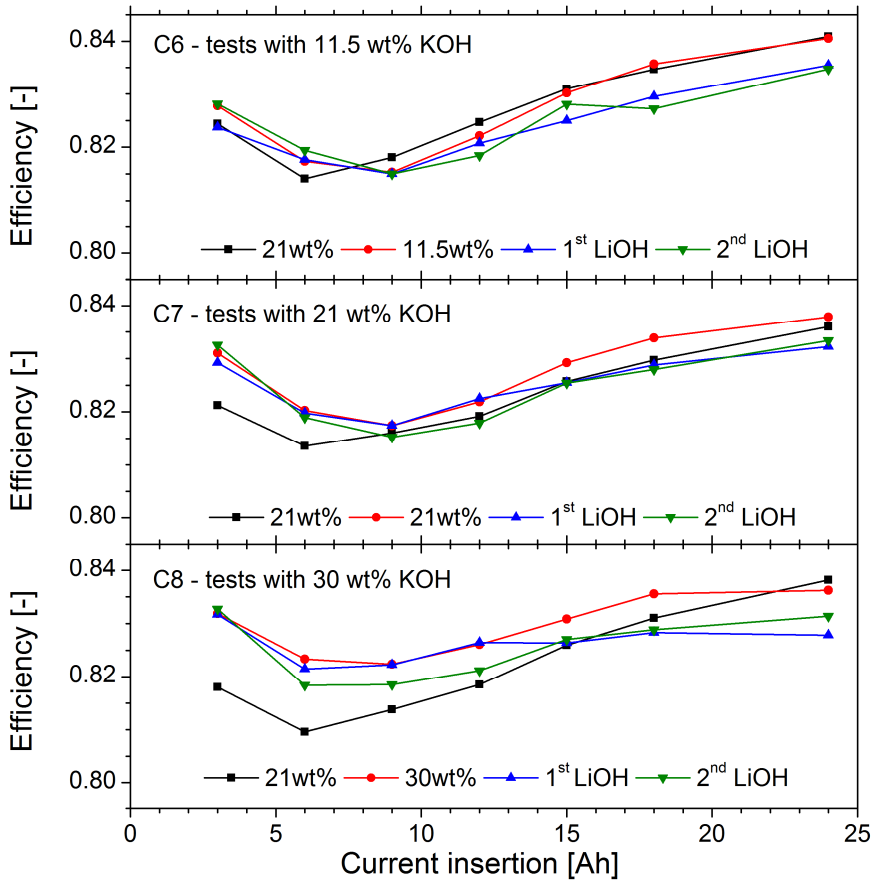

Figure 5.26: Cycle efficiency for charge retention tests with a charge insertion from 3 Ah to 24 Ah

Reducing the concentration of KOH (cell C6) has little effect on the efficiency. The values of KOH concentration of 11.5wt% are in the range of the initial concentration. Exchanging the electrolyte,

but keeping the concentration constant (cell C7) has a positive effect on the efficiency, all values are above the values of the initial test. Increasing the KOH concentration (cell C8) leads to an increase in efficiency, especially for low charge insertion. Only the last data point at a charge insertion of 24Ah is below the initial value. This is caused by the increased discharge capacity, see Figure 5.24.

The addition of LiOH has little effect on the cycle efficiency for a charge insertion up to 9Ah, the values are in the range of the tests with the same electrolyte KOH concentration (red lines). For charge insertion of 12Ah or higher the efficiency of tests with LiOH containing electrolyte is around 0.5 % lower.

In total 189 cycles have been performed with these three cells at room temperature. Figure 5.27 shows all cycle efficiencies. The variation of efficiency is limited and stays between 0.81 and 0.84. Furthermore is can be observed, that the cycles with 24Ah charge insertion show the highest efficiency. The higher efficiencies up to 90% are not reached here because tests were only performed at room temperature.

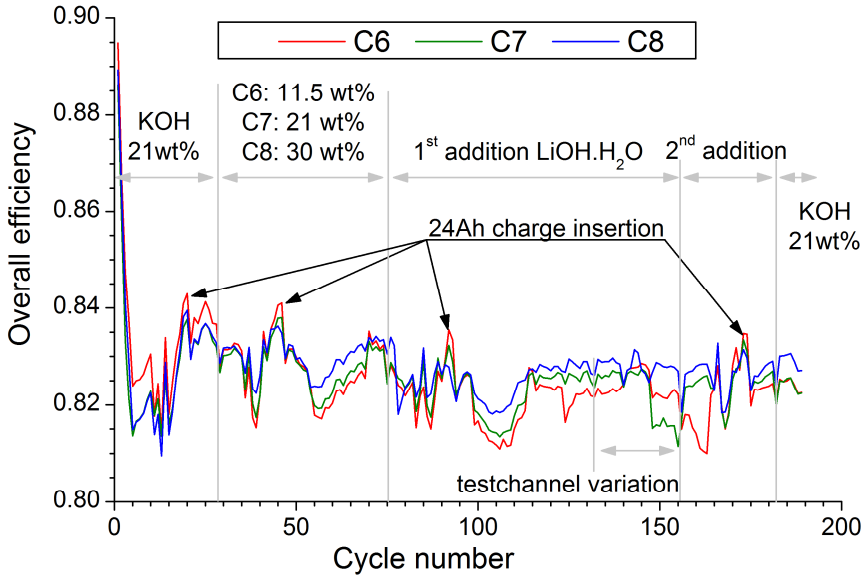

Figure 5.27: Cycle efficiency for all performed cycles

Most of the remaining cycles that were performed were standard cycles. It can be recognized that for normal battery operation, the cell with 30wt% KOH (cell C8) works most efficiently, while the cell with 11.5 wt% KOH (cell C6) operates least efficiently. The difference is approximately 0.5 %.

As mentioned earlier differences in the recorded voltages between the Maccor and the Keithley systems were identified during experimentation, see Table 4.1.

To investigate the suspected errors, the channel/battery configuration was changed. Cell C6 had been connected to channel 10, C7 to channel 11, and C8 to channel 12. For investigation of a possible error, the cells' connection was changed two times. After the first change, C6 was on Channel 11, C7 on Channel 12, and C8 on Channel 10. After the second change, C6 was on Channel 12, C7 on channel 10, and C8 on channel 11. In each case 8 SCs were performed, corresponding to cycles 140-147 and cycles 148-155 respectively. The cycles concerning testchannel variation are marked in Figure 5.27. It can be observed that C8 has the same efficiency, independent of the test channel, while C6 has the same efficiency when connected to channel 10 and 12 and a higher efficiency when connected to channel 11. C7 has the same efficiency when connected to channel 11 and 12 while it has a lower efficiency when connected to

channel 10 .The variation in test channel - even with correction - has a impact in efficiency. Not correcting the voltage has an even higher impact on the cell's efficiencies, see appendix B.

5.2.4 Water loss

The weight loss of the test cells was monitored and is depicted in Table 5.16.

Table 5.16: Determined discharge weight loss and weight loss due to electrolysis

	Weight loss [g]	Electrolysis [Ah]	Weight loss due to Electrolysis [g]	ratio
C6	244.8	762.9	247.7	1.012
C7	234.9	736.5	238.9	1.017
C8	239.6	733.1	237.7	0.992

The cells were charged with a moderate C/5 rate at room temperature. Neither the moderate charge rate, nor the low temperature, lead to extensive evaporation of water. The ratio of expected weight loss from electrolysis to monitored weight loss is close to 1.

5.2.5 Summary

The objective of this test-series is to find the best electrolyte for the battolyzer. Points of interest were especially:

- Charge retention
- Electrolysis potential
- Efficiency

As literature attributes may effects to the addition of LiOH to the electrolyte, it is remarkable that little influence has been noticed.

The charge retention increases upon addition of LiOH for charge insertion equal to the nominal battery capacity, but the effect decays with higher and lower charge insertion. This effect depends on the KOH concentrations and is most noticeable at low concentration.

The addition of LiOH has a positive influence on charging the batteries, the cell potentials drop. However, the effect on electrolysis and discharge potentials is not beneficial, electrolysis potentials increase whereas discharge potentials decrease.

All these characteristics influence the overall efficiency. The executed tests show that variation in the electrolyte has limited effect on the cell efficiency. The efficiency decreases upon addition of LiOH to the electrolyte, especially for high charge insertion to stimulate electrolysis, the bandwidth is within 1%.

The question remains, what is now the best electrolyte for the battolyzer?

In my point of view, the well-established concentration of 21wt% KOH is the best concentration for operating the battolyzer. The conductivity of the electrolyte hardly increases with increasing concentration, but decreases significantly when decreasing the concentration. However, the possibility of increasing the concentration should not be discarded, as electrolysis potentials are lowest for this case. From the viewpoint of efficiency, especially with high charge insertion, LiOH should not be used as an additive.

5.3 Tests with battolyzer.

Tests with the battolyzer were performed to demonstrate that the concept of operation as an integrated battery and electrolyzer works. The following features were tested:

- Cycling capabilities
- Internal resistance of the battolyzer with and without membrane
- Quantitative and qualitative gas characterization

5.3.1 Cycling capabilities

Several standard cycles have been performed with the battolyzer. The operation principles are identical to the operation principles of the tested batteries. The determined measured discharge capacity for these standard cycles is about 6.4Ah. This is in the expected range as the battolyzer has half the capacity of the conventional batteries, which have a measured discharge capacity of about 12Ah.

5.3.2 Tests with and without membrane

Figure 5.28 depicts the voltage curves of tests performed with and without membrane. The voltage curves for charge insertion up to a test time of 18 hours at 1A are almost identical, the insert provides a magnification of the period from 9 to 18 hours. The voltage in the configuration with membrane is slightly above the voltage of the configuration without membrane.

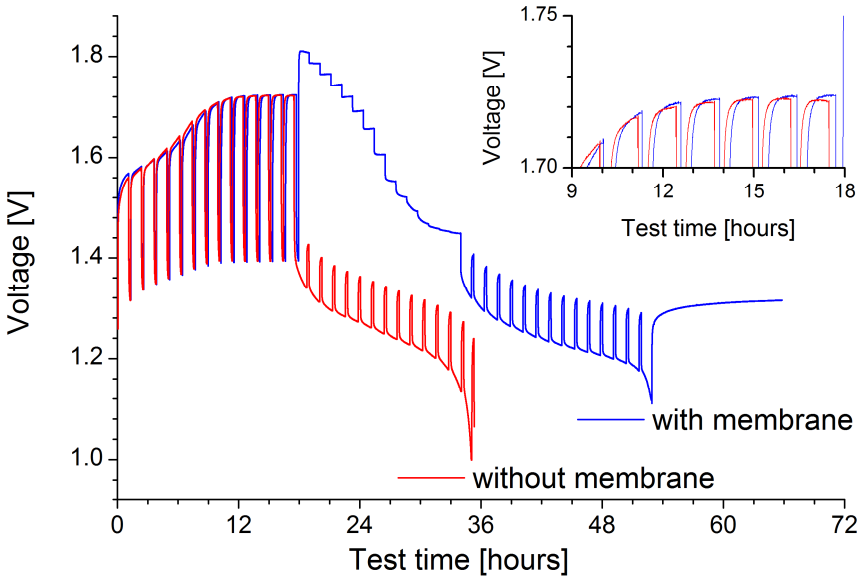

Figure 5.28: Voltage curves for a CP-test with intermittent EIS tests without membrane (red line) and the same test with intermediate Electrolysis test with membrane (blue line); insert depicts the last steps of constant charge insertion.

Figure 5.29 shows the Nyquist plots of constant current EIS tests, performed with the battolyzer with and without membrane. For comparison an equivalent plot for a conventional Ni-Fe battery is added. The EIS tests were executed at the charge electrode. In the case of the battolyzer the current for charging is 1A and for discharging is 0.5A, in the case of the Ni-Fe battery both rates are 2A.

Excursus EIS interpretation: Nyquist plots show the relationship between the real part of the impedance and the negative imaginary part of the impedance determined at various frequencies. The test starts with high frequencies and ends with low frequencies. The plot starts at the left were the imaginary part of the impedance is zero. The starting point at high frequencies reflects the cell's series resistance. Frequencies decrease when following the curve to the right. The frequencies are related to the charge carrier dynamics in the cell. Two semicircles are visible, one in the high frequency region and one in the low frequency region. The semicircle at high frequencies is associated with bulk charge transport and the semicircle at low frequencies is related to surface charge transfer. Actually, it should be possible to build an equivalent electronic circuit to model the system. However this approach was abandoned after consulting a colleague, as the EIS measurement in a two electrode measurement leads to ambiguous interpretation as the contributions of the working and counter electrode may overlap in the impedance spectra. To obtain a more accurate analysis, the EIS measurement should be carried out in a 3 electrode configuration using a reference electrode. That way, the impedance of the working electrode can be evaluated independently, and the contribution from the counter electrode can be limited. This approach is kept in mind for future work. For the interested reader, appendix D provides nyquist plots for charging and discharging the electrodes, for electrolysis at various rates, and for a 10 hour rest period.

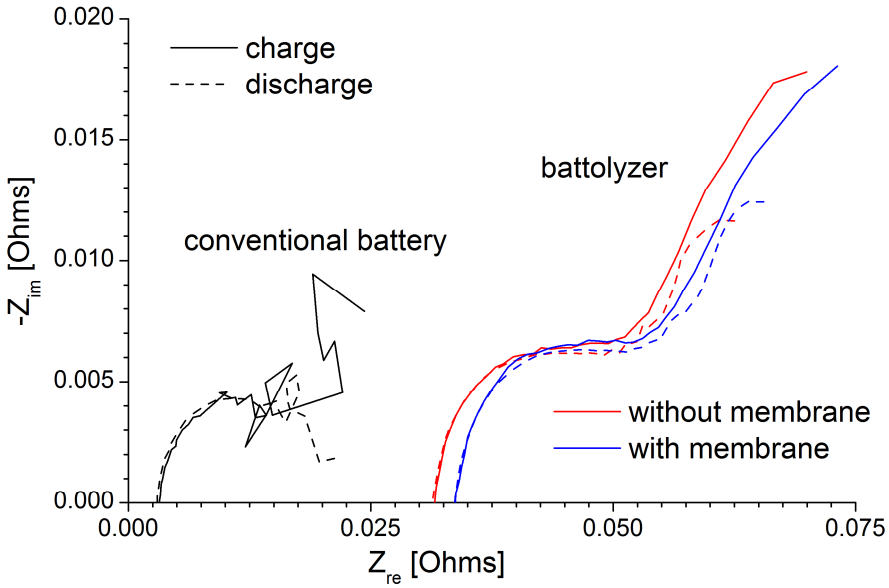

Figure 5.29: Nyquist plots for constant current EIS tests performed with a conventional battery and the battolyzer with and without membrane.

The internal resistance of the commercial cell is 3mΩ. The internal resistance of the battolyzer is 31.6mΩ without membrane and 33.7mΩ. with membrane The membrane causes an increase in resistance of 2.1mΩ. This value corresponds to 0.22Ω.cm², which is in agreement with the product specifications of Zirfon® where the maximum value of the membrane's resistance is defined as 0.3Ω.cm² at 30˚C.

The increase in internal resistance from 3mΩ for the conventional battery to 31.6mΩ for the battolyzer is caused by the relatively thin wiring of the battolyzer. The contribution of the wiring is

estimated to 27-30mΩ (see chapter 3.2.2). 0.2cm extra spacing between the electrodes also causes extra ionic resistance. This contribution can be estimated to 3mΩ (Electrolyte conductivity: 0.60 S/cm; active surface area: 105.3cm²).

Figure 5.30 shows the determined electrolysis potentials for the battolyzer, derived from the voltage curve depicted in Figure 5.28. Actually only the first ten and not all fifteen potentials are plotted, as no equilibrium was established at low current densities. Even the equilibrium for the lowest two current densities plotted in this graph is doubtful. In the first place no scaling factor was considered when writing the test program. The experimentally developed step-size in ampere of the batteries was duplicated as-was to test the battolyzer. Dividing by a factor two, to account for the halved nominal capacity should have been considered.

The electrolysis potentials of the battolyzer are plotted as measured and corrected. The correction compensates for additional ohmic losses caused by the wiring. The correction is a constant factor of 0.027mΩ, multiplied by the actual current.

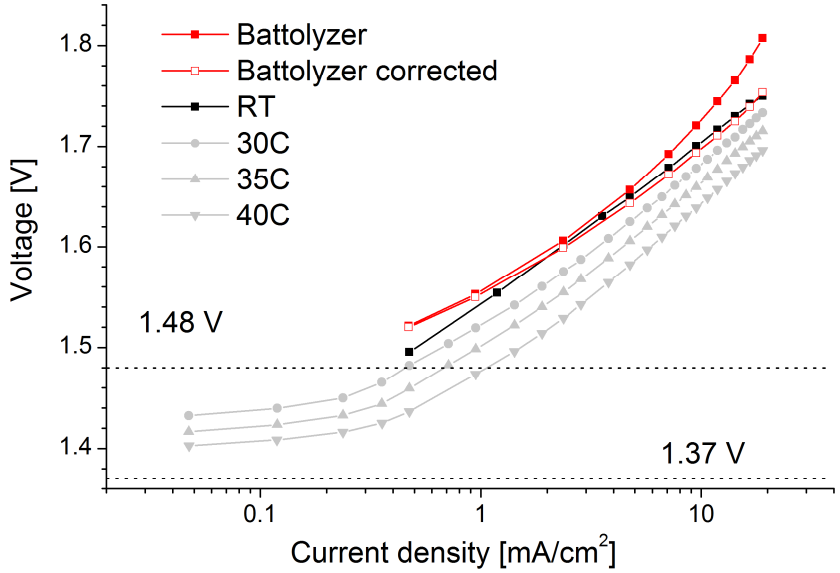

Figure 5.30: Electrolysis potential of the battolyzer without correction and with correction for additional ohmic losses relative to temperature-controlled tests (see Figure 5.13). The corrected voltage is the result of subtracting 0.027mΩ from the thin wiring of the battolyzer multiplied by the actual current from the measured voltage. The x-axis shows in the current plotted in current density. The current density is the test-current divided by the total open surface area between the compartments (= # of surfaces times open area per surface (35.1cm²))

The electrolysis potential of the battolyzer is above the potential for the battery at room temperature. At a current of 0.5 A and room temperature, all depicted potentials are similar. For higher currents, the potentials of the battolyzer deviate increasingly with increasing current. This deviation is caused by ohmic losses in the relatively thin electronic wiring to the outside of the battolyzer. The corrected values for the battolyzer's potential follow the battery's potential. Reducing the current also shows deviations, these deviations are caused by the programmed current's step-size error. Because of this error, no equilibrium is reached at low currents. These measurements show that efficiency results acquired through battery testing can be transferred to the battolyzer, assuming that the ohmic losses will be reduced in future versions. A robust bi-polar setup would be suited for this purpose, since that setup insures electronic contact through the entire surface of low electronic resistance bipolar plate.

5.3.3 Gas measurements

Gas measurements have been performed for three purposes:

- Gas separation capabilities
- Trace gas analysis
- Gas quantity

While efficient gas separation is essential to reduce losses, and for safety reasons, trace gas analysis and gas quantity measurements can be used to verify the absence of unwanted side reactions. Side reactions also decrease the efficiency of the system, but they can also indicate the instability of the electrodes.

All of the following tests have been performed with a previously activated electrode.

5.3.3.1 Gas separation capability

Figure 5.31 shows the gas detection for the separated H_2- and, O_2-compartments at various currents. The H_2-compartment, where hydrogen is produced, was tested first. Afterwards , the O_2-compartment, where oxygen is produced, was tested. The top of the graph displays the test current, beneath the test configuration is displayed. The graphs for hydrogen and oxygen include inserts with magnification of the unwanted gas production.

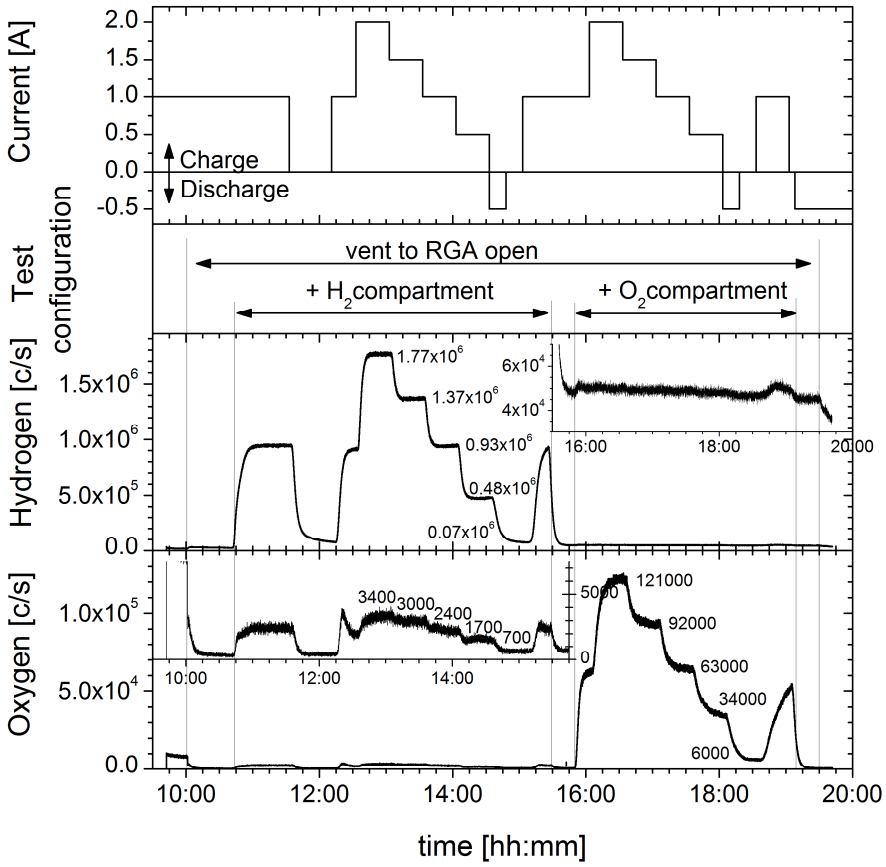

Figure 5.31: Gas separation capabilities of the battolyzer; first the H_2-compartment was tested, then the O_2-compartment. Before connection and disconnecting the H_2 and O_2 compartments the Argon purge gas is analyzed. There is always a background of H_2 and O_2 visible.

Production of both gasses - hydrogen and oxygen - scales with the current as these are the main gasses. The insert for hydrogen shows that there are hardly any fluctuations in H_2 concentration in the O_2 channel when the oxygen compartment is tested. This is good news! Interestingly a peak can be seen at the end of the test program, after the discharge/rest step. This could indicate gas crossover. The counts start to increase, then decrease a little later, while oxygen evolution continues to increase. Maybe the compartment's gas reservoir is not gas tight. The same pattern can be observed for oxygen evolution when the hydrogen compartment is analyzed. After the discharge/rest step oxygen evolution starts simultaneously with hydrogen evolution when current is applied. Again, but this time, oxygen evolution starts to decrease a little later, while hydrogen evolution continues to increase.

The insert in Figure 5.31 for oxygen evolution clearly indicates a charge dependent pattern for unwanted oxygen. Table 5.17 shows the detected counts for oxygen evolution for the oxygen and the hydrogen compartment as a function of the applied current.

Table 5.17: Rate dependent counts of O_2 from the H2-compartment and the O_2-compartment

	O_2- compartment		H_2- compartment		
Charge rate	measured [c/s]	without background	measured [c/s]	without background	ratio
Background	6,000	-	700	-	[%]
2A	121.000	115,000	3,400	2,700	2.3
1.5A	92,000	86,000	3,000	2,300	2.7
1A	63,000	57,000	2,400	1,700	3.0
0.5A	34,000	28,000	1,700	1,000	3.6

The ratio between unwanted and expected oxygen counts increases with decreasing current from 2.3% at 2A and to 3.6% at 0.5A. Considering that twice as many moles of hydrogen are produced as of oxygen, the impurity would result in 1.2% to 1.8%.

5.3.3.2 Trace gas analysis

The initial trace gas analysis has been performed with the box setup and the commercially sourced batteries. An intermittent charge/discharge program was applied to the batteries to monitor changes in mass detection from m=1 up to m=100 caused by the test program. The pattern for the evolution of hydrogen (m=2), oxygen (m=16,32 and 34), and water vapor (m=17,18) followed the test program. Detection was highest at the end of the charging cycle, decreasing during discharging and started to increase at the start of charge insertion. The relative concentration of argon decreases during evolution of oxygen and hydrogen, for that reason, the counts for associated masses (m=20,36,38,39,40) decrease as well, while the pattern for Argon was anticyclical compared to the other gasses.

The counts for CO_2 (m=44) also follow the charging pattern, while the masses m=12,14,15 and 28 did not indicate variations caused by the test program. Figure 5.32 depicts the test result for mass 44.

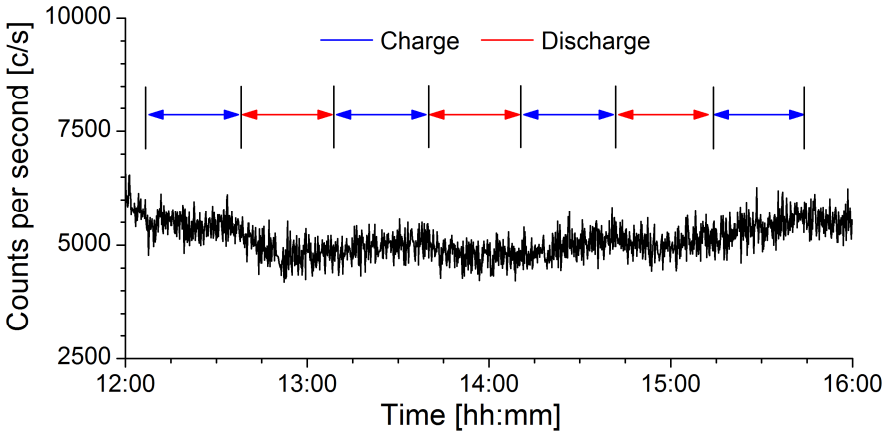

Figure 5.32: Counts detected for m=44 (CO_2) for an intermittent charge-discharge test program. A slight increase in counts towards the end of the charging steps is recognizable with a subsequent decrease in detected counts, test performed with commercial battery in box setup. A amount of around 5000 c/s is background related, only the variation between relative minima and maxima are cause by the test program.

The above result was obtained from measurements performed with commercial batteries in the box-setup. Additional tests were executed with the battolyzer to identify whether the counts for CO_2 originate from the Nickel electrode or from the Fe electrode. Figure 5.33 depicts the test results for CO_2. Furthermore it is indicated which electrode is tested together with the counts for the belonging main product gas.

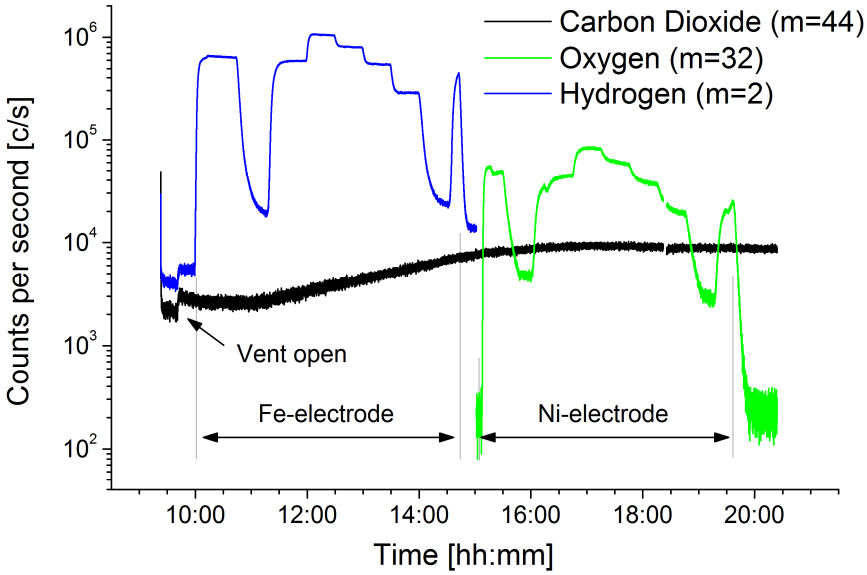

Figure 5.33: Counts detected for m=44 (CO_2) m=32(O_2) and m=2 (H_2). The last two are the main gasses produced at the Ni- electrode and the Fe- electrode respectively. The y-axis is on log-scale for scaling purpose.

The counts for m=44 show no deviation. Neither the applied program with charging, under various charge rate and discharging nor the connected compartment influence the progress of the curve. The moment of opening the vent to the RGA is visible in the beginning of the test as the counts for m=44 and =2 increase abruptly. Throughout the hole test program, Argon is used as a purge gas. The gas system detects this background flow when no electrode compartments are connected. The moments of connecting/disconnecting these compartments is recognizable in the abrupt

rise/decline of the specific counts for first H_2 and then O_2. At this specific moments no variations for CO_2 occur.

Now the question raises, why do we have fluctuations for m=44 when testing the batteries and not when testing the battolyzer? Both use the same electrodes, but both devices use a different electrolyte. The batteries work with commercial electrolyte while the electrolyte for the battolyzer is self-made. Charge rates can be excluded as reason as the battolyzer was charge at a higher rate (C/2.5) than the batteries (C/3.33).

The test-results for the other observed masses, m=12, m=14, m=15 and m=28 did not show any dependence on charge rate or state. Their measurement is not related to the battolyzer activity, but to the background of the RGA system.

5.3.3.3 Gas quantity

The quantitative gas measurements preformed with charged electrodes for both configurations ("up" and "down") are in agreement with computed values for temperature and pressure at the test time. The plunger's weight and setup-based loss factors are compensated for. Table 5.18 and Table 5.19 depict the test results. The ratio of computed to measured values is within 0.5%.

Table 5.18: Determined and computed inverse gas flow rates (sec/ml) for setup "up"

Setup "up" at	1 [A]	1.5 [A]	2 [A}
measured [sec/ml]	5.459	3.655	2.742
computed [sec/ml]	5.458	3.639	2.729
ratio	1.0	0.996	0.995

Table 5.19: Determined and computed inverse gas flow rates (sec/ml) for setup "down"

Setup "down" at	1 [A]	1.5 [A]	2 [A}
measured [sec/ml]	5.347	3.550	2.660
computed [sec/ml]	5.322	3.548	2.661
ratio	0.995	0.999	1.0

5.3.4 Summary

Combining the results from the quantitative and qualitative gas measurements leads to the conclusion that the coulombic efficiency for electrolysis must be close to 100%; the largest experimental deviation is 0.5%, which is a very small deviation. The quantitative gas measurements correlate, that all charge is used for gas production whereas the qualitative measurements show that no other gasses are produced. However, the origin of counts for m=44 is still unknown and requires further research.

Cycling experiments show that the battolyzer is functional as a battery, but that improvements are required with respect to ohmic losses, in order to reach the batteries efficiencies. Improvements of gas separation capabilities are also recommended. This could be achieved easily, considering that the membrane is clamped between flat surfaces but has no O-ring seal between the gas compartments. They are just held by two 1 mm thick PVC plates and small quantities of gas may still pass.

6 Discussion and Conclusions

This chapter provides discussion and conclusions about the battolyzer as a combined short-term and long-term energy storage device. The contribution of this thesis, limitations of the current work and suggestions for future work complete this thesis.

6.1 Discussion

First, the earlier-stated sub-questions are answered on the basis of the theoretical and experimental sections. This finally leads to conclusions and answering of the main research question.

Sub-question 1: What are the main components of Nickel-Iron batteries and alkaline electrolysis?

Nickel-Iron batteries and alkaline electrolyzers are electrochemical cells that operate with an alkaline electrolyte. The main components of the positive electrode of both devices are built up from nickel-compounds. Ni-Fe batteries use iron as negative electrode, alkaline electrolyzers use nickel based negative electrodes. A separator keeps the electrodes of Ni-Fe batteries apart to avoid short-circuiting. Electrolyzers are equipped with a membrane. The membrane separates the evolving gasses while it allows the hydroxyl ion transport required for the process.

Battery cells are arranged in a parallel configuration as this configuration allows a compact design. Electrolyzers are either built up in parallel configuration or in a bi-polar configuration, where the electrodes are connected in series. This bi-polar configuration normally requires additional care for the cell balancing, but has the advantages of simple design, low electrical resistance, and it allows gas separation under pressurized conditions.

The main components of Nickel-Iron batteries and alkaline electrolysis are: electrodes, separator/membrane, electrolyte, and the configuration-dependent components.

Sub-question 2: Can these components be used for a combined device or is it necessary to invent/assemble components?

At first the technical requirements for the combined device are defined:

- Resistant to KOH and NaOH at all concentrations
- Resistant to temperatures up to 50˚C
- Resistant to H_2 and O_2

The temperature requirement follows the maximum operating temperature for Ni-Fe batteries, as only these electrodes allow reversible operation (charging and discharging).

2.a: What is the best choice for the positive electrode?

Nickel-based battery electrodes are well established in different types of batteries, such as Nickel-Iron, Nickel-Cadmium, Nickel-Metal-hydride, Nickel-Zinc and Nickel-Hydrogen. Nickel-electrodes are characterized by a high cycle life, because the material hardly experiences any structural changes during charging and discharging. Nickel-Cadmium and Nickel-Hydrogen batteries are even used for space application because of their longevity. In Nickel-based batteries the β-$Ni(OH)_2$ phase spontaneously forms during discharge, as this is the most thermodynamically stable outcome at the pH and potentials used. This means that irrespectively of the history of charge/discharge/overcharge the material will always return to this phase.

Considering the relevant α,β,γ – Nickel based phase, batteries usually employ the β/β couple. It would be advantageous to utilize the α/γ couple as the difference in oxidation state increases. In other words, less active material is required for the same storage capacity. The γ- NiOOH forms upon overcharge and builds a pair together with the α- $Ni(OH)_2$ phase. However, the α-phase is not stable in alkaline electrolyte and alters back to the β-phase. As overcharging with the formation of γ- NiOOH is an essential operation principle of the battolyzer, further research of the α/γ couple could be advantageous.

NiOOH is one of the most active oxygen evolution catalysts. This catalyst forms automatically while charging the battery. Thus NiOOH becomes increasingly available when the battery becomes charged, and is fully available when required during overcharging.

The following remarks also concern sub-question 2.b:

Battery electrodes have traditionally been developed to increase overpotentials for gas evolution. Since gas evolution is now - in the battolyzer - a product, a whole new research field could evolve. Material combinations that were abandoned in the past, because they reduce overpotentials for gas evolution, could now be employed. New material combinations could also be tested. Research into the structure of electrodes is also required, as the structure has to have suitable gas transport properties in addition to ionic and electronic conductivity. The question is: which type of electrode - pocket type, plastic bond or sintered, will be best suited for these purposes. Tests with the pocket-electrodes were successful. Plastic bond electrodes are less stable than sintered ones, which are known to be the most stable and have the highest electrical conductivity.

The combination of excellent battery and catalytic properties makes Nickel the best choice for a positive electrode at this time. Improvements, building on this Nickel based material, may still be possible.

2.b: What is the best choice for the negative electrode?

Iron is an excellent choice for the negative electrode. The Ni-Fe combination has been known since its invention by Waldemar Jungner and Thomas Edison. The exceptional stability is related to the fact that both electrodes operate between the thermodynamically stable phases in their Pourbaix diagrams. Moreover, the stability window for the electrolyte matches well with the open-cell potential, which lies between the minimum equilibrium and the thermo-neutral potential window to electrolyze water. During charging, hydrogen production occurs simultaneously, no additional overpotential is required, except for to compensate entropy changes. This fact, the unwanted

hydrogen production, led to the near-extinction of this type of battery. However, it perfectly fits our purpose of having a combined battery and electrolyzer.

Currently, no other combination with a positive nickel electrode is possible for a large-scale energy storage application in the form of the battolyzer: overcharging has a detrimental effect on Nickel-Zinc and Nickel-metal-hydride batteries. Nickel-Hydrogen batteries use platinum as negative hydrogen electrode and hydrogen gas under pressure. This makes them suitable for space applications, but not for large-scale storage applications, because of the price and the scarcity of platinum. Nickel-Cadmium batteries are very robust and tolerate overcharging as Nickel-Iron batteries do. However, Nickel-Cadmium batteries were discarded as an option because of the toxicity of cadmium.

Apart from these considerations, no other configuration seems as energy efficient, due to the position of the redox potentials, and as economic as iron with its low costs.

Iron in combination with Nickel is an excellent choice for the negative electrode.

2.c: What is the best choice for the diaphragm?

Zirfon® Perl is a porous membrane that is considered state of the art for alkaline electrolyzers. Two types of Zirfon® Perl are available, type UTP 500 resists temperatures of up to 110˚C for continuous operation, and type LTP 550 can stand temperatures up to 70˚C. Both allow a maximum concentration of KOH or NaOH of 30wt%, so the type LPT 550 is sufficient.

Zirfon® Perl LPY 550 is an excellent choice for the diaphragm.

2.d: Which electrolyte should be used?

Ni-Fe batteries and alkaline electrolyzers both operate with potassium hydroxide as electrolyte. Only the concentrations of potassium hydroxide differ between these two applications. The electrolyte of Ni-Fe batteries additionally contains Lithium hydroxide.

The experiments show that the well established concentration of 21wt% KOH is the best concentration for operating the battolyzer. However, the possibility of increasing the concentration should not be discarded as electrolysis potentials are lower for higher concentrations. From the viewpoint of efficiency, especially with high charge insertion, LiOH should not be used as an additive.

The effects of not adding LiOH to the electrolyte on the longevity of the cells have not been studied. Based on my research so far, no statements are possible about this issue. However, nickel-cadmium batteries utilize pure KOH as electrolyte, so the effect of omitting LiOH on the nickel-electrode should be limited.

The well-established concentration of 21wt% KOH should be used for the battolyzer.

Answering sub-questions 2.a-d leads to the answer of sub-question 2:

Iron in combination with Nickel is an excellent choice for the battolyzer, together with Zirfon® Perl LPY 550 and the well-established concentration of 21wt% KOH for the electrolyte. Improvements building on these materials may still be possible.

Sub-question 3: Does the concept of the battolyzer work?

3.a: Do the electrodes withstand severe overcharging?

The test-series that were designed to simulate various real-life situations, including partial and full charging and discharging, rapid switching, continuous overcharging, and the around-the-clock cycling, has by now been operational for over a year. Nearly 8000Ah of charge were inserted to single cells, 800 times the nominal cell capacity. 3200 Ah were used for water splitting, 320 times the nominal cell capacity. Neither the battery, nor the electrolysis have noticeably deteriorated after the many cycles that include battery overcharges of up to 6 times the nominal capacity, rapid current reversals, and deep discharges for each cycle. The remarkable finding is that the reversible discharge capacity of the battery is not adversely affected by such harsh test conditions.

Yes, the electrodes withstand severe overcharging.

3.b: Does overcharging lead to gas production?

Hydrogen evolution starts immediately at small rates upon charge insertion, while the onset for oxygen evolution is delayed. The oxygen evolution catches up later and surpasses hydrogen evolution. Overall, stoichiometric gas evolution takes place, and the gas production scales with the charge rate. During discharge, a fast decrease of gas evolution towards zero is observed. This is in line with earlier gas measurements of Ni-Fe batteries that were performed to characterize the composition of the produced gas to evaluate explosion risk [51]. Interestingly, the gas evolution is not constant during electrolysis. Increasing device temperature promotes self-discharge and electrolysis. Both processes lead to increased gas yield and reduced discharge capacity.

Intermittent charge and discharge show that hydrogen evolution starts immediately, while oxygen evolution is delayed, but catches up again when the nickel electrode becomes charged (NiOOH). NiOOH is clearly the more active oxygen evolution catalyst. Interestingly, after onset of oxygen evolution, oxygen evolution starts immediately in subsequent sub-cycles. Partial discharge does not lead to delays anymore, but just to a drop in magnitude of oxygen evolution. Thus, NiOOH is in contact with the electrolyte and enables water splitting.

During the test period, cell C2 consumed 1073.6 g of water, of which 1038.7 g (96.7%) was expected from electrolysis. The remainder was lost through evaporation via the exhaust valves, together with the gas release. Since the cell contains around 70 ml electrolyte, the contents have been replaced over 15 times, only demineralized water was added. The additional water consumption increases with test temperature and charge rate. This close agreement indicates that all overcharge contributes to water splitting and gas production.

Yes, overcharging leads to gas production.

3.c: Do side reactions occur?

The amount of evolving gasses has been determined volumetrically. The quantitative gas measurements correlate with the theoretical amount of evolving gasses. The measurements support the conclusion that all inserted charge is used for gas production. The high conversion efficiency indicates that there is hardly any room for side reactions.

Trace gas analysis performed with the battolyzer further indicates that no side-reactions occur. However, trace gas analysis performed with the commercial batteries indicates a very small amount of CO_2 production.

The reason for the detection of CO_2 is still unclear. Trace gas analysis with the battolyzer was performed at a lower temperature than trace gas analysis performed with the commercial batteries. This fact could indicated a thermally activated process.

The electrolyte composition could also cause CO_2 detection. The electrolyte for the battolyzer was self-made with demineralized water. The exposure time to the atmosphere was limited. Thus, the electrolyte hardly contains any carbonate. The commercially-supplied electrolyte contains carbonates. Carbonates form, together with sodium and potassium, salts in alkaline environment. These salts are white and visible in the electrolyte. Actually, ICP did not detect these salts, as solids are filtered out before testing. Literature indicates (that carbonate converts to small amounts of bicarbonate, and) that sodium-bicarbonate electrolyzes to, among others, CO_2 during electrolysis in a aqueous solution [52]. Replacing supplied electrolyte with self-made electrolyte could verify this hypothesis and explain CO_2 detection.

The high conversion efficiency indicates that there is hardly any room for side reactions. However, side-reactions cannot be ruled out for 100%.

3.d: Is the system efficient and what factors influence the efficiency?

The most remarkable finding of the whole project is the stability of the energetic efficiency at 80-90% over many different types of cycles. The usual suspects - charge and discharge rate, operation temperature, and electrolyte composition - determine the efficiency. Moreover, the state of discharge influences the efficiency, avoiding less efficient full discharge is beneficial.

Charge and discharge rate influence overpotentials. Ohmic losses generate the main losses in the battolyzer. Activation overpotentials dictate the battery and electrolysis related losses. Figure 6.1 reprints Figure 5.13, as a "Tafel plot". Furthermore, voltage dependent efficiency limits are added to the figure.

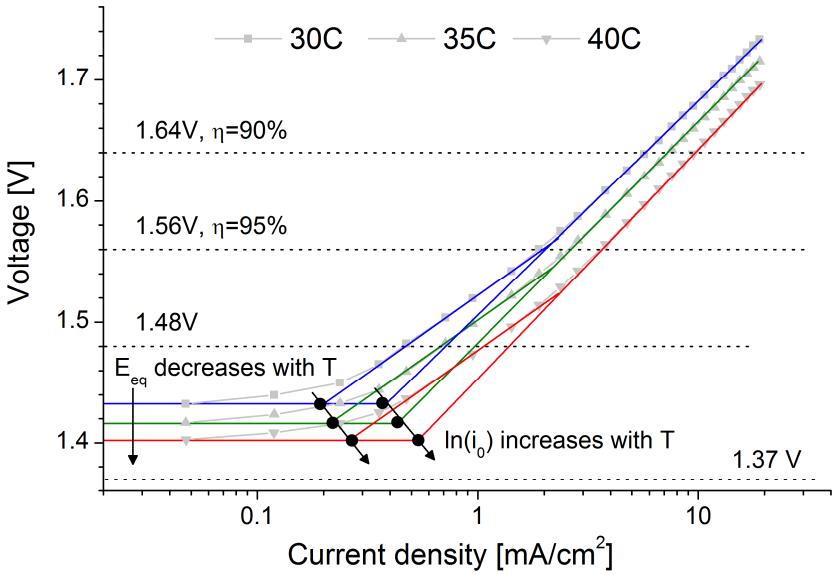

Figure 6.1: Electrolysis potential dependence on applied current density for several temperatures (cell C1).

The overpotentials increase with increasing current and decrease with increasing temperature. For low currents the overpotentials are zero, the equilibrium potentials can be read from the graphs. These potentials decrease with increasing temperature. At high overpotentials two linear regions can be distinguished, indicating two processes. (At the current stage no statement is possible as to which region belongs to which process.) The slope of these sections is proportional to the overpotentials. The intersection of these lines with their respective equilibrium potentials displays the exchange current density (i_0). The exchange current density increases with increasing temperature, improving the kinetics of the electrode. No mass transport limitations have been identified for the applied currents, since the slope progresses linearly at high currents. Increasing the cell temperature has two effects, decreasing equilibrium potential and increasing exchange current density. Both effects improve cell operation.

The applied electrolyte compositions affect the cell efficiency less than temperature variations do. While the electrolyte conductivity hardly changes within a concentration range from 20wt% to 30wt% KOH, the electrolyte conductivity increases by 25 % when increasing the operating temperature from 25˚C to 40˚C.

From the above remarks, I conclude that increasing operating temperature is beneficial. Hence, further research should focus on finding the maximum operation temperature for the Ni-Fe system. Based on Thomas Edison, who limited the operation temperature for his batteries to 45˚C, this research limited the maximum test temperature to 40˚C. The manual of the tested cell defines the maximum cell temperature as 60˚C, but increasing the operating temperature should be possible.

Increasing temperature increases the conductivity of the electrolyte and the solubility of $HFeO_2^-$, the dissolute intermediate for charging the iron electrode. Both improve cell operation. Interestingly, increasing the temperature hardly influences the discharge process.

The system currently has an energetic efficiency of 80-90%. Temperature, as well as charge and discharge rate, influence the efficiency. The electrolyte composition has a minor influence. Operating the cell at 40˚C and moderate rates leads to efficiencies of around 90%. Avoiding less-efficient full discharge further increases the system's performance.

Answering sub-questions 3.a-d leads to the answer of sub-question 3:

Yes, the concept of the battolyzer works!

Sub-question 4: How can the system be classified compared to state-of-the art alkaline electrolyzers and batteries?

State-of-the-art alkaline electrolyzers operate at a current density up to 400mA/cm² and at pressures up to 30 bar [30]. The cell potential for these conditions is 2.4V [29]. The battolyzer operates at atmospheric pressure and a maximum current density up to 20mA/cm². (This limit is because of limitations of the test equipment). Figure 6.1 shows that the potential for electrolysis at 40˚C increases with 0.18V when increasing the current by a factor 10. The potential associated with for a current density of 20mA/cm² is 1.69V at 40˚C. Increasing the current density to 200mA/cm², and assuming no mass transfer losses, would result in potential of 1.87V and an efficiency of 79%. The process would still be highly efficient compared to an alkaline electrolyzer operating at well above 2V. Operation at high pressure is worthwhile, as compressing the initial liquid electrolyte costs much less energy than compressing the produced gasses. Actually, there are no objections to increasing the operation pressure and the current density of the battolyzer. It would only be a matter of making the efforts to develop a suitable pressurized configuration.

Compared to polymer membrane electrolyzers (PEM), the battolyzer uses only low cost materials and no noble metals such as Pt, and still reaches high efficiency and good switching capabilities.

It is likely that the thickness of electrodes has to increase to match the charge rate of the battery to the desirable current densities of the electrolyzer. The active surface area of new electrodes will always exceed the active surface area of electrodes of the alkaline electrolyzer. Increasing the surface area will benefit the electrolysis efficiency, since the current density will decrease. This electrode design issue goes along with the remarks concerning the structure of the electrode (see sub-question 2.a)

Lithium-ion batteries and Sodium-Sulfur batteries have the highest round-trip efficiency [53]. Therefore comparison is limited to these two battery types. Lithium ion batteries have an efficiency of up to 90 %, Sodium-sulfur batteries of up to 80%. The efficiency of the battolyzer was stable and always above 80%. For an operation temperature of 40˚C the efficiencies are always above 85%, even at high charge rates.

The advantage of the battolyzer compared to these batteries is not efficiency-related. The battolyzer operates with an aqueous electrolyte without any concerns about toxicity. Lithium-ion batteries operate with an organic electrolyte, while sodium sulfur batteries work at high temperatures with molten sodium and sulfur and alumina electrolyte. Organic electrolytes can be characterized as expensive, toxic and highly flammable. The same holds for sodium-sulfur batteries as SOx is poisonous and liquid sodium is highly flammable. Processing and cell technology determine the costs for energy storage systems. Unlike Lithium-ion batteries and Sodium-Sulfur batteries, the battolyzer requires no air-free or dry room processing, or expensive electrolytes and electrodes. In the case of the battolyzer, the Fe and Ni based compounds are relatively simple hydroxides, which are low cost and earth abundant.

Last but not least, Ni-Fe battery electrodes already have a proven longevity, which makes their economic lifetime much longer than lithium and sodium batteries.

The operating conditions of the battolyzer have to improve to reach operational conditions - high pressure and high current density - of state-of-the-art alkaline electrolyzers. The battolyzer operates with a higher efficiency at the current operating conditions, and has the potential for highly efficient operation at conditions comparable with current high power electrolysis.

The battolyzer can be classified as more efficient than Sodium-Sulfur batteries, and as equally efficient as Lithium-ion batteries. The battolyzer clearly has advantages relative to Lithium-ion and Sodium-Sulfur batteries in the realms of processing, safety, and longevity.

However, the main advantage compared to batteries and electrolyzers is that you get both functions - electrical energy storage and electrolytic water splitting - in one device!

6.2 Conclusions

Finally, the main research question will be answered:

Is an energy storage system based on Nickel and Iron suitable to operate as an integrated battery and electrolyzer, and what would be the overall energy efficiency of such a device?

Yes, an energy storage system based on Nickel and Iron is suitable to operate as an integrated battery and electrolyzer.

The synergy of this combination of materials is most noticeable when looking at the energy efficiency of up to 90 % for the combined device. On top of the battolyzer's excellent efficiency, where other types of batteries are limited by their capacity, the battolyzer is not. The battolyzer overcomes this restriction, which makes the device flexible with respect to energy insertion. A multiple of its capacity can be inserted to efficiently convert excess renewable energy into hydrogen and oxygen. The battolyzer is either charging and/or producing hydrogen and oxygen, or discharging when no excess energy is available. This concept will lead to a high capacity factor.

As a storage alternative, a battery could be combined with an electrolyzer. As at least alkaline electrolysis requires continuous operation, backup battery power is necessary at times when no excess energy is available, thus the overall efficiency of two separate devices will be lower.

For up-scaling purposes, cells can be arranged in serial configurations. In practice, the cells will not be fully identical. In serial configuration, the differences in capacity normally play an important role in the battery management system. When the first cell is full, but charging continues, this cell will start overcharging, i.e. electrolysis is the main reaction. The battolyzer inherently deals with the overcharging, which is unlike any other battery type. For example, for Lithium-ion batteries or Nickel-metal-hydride batteries this is an unwanted, and even dangerous, situation. An uncomplicated management system is feasible for the battolyzer.

So far, a lot of data has been presented on performance characteristics, but what would be an appropriate starting point for a real large-scale energy storage device? What would be constraints?

One could argue, that such a device should be able to provide energy for at least one day without solar energy generation, therefore backup is required for two nights and one day, approximately 40 hours. Assuming uniform energy consumption, the maximum discharge rate would be C/40. Hence, handling a C/40 discharge rate seems a appropriate starting point for a future cell design. In a renewable energy future, similar daily volumes of electricity storage in batteries and in hydrogen fuels may be required to achieve adequate energy storage on both daily and seasonal timescales [1]. Assuming 10 hours of charging and 14 of hours discharging per day leads to charging rates of about C/10, four times higher than the discharge rate, to fulfill the production constraints. The estimated rates for such a large-scale device are about 2-4 times lower than the test conditions. Final tests at these test conditions result in efficiencies of 90.4% for a complete cycle and 91.8% for a sub-cycle. The energy efficiency of a real device could therefore be above 90%.

The overall energy efficiency of the battolyzer in practical applications could surpass 90%.

6.2.1 Contribution of this thesis

This thesis has developed and explored a prototype energy storage system based on Nickel and Iron to operate as a battery and electrolyzer as one combined device. The battolyzer was based on the Nickel-Iron-Battery, which was developed by Thomas Edison and Waldemar Jungner, and on alkaline electrolysis. Both are well-established technologies that were developed more than a century ago. This thesis shows that it is possible to merge these technologies.

The robust Nickel-Iron based energy storage-system, is not only suitable as an integrated battery and electrolyzer, but the combined system also has an impressive overall energy efficiency of up to 90% at the current state, and has the potential to surpass this limit.

We anticipate these results to be a starting point for a robust grid-scale energy storage solution in a low-cost, abundant-element based, intrinsically flexible device that has close to full-time operability: as electrical power storage, switchable electricity supply and as a hydrogen producer.

6.3 Limitations of the current work and future work

6.3.1 Limitations of the current work

Successful tests were executed for over a year. Predictions concerning life-time are based on experience with Ni-Fe batteries and alkaline electrolysis, not on experimental results.

6.3.2 Future work

Remarks concerning future work are placed throughout the thesis. The following summary lists all suggestions for further research:

- Tests with a three electrode configuration to determine the specific electrode potentials for charging, discharging, and electrolysis at various temperatures.
- Tests at temperatures above 40˚C.
- Trace gas analysis with commercial batteries using self-made electrolyte.
- Trace gas analysis at elevated temperatures.
- Tests at higher currents (beyond limitations of our current test-equipment).
- Gas analysis of battolyzer after improvement of the mechanical separation of its gas compartments.
- Search the literature for new electrode materials, to improve catalytic properties of the electrodes.
- Self-assembly of thicker electrodes.
- Design of a pressurized battolyzer cell, preferably in a bi-polar setup.

Finally I would like to propose the following research question:

"Does successive overcharging and/or discharging decrease the concentration of $HFeO_2^-$ and FeO^{2-}?"

The hypothesis is that overcharging and/or discharging leads to the decrease of the concentrations of $HFeO_2^-$ and of FeO^{2-}, as these dissolute intermediates will re-deposit on the iron electrode. Since the dissolution of iron occurs at higher temperatures, this effect could counteract iron dissolution. This would allow higher operation temperatures for the battolyzer and would benefit its longevity.

Bibliography

[1] Mulder, F.M., *Implications of diurnal and seasonal variations in renewable energy generation for large scale energy storage.* Journal of Renewable and Sustainable Energy, 2014. **6**: p. 033105.

[2] Falk, S.U. and A.J. Salkind, *Alkaline Storage Batteries*. 1969, New York: J. Wiley & Sons.

[3] Linden, D. and T.B. Reddy, *Handbook of Batteries Third Edition*. 2001: McGraw-Hill.

[4] DeMar, P.J. *Nickel-Iron*. in *Telecommunications Energy Conference (INTELEC), 2011 IEEE 33rd International*. 2011.

[5] Kinzelbach, R., *Stahlakkumulatoren*. Vol. Band 3. 1974, Hannover: VARTA Batterie AG.

[6] Shukla, A.K., M.K. Ravikumar, and T.S. Balasubramanian, *Nickel/iron batteries.* Journal of Power Sources, 1994. **51**(1–2): p. 29-36.

[7] Huggins, R., *Advanced batteries: materials science aspects*. 2008: Springer Science & Business Media.

[8] Halpert, G., *Past developments and the future of nickel electrode cell technology.* Journal of Power Sources, 1984. **12**(3–4): p. 177-192.

[9] Tsais, P.J. and L.I. Chan, *11 - Nickel-based batteries: materials and chemistry*, in *Electricity Transmission, Distribution and Storage Systems*, Z. Melhem, Editor. 2013, Woodhead Publishing. p. 309-397.

[10] Ravikumar, M.K., T.S. Balasubramanian, and A.K. Shukla, *A nickel-iron battery with roll-compacted iron electrodes.* Journal of Power Sources, 1995. **56**(2): p. 209-212.

[11] Periasamy, P., B. Ramesh Babu, and S. Venkatakrishna Iyer, *Performance characterization of sintered iron electrodes in nickel/iron alkaline batteries.* Journal of Power Sources, 1996. **62**(1): p. 9-14.

[12] Ravikumar, M.K., T.S. Balasubramanian, A.K. Shukla, and S. Venugopalan, *A cyclic voltammetric study on the electrocatalysis of alkaline iron-electrode reactions.* Journal of Applied Electrochemistry, 1996. **26**(11): p. 1111-1115.

[13] Bryant, W.A., *The structure and performance of sintered iron electrodes.* Electrochimica Acta, 1979. **24**(10): p. 1057-1060.

[14] Öjefors, L. and L. Carlsson, *An iron—air vehicle battery.* Journal of Power Sources, 1978. **2**(3): p. 287-296.

[15] Öjefors, L., *Self-discharge of the alkaline iron electrode.* Electrochimica Acta, 1976. **21**(4): p. 263-266.

[16] Andersson, B. and L. Ojefors, *SLOW POTENTIODYNAMIC STUDIES OF POROUS ALKALINE IRON ELECTRODES.* Journal of the Electrochemical Society, 1976. **123**(6): p. 824-828.

[17] Ojefors, L., *TEMPERATURE DEPENDENCE OF IRON AND CADMIUM ALKALINE ELECTRODES.* Journal of the Electrochemical Society, 1976. **123**(8): p. 1139-1144.

[18] Souza, C.A.C., I.A. Carlos, M. Lopes, G.A. Finazzi, and M.R.H. de Almeida, *Self-discharge of Fe–Ni alkaline batteries.* Journal of Power Sources, 2004. **132**(1–2): p. 288-290.

[19] Malkhandi, S., B. Yang, A.K. Manohar, G.K.S. Prakash, and S.R. Narayanan, *Self-assembled monolayers of n-alkanethiols suppress hydrogen evolution and increase the efficiency of rechargeable iron battery electrodes.* Journal of the American Chemical Society, 2013. **135**(1): p. 347-353.

[20] Gil Posada, J.O. and P.J. Hall, *Multivariate investigation of parameters in the development and improvement of NiFe cells.* Journal of Power Sources, 2014. **262**(0): p. 263-269.

[21] Gil Posada, J.O. and P.J. Hall, *Post-hoc comparisons among iron electrode formulations based on bismuth, bismuth sulphide, iron sulphide, and potassium sulphide under strong alkaline conditions.* Journal of Power Sources, 2014. **268**(0): p. 810-815.

[22] Manohar, A.K., C. Yang, S. Malkhandi, G.K.S. Prakash, and S.R. Narayanan, *Enhancing the performance of the rechargeable iron electrode in alkaline batteries with bismuth oxide and iron sulfide additives.* Journal of the Electrochemical Society, 2013. **160**(11): p. A2078-A2084.

[23] Wang, H., Y. Liang, M. Gong, Y. Li, W. Chang, T. Mefford, J. Zhou, J. Wang, T. Regier, F. Wei, and H. Dai, *An ultrafast nickel–iron battery from strongly coupled inorganic nanoparticle/nanocarbon hybrid materials.* Nat Commun, 2012. **3**: p. 917.

[24] Gong, M., W. Zhou, M.-C. Tsai, J. Zhou, M. Guan, M.-C. Lin, B. Zhang, Y. Hu, D.-Y. Wang, J. Yang, S.J. Pennycook, B.-J. Hwang, and H. Dai, *Nanoscale nickel oxide/nickel heterostructures for active hydrogen evolution electrocatalysis.* Nat Commun, 2014. **5**.

[25] Hariprakash, B., S.K. Martha, M.S. Hegde, and A.K. Shukla, *A sealed, starved-electrolyte nickel–iron battery.* Journal of Applied Electrochemistry, 2005. **35**(1): p. 27-32.

[26] *Changhong NF-S Series Nickel-Iron batteries for solar PV applications*. [Accessed: 1-12-2014]; Available from: http://www.changhongbatteries.com/Nickel-Iron(Ni-Fe)_c13_m2.2.1.html.

[27] *Alkaline Nickel-Cadmium and Nickel-Iron Cells and Batteries*. [Access: 01-12-2014]; Available from: http://nickelcells.com/pdf/manuf/Kursk.pdf.

[28] Bat, U. [cited 2014 1-12-2014]; Available from: http://ukrbat.com/en/.

[29] Carmo, M., D.L. Fritz, J. Mergel, and D. Stolten, *A comprehensive review on PEM water electrolysis.* International Journal of Hydrogen Energy, 2013. **38**(12): p. 4901-4934.

[30] Guillet, N. and P. Millet, *Alkaline Water Electrolysis*, in *Hydrogen Production*. 2015, Wiley-VCH Verlag GmbH & Co. KGaA. p. 117-166.

[31] *Separator Membranes*. [Accessed 27-11-2015]; Available from: http://www.agfa.com/sp/global/en/internet/main/solutions/membranes/index.jsp.

[32] *Polymeric separators for electrolysis*. [Accessed: 30-11-2015]; Available from: https://vito.be/en/chemistry/membranes-and-electrodes/polymeric-separators-for-electrolysis.

[33] Pérez-Alonso, F.J., C. Adán, S. Rojas, M.A. Peña, and J.L.G. Fierro, *Ni/Fe electrodes prepared by electrodeposition method over different substrates for oxygen evolution reaction in alkaline medium.* International Journal of Hydrogen Energy, 2014. **39**(10): p. 5204-5212.

[34] Subbaraman, R., D. Tripkovic, K.-C. Chang, D. Strmcnik, A.P. Paulikas, P. Hirunsit, M. Chan, J. Greeley, V. Stamenkovic, and N.M. Markovic, *Trends in activity for the water electrolyser reactions on 3d M(Ni,Co,Fe,Mn) hydr(oxy)oxide catalysts.* Nat Mater, 2012. **11**(6): p. 550-557.

[35] Gupta, R.B., *Hydrogen fuel: production, transport, and storage*. 2008: CRC Press.

[36] Winston, R., *Uhlig's corrosion handbook, Second edition*. Other Information: Also available at www.pubs.asce.org; PBD: 2000. 2000. Medium: X; Size: 1312 pages.

[37] Vijayamohanan, K., T.S. Balasubramanian, and A.K. Shukla, *Rechargeable alkaline iron electrodes.* Journal of Power Sources, 1991. **34**(3): p. 269-285.

[38] Génin, J.M.R., A.A. Olowe, P. Refait, and L. Simon, *On the stoichiometry and pourbaix diagram of Fe(II)-Fe(III) hydroxy-sulphate or sulphate-containing green rust 2: An electrochemical and Mössbauer spectroscopy study.* Corrosion Science, 1996. **38**(10): p. 1751-1762.

[39] Beverskog, B. and I. Puigdomenech, *Revised pourbaix diagrams for iron at 25–300 ℃.* Corrosion Science, 1996. **38**(12): p. 2121-2135.

[40] Demidov, A.I. and E.N. Volkova, *Potential-pH diagram for the nickel-water system containing nickel(III) metahydroxide.* Russian Journal of Applied Chemistry, 2009. **82**(8): p. 1498-1500.

[41] Gilliam, R.J., J.W. Graydon, D.W. Kirk, and S.J. Thorpe, *A review of specific conductivities of potassium hydroxide solutions for various concentrations and temperatures.* International Journal of Hydrogen Energy, 2007. **32**(3): p. 359-364.

[42] *Installation and maintenance manual of Changhong solar PV NI-Iron storage cell NF-S*. [Access: 22-10-2015]; Available from: http://www.nickelcells.com/pdf/manuf/Ni-Fe%20NF-S%20user%20manual.pdf.

[43] *Electrolyte Mixing*. [Accessed: 27-11-2015]; Available from: https://ironedison.com/images/products/Iron%20Edison/Iron%20Edison%20Battery%20Company%20-%20Mixing%20guide%202012.pdf.

[44] Handbook, F.C., *EG&G technical services.* Inc., Albuquerque, NM, DOE/NETL-2004/1206, 2004.

[45] *Accumulator*. [Accessed: 27-11-2015]; Available from: http://www.nickelcells.com/pdf/manuf/Kursk.pdf.

[46] Micka, K. and Z. Zábranský, *Study of iron oxide electrodes in an alkaline electrolyte.* Journal of Power Sources, 1987. **19**(4): p. 315-323.

[47] Ogg, R.G., P. Bennett, A. Seidel, and P. Gifford, *Electrolyte for a nickel-iron battery*. 2014, Google Patents.

[48] *Kinetics of Activation Polarization*, in *Electrochemistry and Corrosion Science*, N. Perez, Editor. 2004, Springer US: Boston, MA. p. 71-120.

[49] *3F-PIC*. [Accessed 27-11-2015]; Available from: http://www.hidenanalytical.com/en/products/for-catalysis-and-thermal-analysis/catalysis-3f-pic-for-fast-event-uhv-studies.

[50] Akerlof, G. and P. Bender, *The density of aqueous solutions of potassium hydroxide.* Journal of the American Chemical Society, 1941. **63**(4): p. 1085-1088.

[51] Saltat, R.C., *Nickel-iron battery system safety*. 1984, Eagle-Pichler Industries, Inc.: NASA STI.

[52] Shipley, J.W., *THE EVOLUTION OF CARBON DIOXIDE IN THE A.-C. ELECTROLYSIS OF SODIUM CARBONATE AND BICARBONATE SOLUTIONS, AND THE DISCHARGE POTENTIALS OF CARBONATE AND BICARBONATE IONS.* Canadian Journal of Research, 1934. **11**(4): p. 539-546.

[53] Pellow, M.A., C.J. Emmott, C.J. Barnhart, and S.M. Benson, *Hydrogen or batteries for grid storage? A net energy analysis.* Energy & Environmental Science, 2015. **8**(7): p. 1938-1952.

[54] Mills, A.F., *Heat Transfer Second Edition*. 1999, Upper Saddle River, NJ 07458: Prentice Hall, Inc.

List of figures

List of tables

Appendix A - Results SEM/EDS

A.1. Nickel electrode activated and discharged

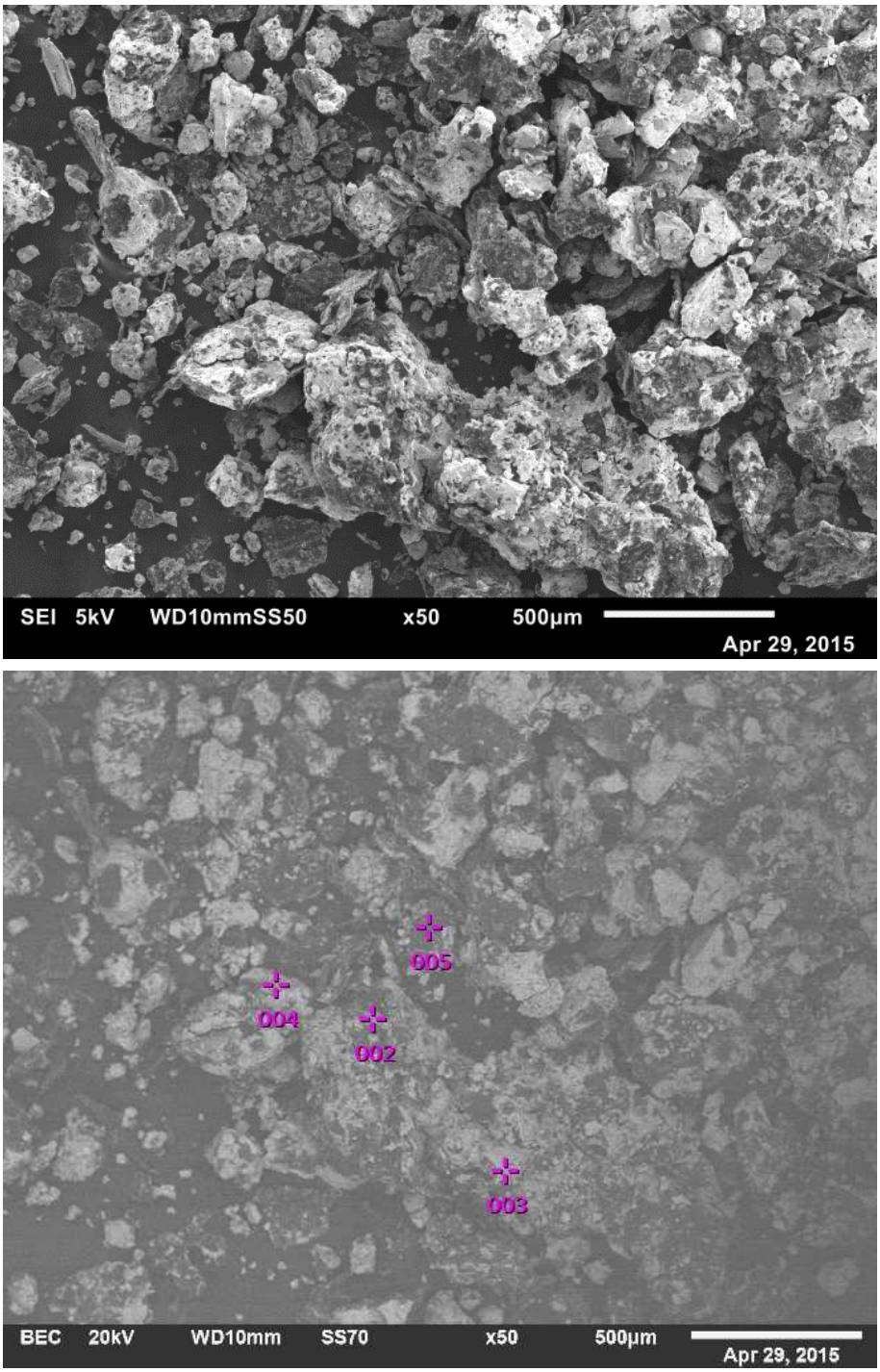

Figure A 1: SEI and BEC image of the material of the activated and discharge Ni-electrode. The marked point display the locations for point analysis.

Table A 1: Nickel electrode, Overall EDS result:

Chemical formula	mass%	Atom%	Sigma	Net	K ratio	Line
C	59.07	73.81	0.02	3E+05	0.0068919	K
O	21.55	20.21	0.05	84221	0.0071569	K
Na	1.68	1.10	0.02	25335	0.0011466	K
K	2.83	1.09	0.02	91986	0.0043456	K
Co	2.66	0.68	0.02	27545	0.0035342	K
Ni	12.21	3.12	0.05	1E+05	0.0167760	K
Total	100.00	100.00				

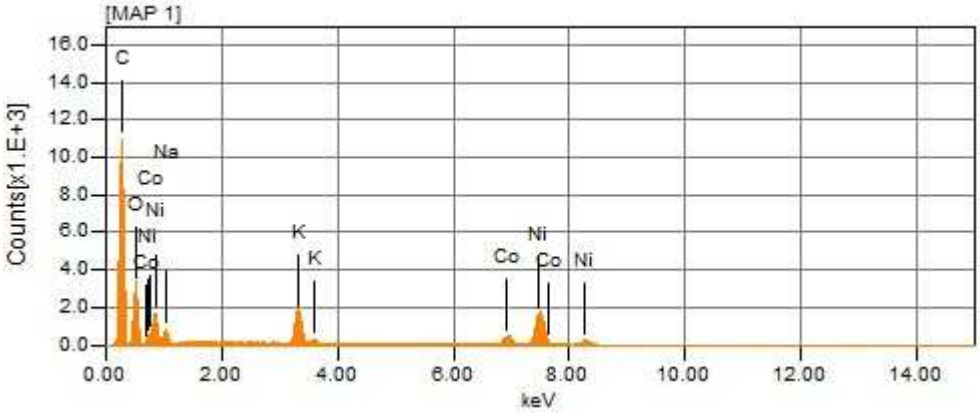

Table A 2: Nickel electrode, EDS result for point 002:

Chemical formula	mass%	Atom%	Sigma	Net	K ratio	Line
C	20.22	32.29	0.05	9783	0.0040108	K
O	46.27	55.48	0.15	45896	0.0639005	K
K	8.02	3.93	0.07	35307	0.0273277	K
Co	25.49	8.30	0.17	36653	0.0770501	K
Total	100.00	100.00				

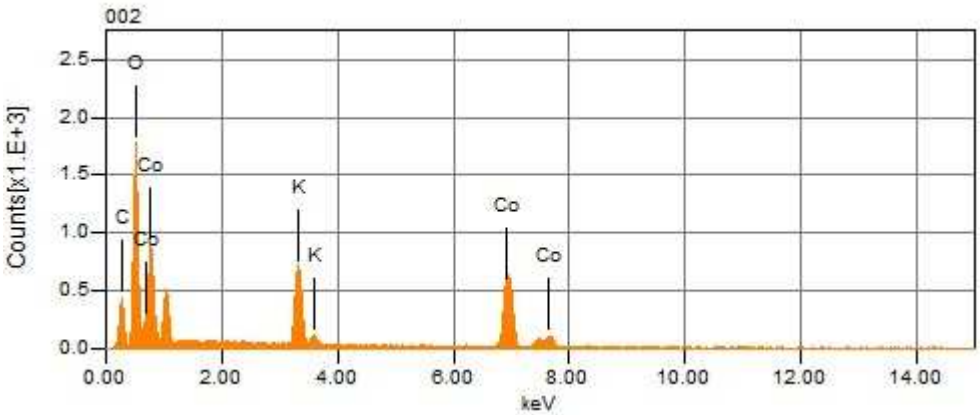

Table A 3: Nickel electrode, EDS result for point 003:

Chemical element	mass%	Atom%	Sigma	Net	K ratio	Line
K	13.98	19.61	0.22	9914	0.0076732	K
Co*	6.70	6.24	0.28	1737	0.0036516	K
Ni	79.32	74.14	0.76	17986	0.0451008	K
Total	100.00	100.00				

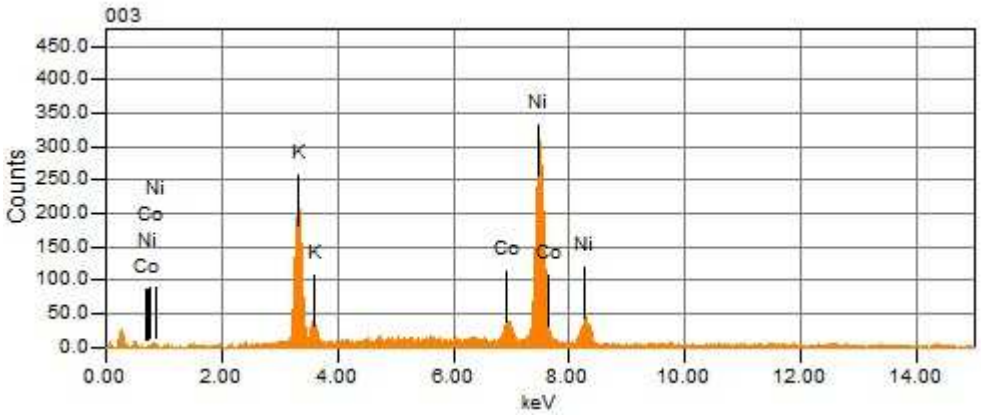

Table A 4: Nickel electrode, EDS result for point 004:

Chemical element	mass%	Atom%	Sigma	Net	K ratio	Line
C	29.88	44.46	0.05	16527	0.0067755	K
O	39.58	44.22	0.13	42493	0.0591619	K
Na*	2.89	2.24	0.06	5829	0.0043220	K
K	4.28	1.96	0.05	22736	0.0175980	K
Co*	4.97	1.51	0.08	8672	0.0182290	K
Ni	18.40	5.60	0.15	27876	0.0699011	K
Total	100.00	100.00				

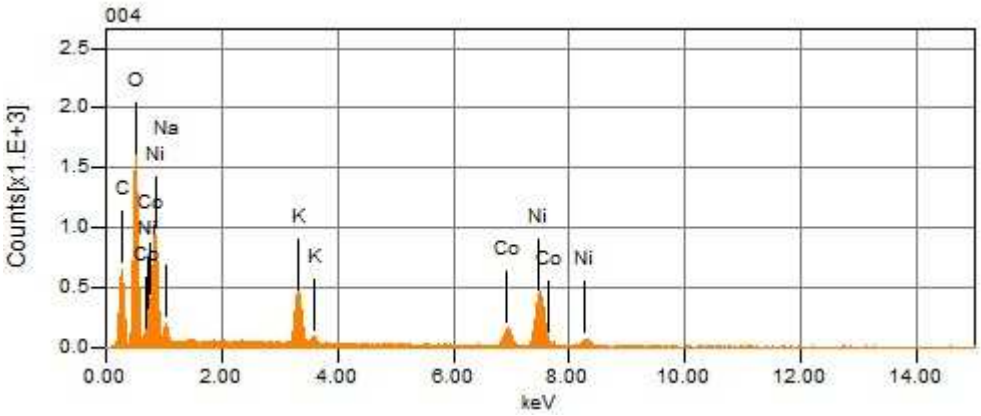

Table A 5: Nickel electrode, EDS result for point 005:

Chemical formula	mass%	Atom%	Sigma	Net	K ratio	Line
C	93.52	95.70	0.05	160383	0.0657509	K
O	5.26	4.04	0.09	2251	0.0031347	K
Co	0.52	0.11	0.03	937	0.0019691	K
Ni	0.69	0.14	0.04	1058	0.0026534	K
Total	100.00	100.00				

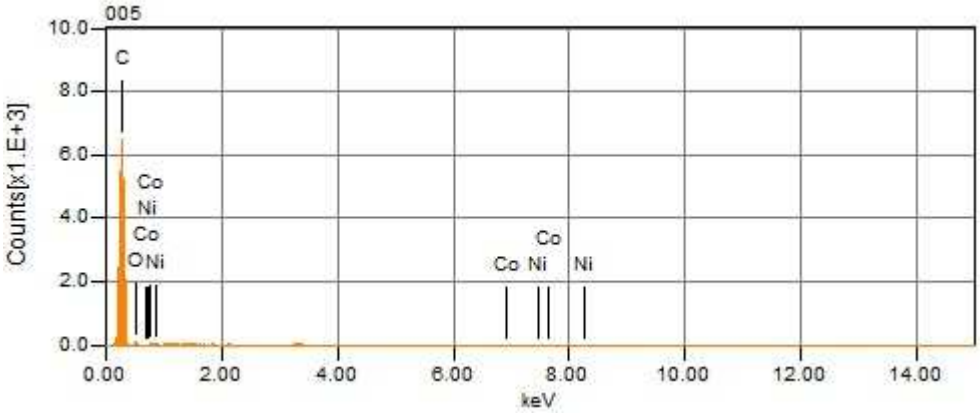

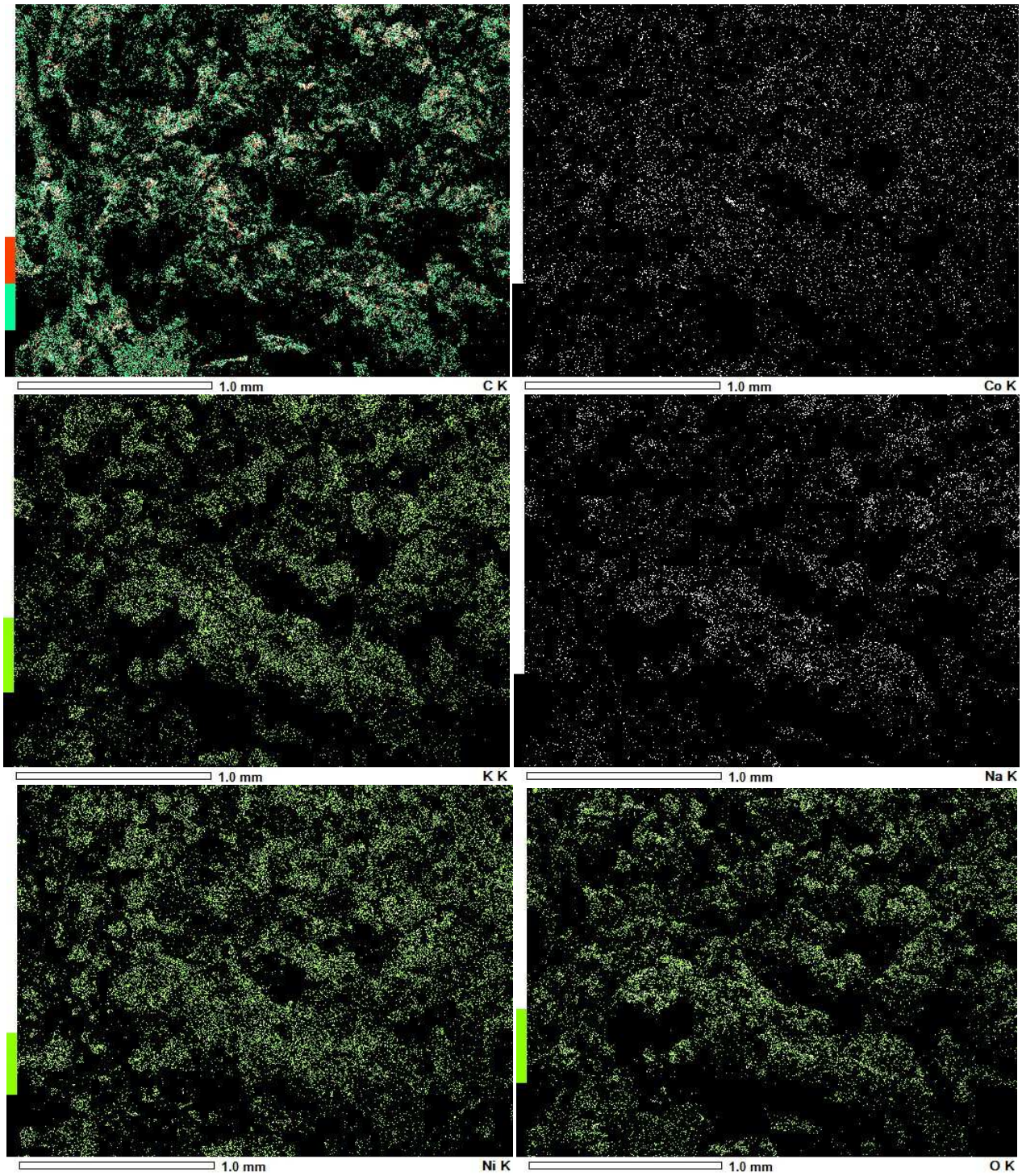

Figure A 2: Mapping image of chemical elements of the activated and discharge Ni-electrode; top left: Carbon, top right Cobalt; middle left Potassium; middle right: Sodium; bottom left: Nickel, bottom right: oxygen

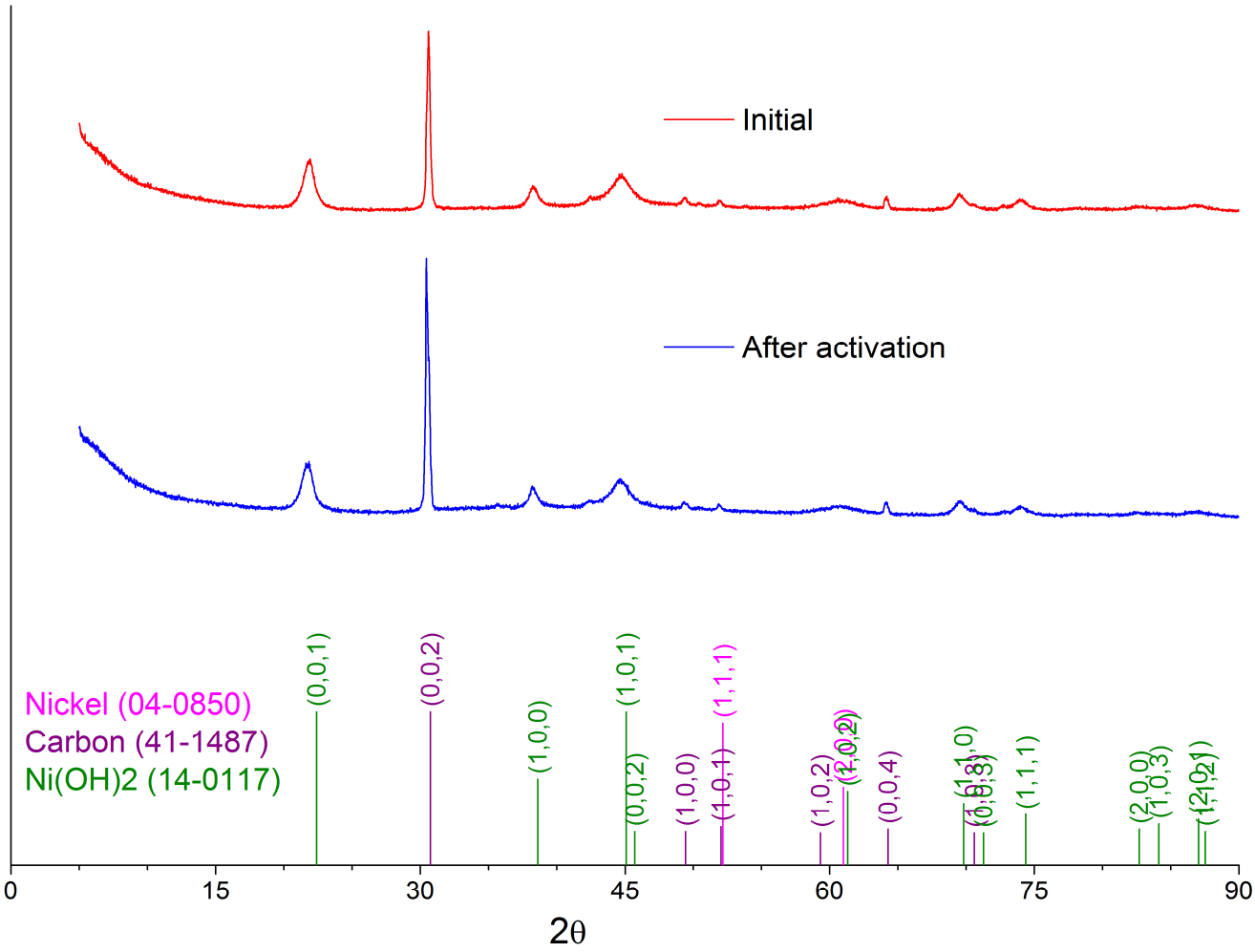

Figure A 3: XRD raw data of new and of activated Nickel electrode, wavelength 1.78897. For the sake of clarity, Cobalt and Cobalthydroxide are not added to the data. Their peaks are close to Nickel and Nickelhydroxide, due to their neighboring position in the periodic table.

A.2. Iron electrode activated and discharged

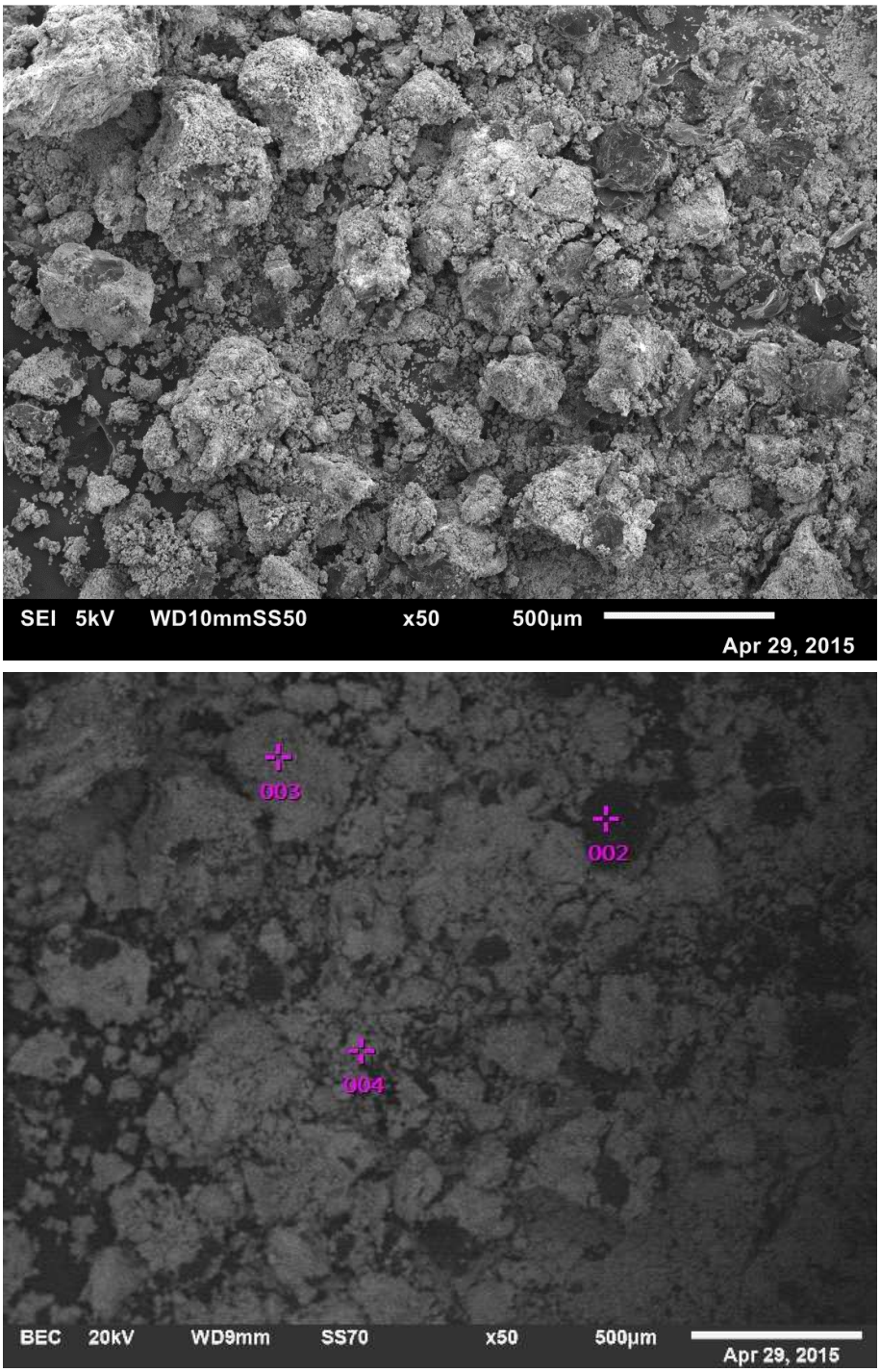

Figure A 4: SEI and BEC image of materials of the activated and discharge Fe-electrode. The marked point display the locations for point analysis.

Table A 6: Iron electrode, Overall EDS result:

Chemical formula	mass%	Atom%	Sigma	Net	K ratio	Line
C	40.01	62.65	0.02	1E+05	0.0027433	K
O	19.74	23.20	0.05	87586	0.0074428	K
Na	0.68	0.56	0.02	6359	0.0002878	K
K	1.91	0.92	0.02	47977	0.0022665	K
Fe	37.66	12.68	0.07	4E+05	0.0406154	K
Total	100.00	100.00				

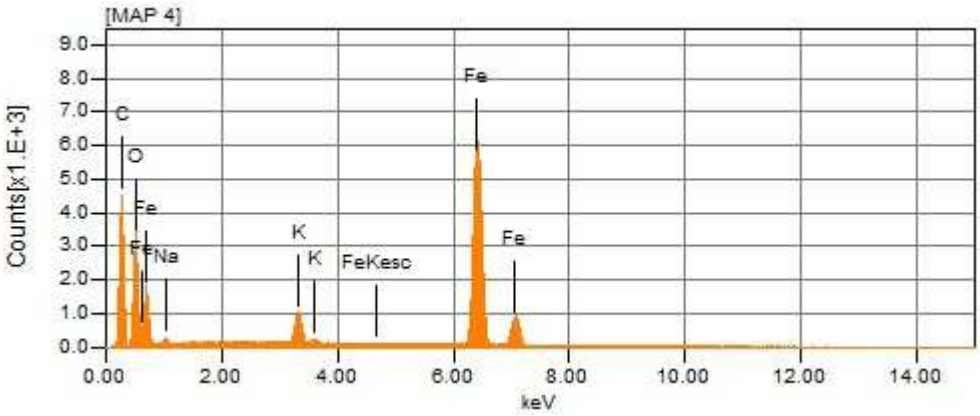

Table A 7: Iron electrode, EDS result for point 002:

Chemical formula	mass%	Atom%	Sigma	Net	K ratio	Line
C	100.00	100.00	0.04	3E+05	0.0568819	K
Total	100.00	100.00				

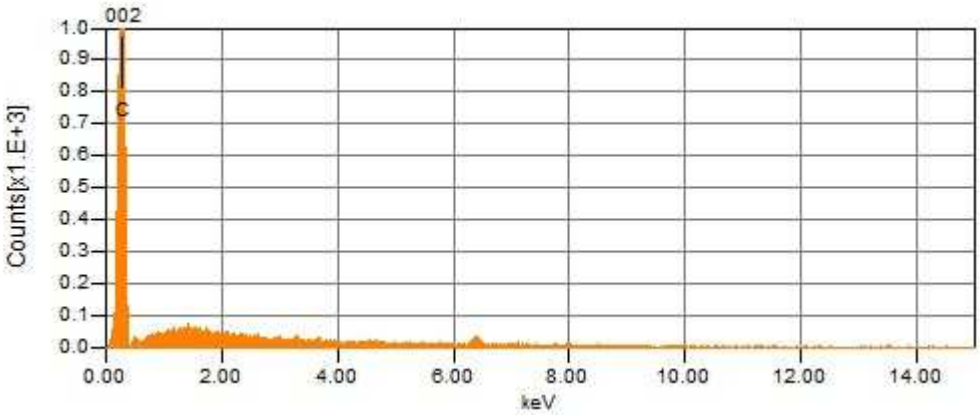

Table A 8: Iron electrode, EDS result for point 003:

Chemical formula	mass%	Atom%	Sigma	Net	K ratio	Line
C	16.64	34.61	0.04	9841	0.0020172	K
O	23.31	36.40	0.08	42082	0.0292948	K
Na	2.15	2.33	0.06	4738	0.0017567	K
K	3.90	2.49	0.04	26334	0.0101912	K
Fe	54.00	24.16	0.16	1E+05	0.1322122	K
Total	100.00	100.00				

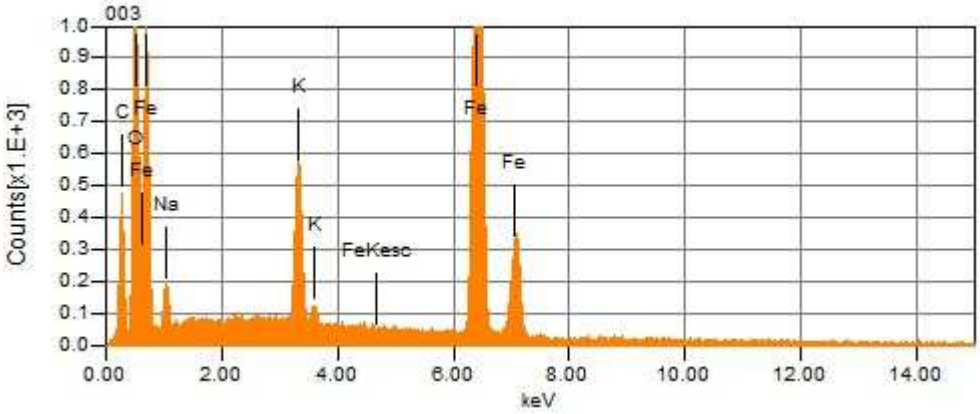

Table A 9: Iron electrode, EDS result for point 004:

Chemical formula	mass%	Atom%	Sigma	Net	K ratio	Line
C	42.78	66.65	0.05	29742	0.0060966	K
O	16.65	19.47	0.09	17408	0.0121187	K
K	2.03	0.97	0.03	12692	0.0049120	K
Fe	38.55	12.91	0.14	95376	0.0850324	K
Total	100.00	100.00				

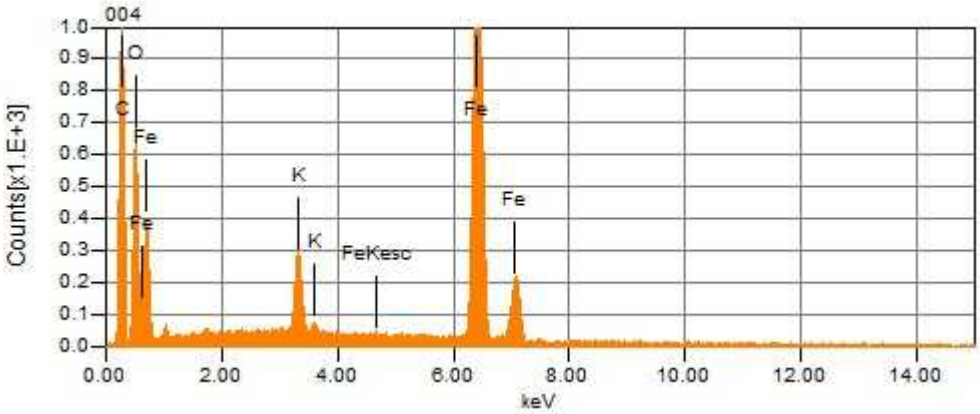

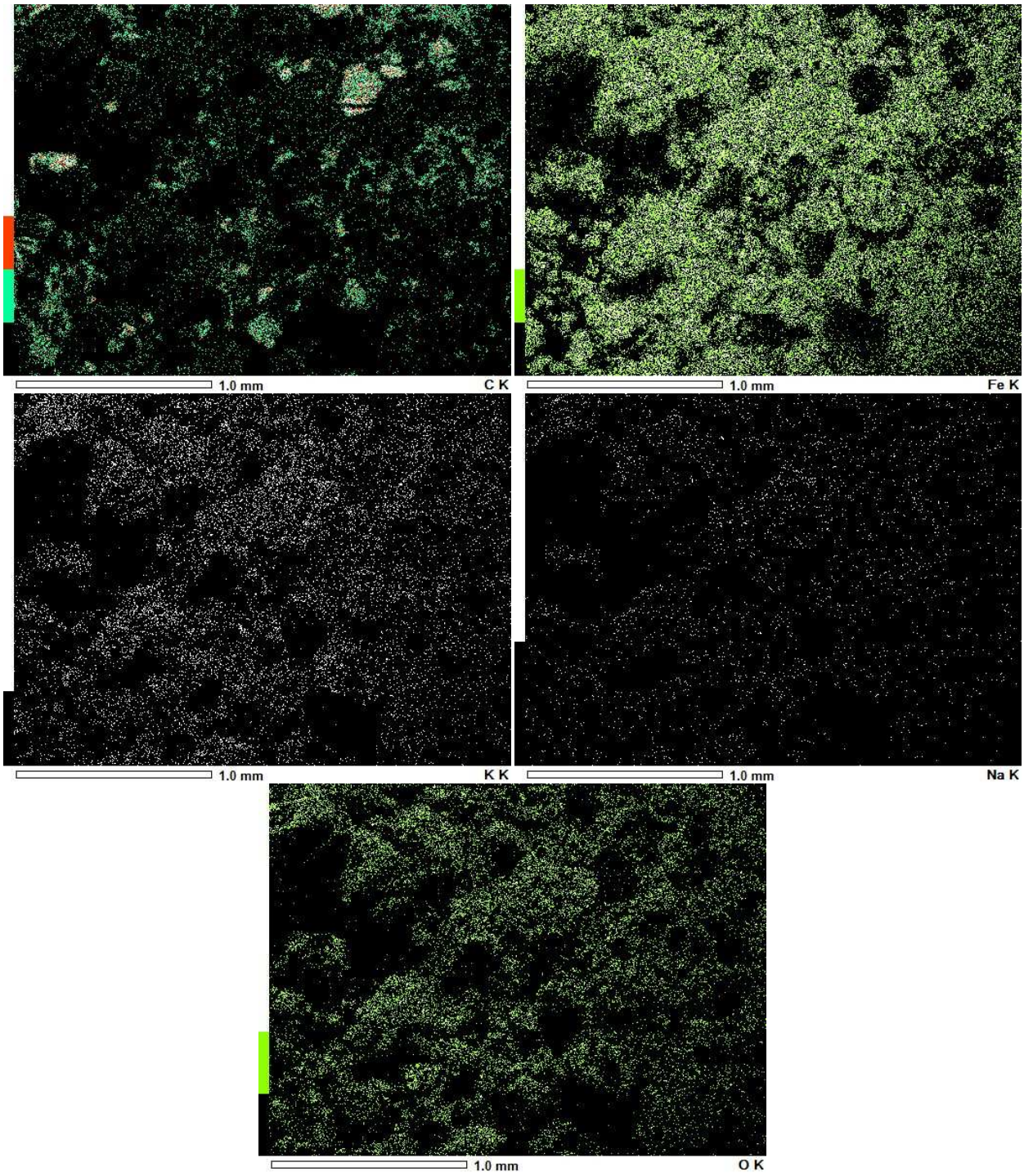

Figure A 5: Mapping image of chemical elements of the activated and discharge Fe-electrode; top left: Carbon, top right Iron; middle left Potassium; middle right: Sodium; bottom left: oxygen

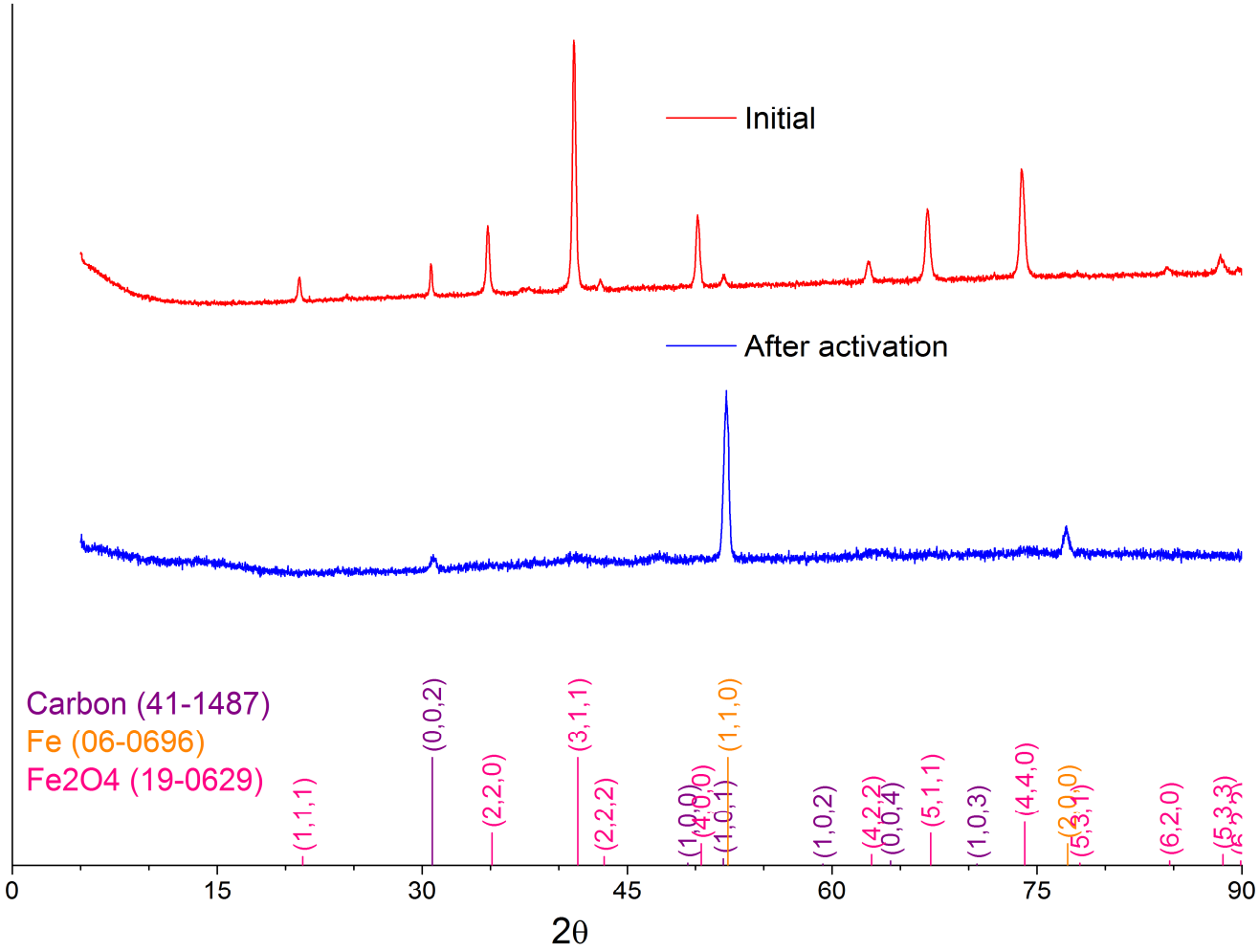

Figure A 6: XRD raw data of new and of activated and discharge Iron electrode, wavelength 1.78897.

A.3. Electrolyte-test; electrolyte droplets placed on carbon sheet and dried

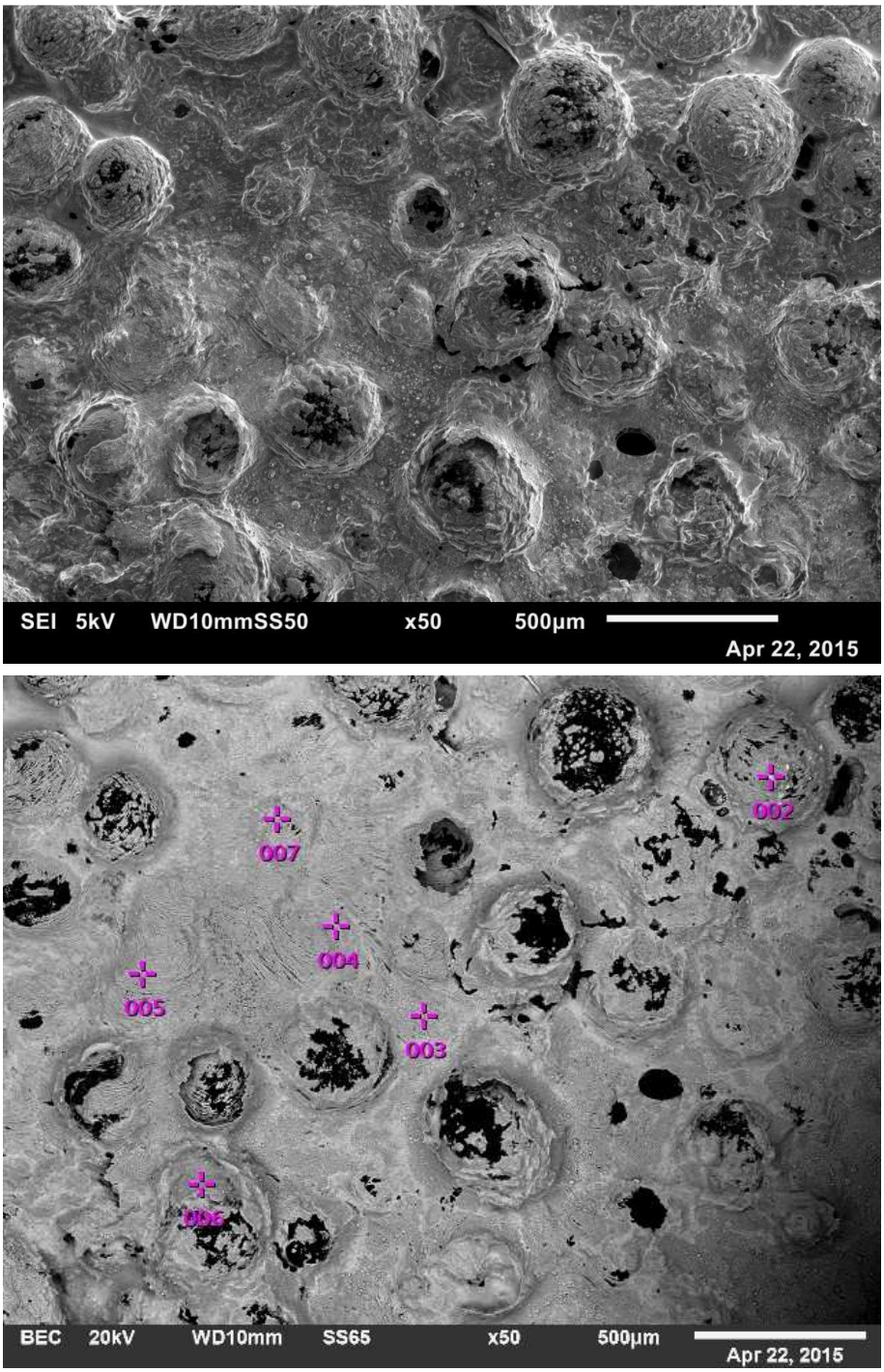

Figure A 7: SEI and BEC image of dried electrolyte. The marked point display the locations for point analysis.

Table A 10: Dried electrolyte, overall EDS result:

Chemical formula	mass%	Atom%	Sigma	Net	K ratio	Line
C	14.95	23.70	0.01	421799	0.0131929	K
O	42.80	50.94	0.02	1323228	0.1405566	K
Na	14.02	11.61	0.01	1770756	0.1001781	K
K	28.23	13.75	0.02	6333766	0.3740214	K
Total	100.00	100.00				

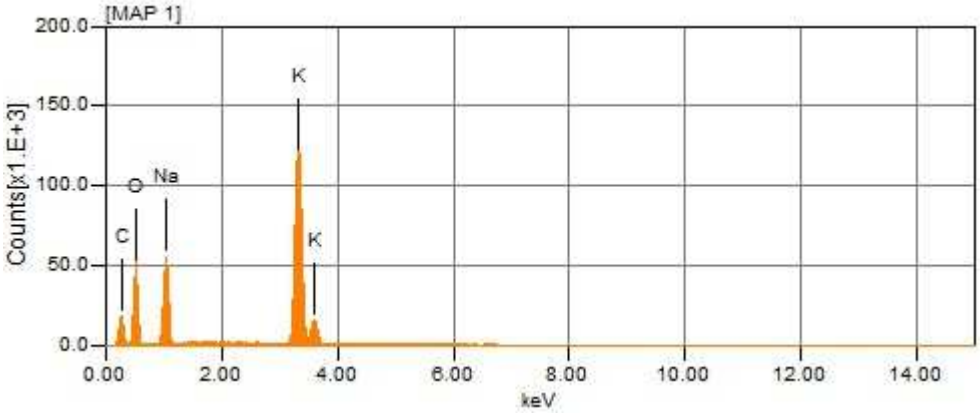

Table A 11: Dried electrolyte, EDS result for point 002:

Chemical formula	mass%	Atom%	Sigma	Net	K ratio	Line
C	3.68	8.03	0.01	4543	0.0037249	K
O	26.05	42.66	0.14	15931	0.0443609	K
Na	4.75	5.42	0.05	19638	0.0291243	K
K	65.51	43.90	0.13	512386	0.7931781	K
Total	100.00	100.00				

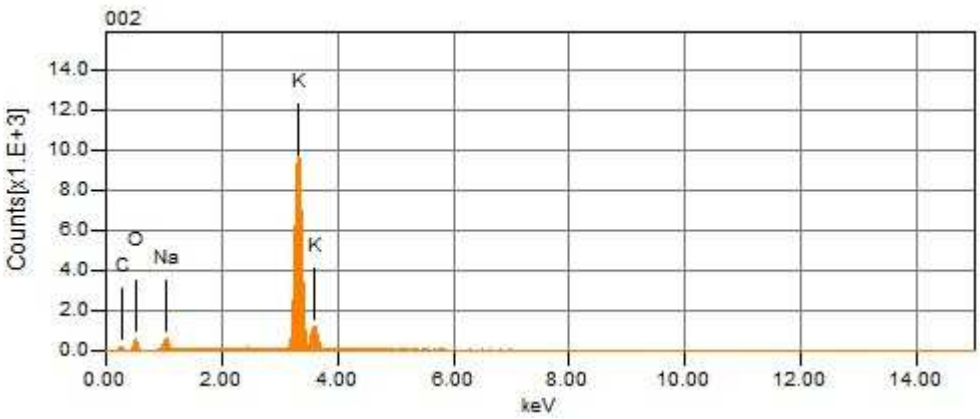

Table A 12: Dried electrolyte, EDS result for point 003:

Chemical formula	mass%	Atom%	Sigma	Net	K ratio	Line
C	8.34	15.15	0.02	10452	0.0085702	K
O	30.58	41.69	0.10	42473	0.1182686	K
Na	23.25	22.06	0.07	165153	0.2449278	K
K	37.82	21.10	0.08	432832	0.6700276	K
Total	100.00	100.00				

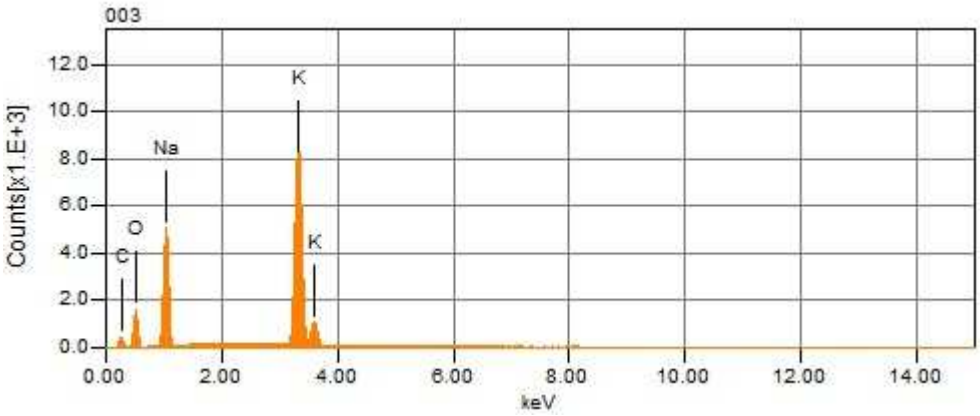

Table A 13: Dried electrolyte, EDS result for point 004:

Chemical formula	mass%	Atom%	Sigma	Net	K ratio	Line
C	10.12	18.04	0.02	15182	0.0124484	K
O	32.99	44.14	0.10	46652	0.1299054	K
Na	17.40	16.20	0.06	126604	0.1877590	K
K	39.48	21.61	0.08	489446	0.7576663	K
Total	100.00	100.00				

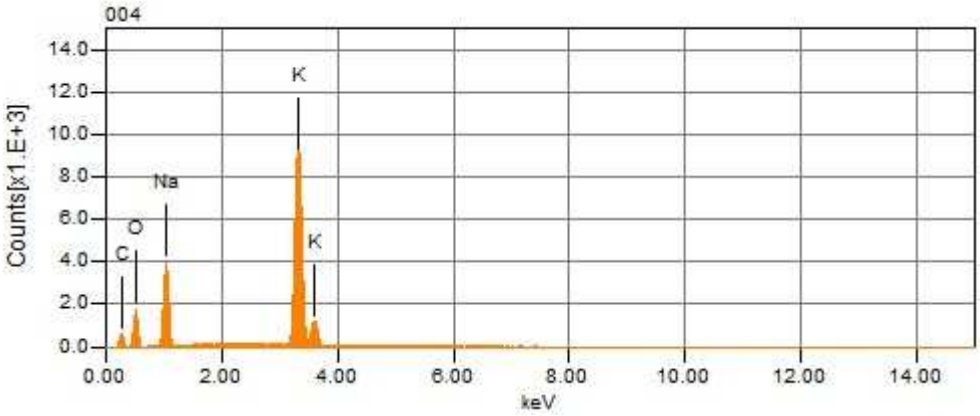

Table A 14: Dried electrolyte, EDS result for point 005:

Chemical formula	mass%	Atom%	Sigma	Net	K ratio	Line
C	9.00	16.25	0.02	15948	0.0130758	K
O	35.81	48.57	0.11	50922	0.1417960	K
Na	11.72	11.06	0.05	85988	0.1275235	K
K	43.47	24.12	0.08	577391	0.8938063	K
Total	100.00	100.00				

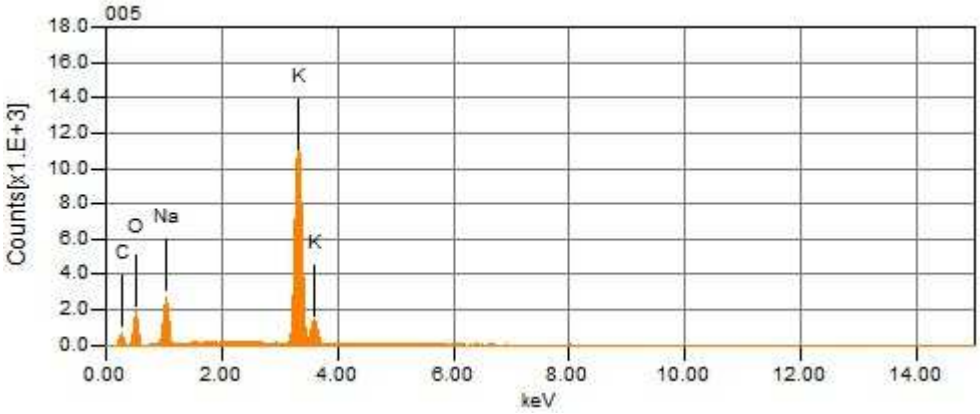

Table A 15: Dried electrolyte, EDS result for point 006:

Chemical formula	mass%	Atom%	Sigma	Net	K ratio	Line
C	14.23	22.06	0.02	37463	0.0307170	K
O	44.52	51.81	0.07	172644	0.4807374	K
Na	19.45	15.76	0.05	268503	0.3982008	K
K	21.80	10.38	0.04	510306	0.7899582	K
Total	100.00	100.00				

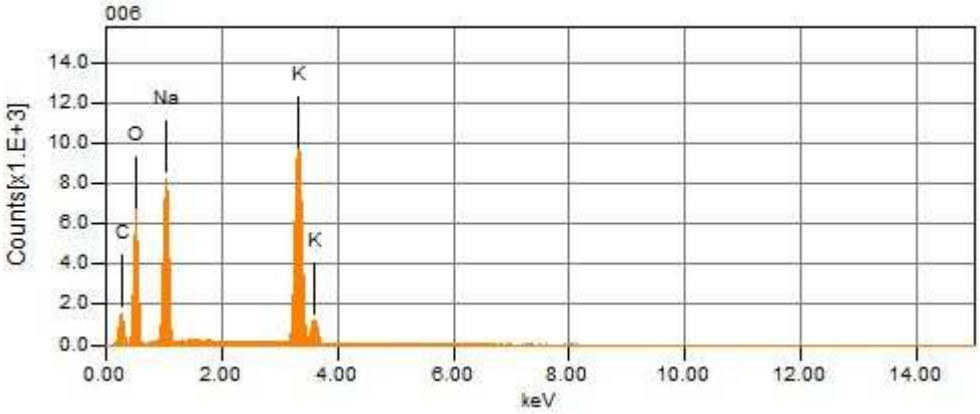

Table A 16: Dried electrolyte, EDS result for point 007:

Chemical formula	mass%	Atom%	Sigma	Net	K ratio	Line
C	14.94	24.29	0.02	31166	0.0255539	K
O	43.31	52.88	0.11	69245	0.1928169	K
Na	5.64	4.79	0.04	41004	0.0608100	K
K	36.12	18.04	0.07	504401	0.7808175	K
Total	100.00	100.00				

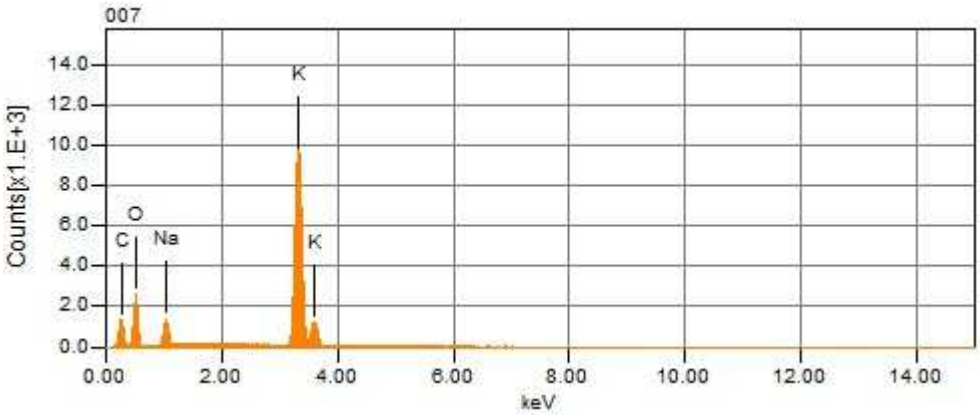

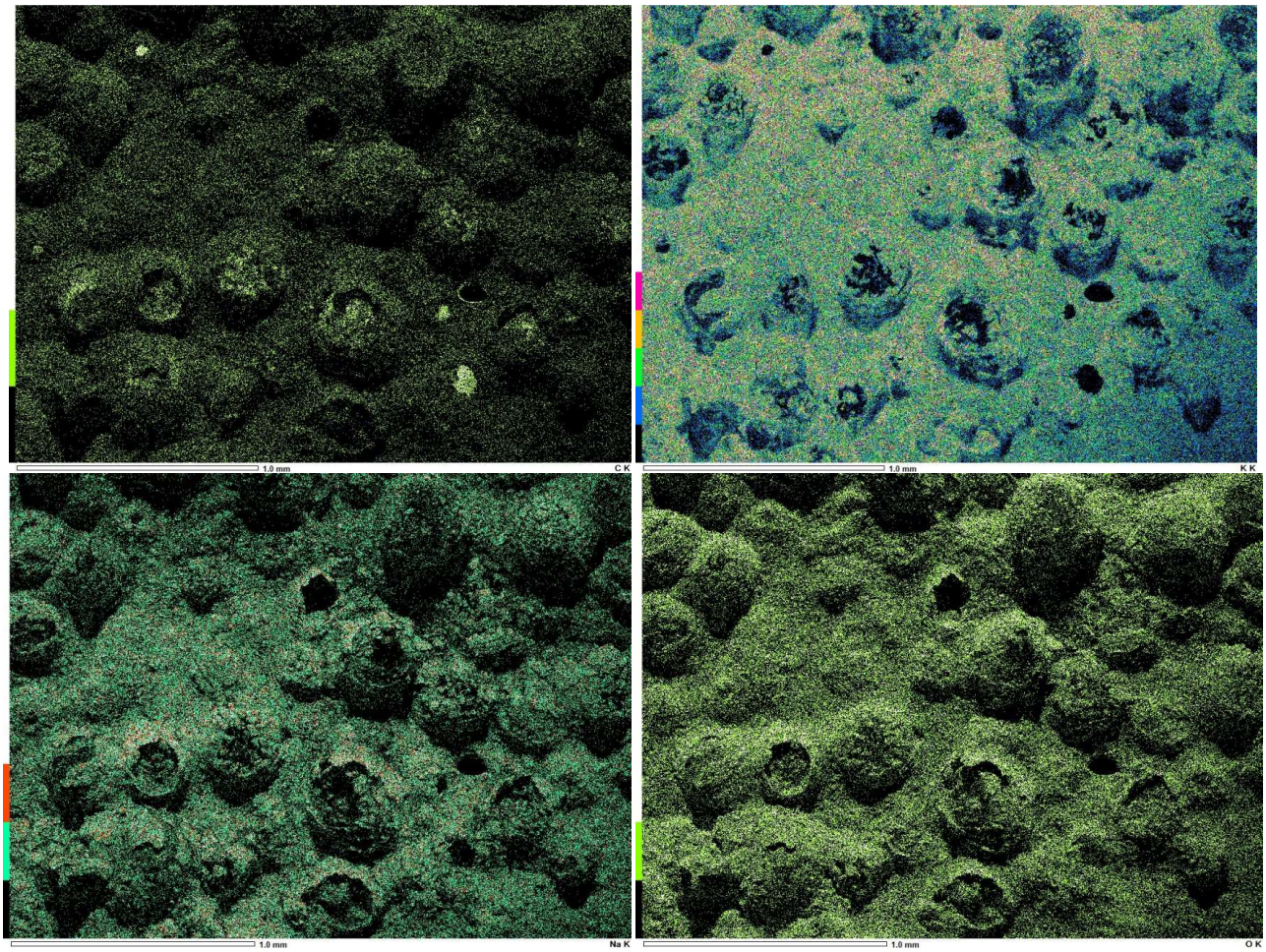

Figure A 8: Mapping image of chemical elements of dried electrolyte; top left: Carbon, top right Potassium; bottom left Sodium; bottom right: oxygen

Appendix B - Additional results varying electrolyte tests

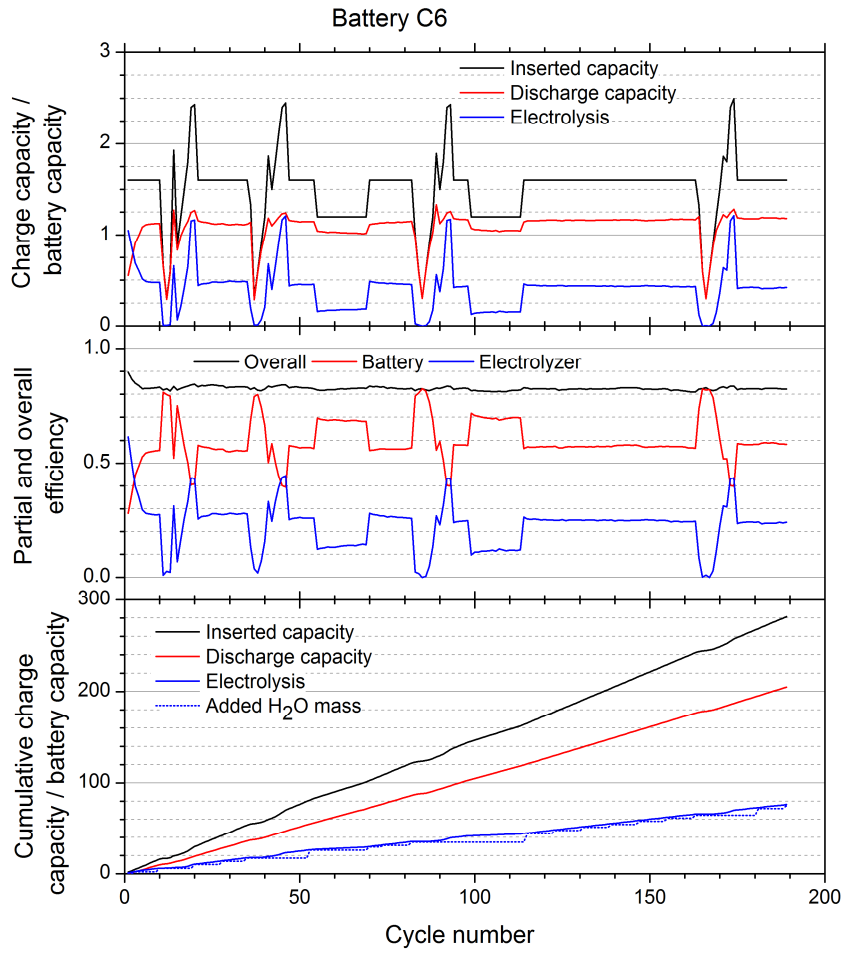

Figure B 1: History for batteries C6 with a low KOH concentration (11.5wt%): Top: inserted charge split up into discharge and electrolysis; Middle: partial efficiency for battery function and electrolysis as well as overall efficiency; Bottom: Cumulative inserted charge and breakdown in battery charge and electrolysis, and the cumulative H_2O mass to replenish the electrolyte expressed with respect to the battery capacity.

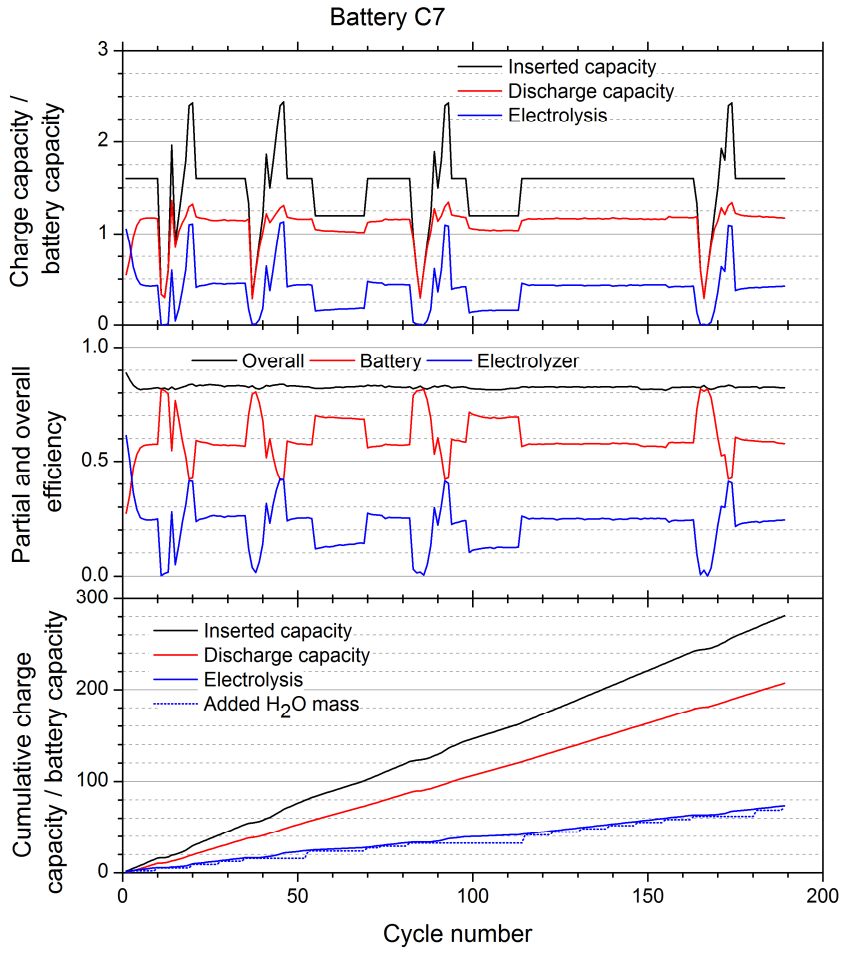

Figure B 2: History for batteries C7 with a standard KOH concentration (21wt%): Top: inserted charge split up into discharge and electrolysis; Middle: partial efficiency for battery function and electrolysis as well as overall efficiency; Bottom: Cumulative inserted charge and breakdown in battery charge and electrolysis, and the cumulative H_2O mass to replenish the electrolyte expressed with respect to the battery capacity.

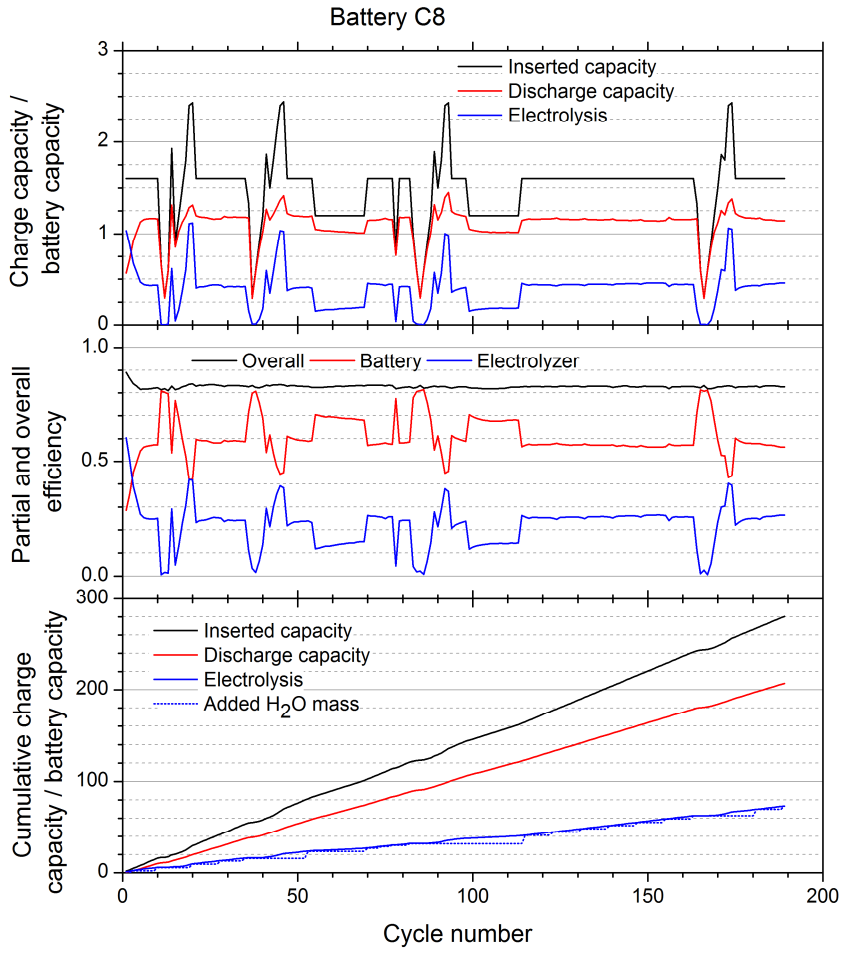

Figure B 3: History for batteries C8 with a high KOH concentration (30wt%): Top: inserted charge split up into discharge and electrolysis; Middle: partial efficiency for battery function and electrolysis as well as overall efficiency; Bottom: Cumulative inserted charge and breakdown in battery charge and electrolysis, and the cumulative H_2O mass to replenish the electrolyte expressed with respect to the battery capacity.

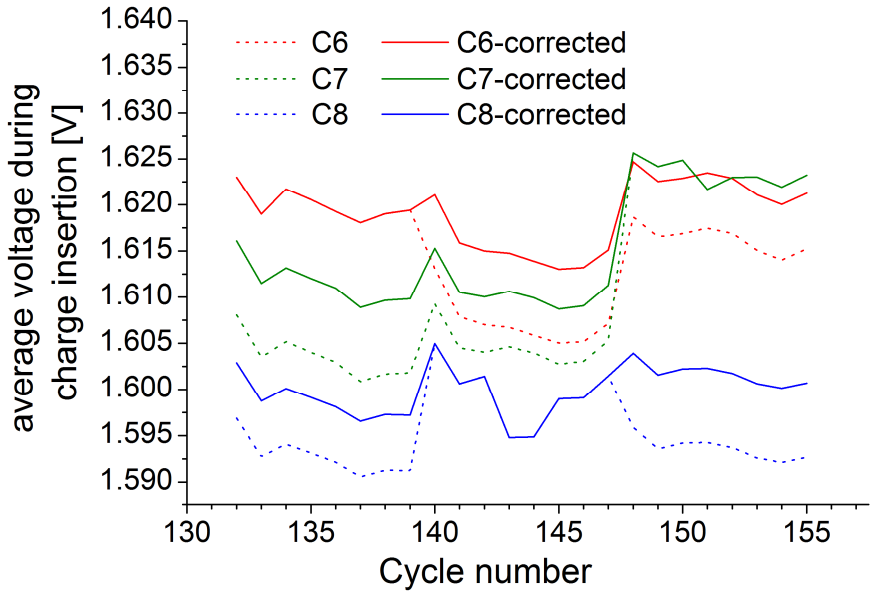

Figure B 4: Average voltage during charging for test-channel variation with and without correction.

Table B 1: average voltage [V] for test-channel variation, raw-data from Maccor and corrected values

Cycle nr	C6	C7	C8	C6-corr.	C7-corr.	C8-corr
132	1.623	1.608	1.597	1.623	1.616	1.603
133	1.619	1.603	1.593	1.619	1.611	1.599
134	1.622	1.605	1.594	1.622	1.613	1.600
135	1.621	1.604	1.593	1.621	1.612	1.599
136	1.619	1.603	1.592	1.619	1.611	1.598
137	1.618	1.601	1.591	1.618	1.609	1.597
138	1.619	1.602	1.591	1.619	1.610	1.597
139	1.619	1.602	1.591	1.619	1.610	1.597
140	1.613	1.609	1.605	1.621	1.615	1.605
141	1.608	1.605	1.601	1.616	1.611	1.601
142	1.607	1.604	1.601	1.615	1.610	1.601
143	1.607	1.605	1.595	1.615	1.611	1.595
144	1.606	1.604	1.595	1.614	1.610	1.595
145	1.605	1.603	1.599	1.613	1.609	1.599
146	1.605	1.603	1.599	1.613	1.609	1.599
147	1.607	1.605	1.601	1.615	1.611	1.601
148	1.619	1.626	1.596	1.625	1.626	1.604
149	1.617	1.624	1.594	1.623	1.624	1.602
150	1.617	1.625	1.594	1.623	1.625	1.602
151	1.617	1.622	1.594	1.623	1.622	1.602
152	1.617	1.623	1.594	1.623	1.623	1.602
153	1.615	1.623	1.593	1.621	1.623	1.601
154	1.614	1.622	1.592	1.620	1.622	1.600
155	1.615	1.623	1.593	1.621	1.623	1.601
Color-code for test-channel	12	10	11	Corr: 0.006V	Corr: 0.0V	Corr: 0.008V

Appendix C - Calculation of heat transfer coefficient for the insulated setup

The heat transfer $\dot{Q}$ [W] for the setup is calculated according to Eg. (3.32) $\dot{Q} = kS\Delta T$ and Table 3.2 for the shape factor S form [54]. A shape factor exists for the configurations 1, 10 and 11 belonging to a plane wall, the edge of adjoined walls and the corner of three adjoining walls respectively. For simplification the bottom and the top of the box is neglected. The isolation of the bottom side is thicker and furthermore the box stands on the table, therefore this contribution will be small. A box for storing spare polystyrene chips (several centimeter high) was located on the top of the setup during testing, this contribution will also be small.

The shape factor of plane walls is the surface area divided by the wall's thickness. The larger box has outer dimensions of 390 mm x 290 mm x 370 mm (L x W x H) with a thickness of 50 mm. The area of plain surfaces is (2*(0.29*0.27+0.19*0.27)=) 0.2592 m² and the shape factor S in 0.2592 / 0.05 = 5.184. The shape factor for edge of adjoining walls equals 0.54 * W, the inner edge length. The total inner edge lengths is (4*0.27+2*(0.19+0.29)=) 2.04m, the shape factor is 0.54 * 2.04 = 1.1016. The shape factor for corners of three adjoining walls equals 0.15 * the wall thickness, the shape factor corners is therefore 4 * 0.05 * 0.15 = 0.03. The total shape factor is 5.184 + 1.1016 + 0.03 = 6.3156 m. Polystyrene has a heat transfer coefficient k of 0.028 W/(m.K) (see table 1.1 [54]).

The heat transfer coefficient for free convection in air is in the order of 10 W/(m².K). The sum of inner and outer surface of the box results in 2*(0.37*(0.29+0.39)+0.27*(0.19+0.29)) = 0.7624 m². The reciprocal addition of conductive and convective heat transfer leads to a:

$$\frac{1}{h_{tot}} = \frac{1}{kS} + \frac{1}{A_{suf} * h_{conv}} = \frac{1}{0.028 * 6.3156} + \frac{1}{0.7624 * 10} = \frac{1}{0.17}$$

The following relation can be used to estimate heat losses: $\dot{Q} = 0.17\ \Delta T$.

Appendix D - Impedance spectroscopy

The following four figures depict Nyquist plots of performed constant current EIS tests. Four different operation modes are investigated: 1) Charging of the electrodes; 2) Electrolysis at the activated electrodes, performed with various currents; 3) Discharging of the electrodes and 4) Discharged electrode at rest.

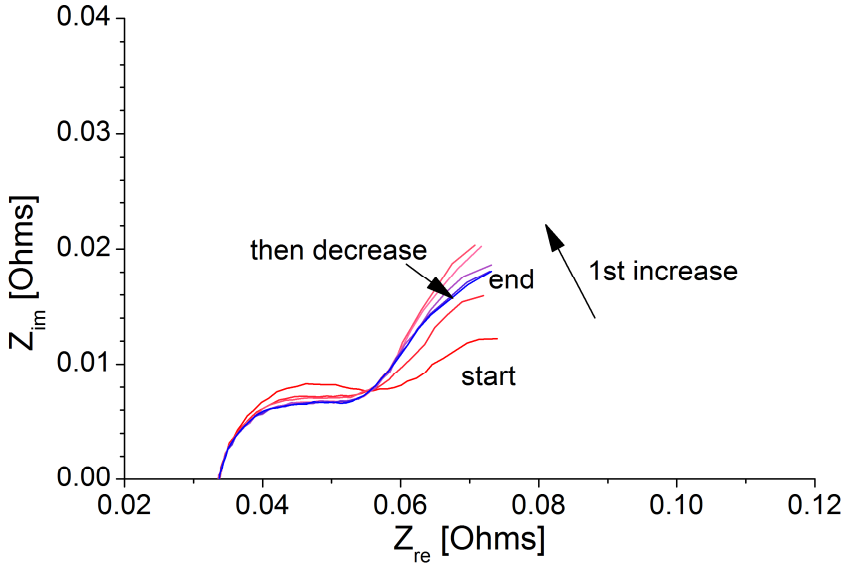

Figure D 1: Nyquist plots during charging of the electrodes: the test starts at the discharged electrode (red line) which has the largest first semicircle and ends at the charged electrode (blue line). The size of the first semicircle decreases with the charging process what indicates changes in the bulk. The second semicircle first increases and then decreases. All tests are performed at a charge rate of 1A

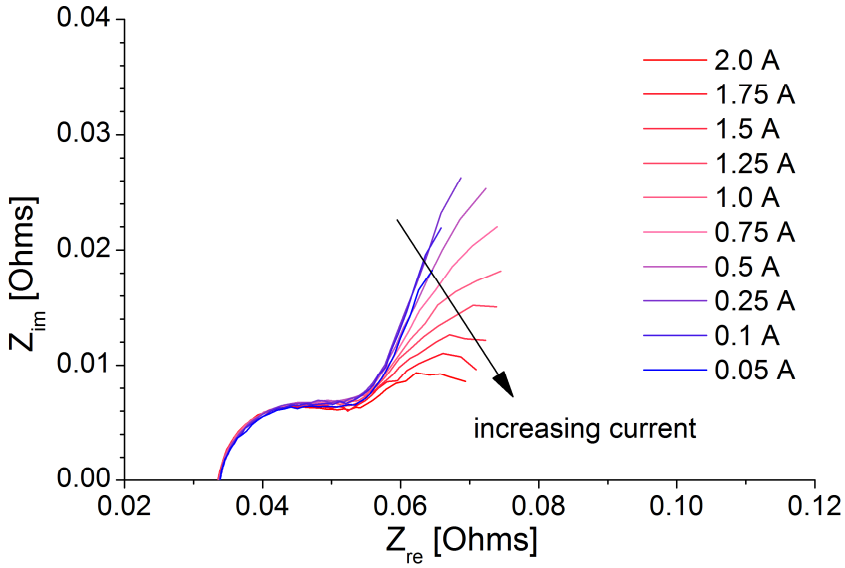

Figure D 2: Nyquist plots during electrolysis at the activated electrodes: The blue line represents the lowest current, 0.05A and the red line the highest current 2A. The first semicircle remains constant throughout the test meaning that the bulk of the electrodes does not change. The second semicircle decreases with increasing current meaning that the charge transfer between the electrodes and the electrolyte is faster what could indicate increased surface activity.

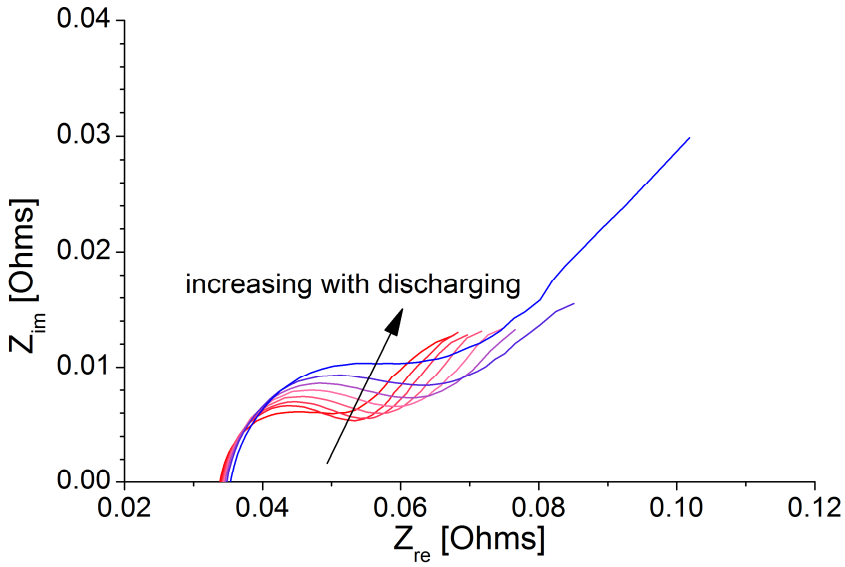

Figure D 3: Nyquist plots during discharging the electrodes. The test starts at the charged electrodes (red line) and ends at the discharge electrodes (blue line). The first semicircle associated with bulk of the electrode and increases steadily implying that the capcitance of the bulk increases. The second semicircle seems to shift according to changes in the first semicircle but not to vary itself, besides the last measurement (blue line) at the discharged electrode were the semicircle is increased. All tests are performed at a discharge rate of 0.5A.

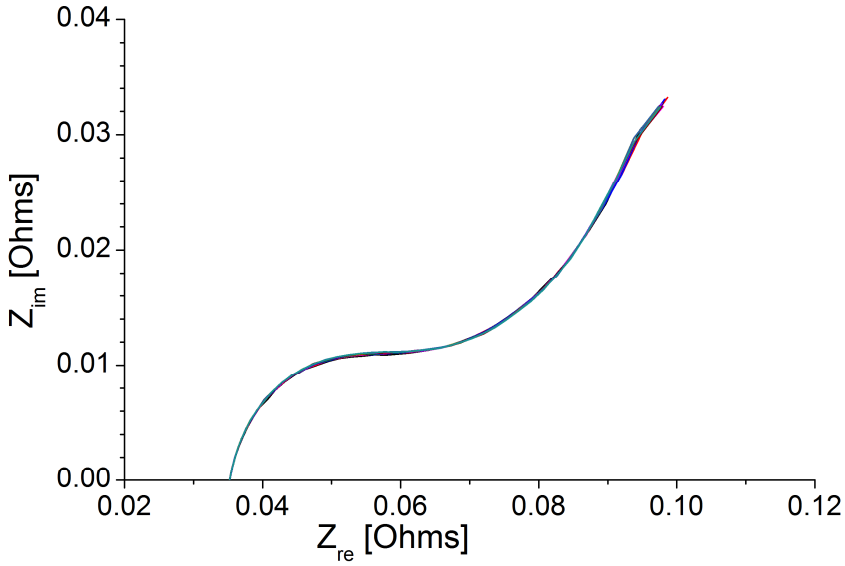

Figure D 4: Nyquist plots at the discharged electrode during a rest period of 10 hours. All tests are performed without applying any charge rate. The results are similar to the results obtained for the discharged electrode. The open circuit potential increases during this tests slightly form 1.29V to 1.32V.